Field Line Resonance in Two and a Half Dimensions

DRAFT VERSION CREATED ON APRIL 10, 2016

Acknowledgements

Acknowledgement placeholder.

Dedication

Dedication placeholder.

Abstract

Abstract placeholder.

Contents

List of Tables

List of Figures

Chapter 1

Introduction

1859 was a pivotal year in human history. The United States moved steadily toward the American Civil War, which would abolish slavery and consolidate the power of the federal government. A slew of conflicts in Southern Europe, such as the Austro-Sardinian War, set the stage for the unification of Italy. The Taiping Civil War — one of the bloodiest conflicts of all time — is considered by many to mark the beginning of modern Chinese history. Origin of Species was published. The first transatlantic telegraph cable was laid.

Meanwhile, ambivalent to humanity, the Sun belched an intense burst of charged particles and magnetic energy directly at Earth. The resulting geomagnetic storm[1] caused telegraph systems to fail across the Western hemisphere, electrocuting operators and starting fires[36, 98]. Displays of the northern lights were visible as far south as Cuba.

The Solar Storm of 1859 was perhaps the most powerful in recorded history, but by no means was it a one-time event. The Sun discharges hundreds of coronal mass ejections (CMEs) per year, of all sizes, in all directions. In fact, a comparably large CME narrowly missed Earth in 2012[74]. Had it not, it's estimated it would have caused widespread, long-term electrical outages, with a damage toll on the order of 10^{12} dollars[68].

[1] The Solar Storm of 1859 is also called the Carrington Event, after English astronomer Richard Carrington. He drew a connection between the storm's geomagnetic activity and the sunspots he had observed the day before.

The Sun's extreme — and temperamental — effect on Earth's magnetic environment makes a compelling case for the ongoing study of space weather. Such research has evolved over the past century from sunspot counts and compass readings to multi-satellite missions and supercomputer simulations. Modern methods have dramatically increased humanity's understanding of the relationship between the Sun and the Earth; however, significant uncertainty continues to surround geomagnetic storms, substorms, and the various energy transport mechanisms that make them up.

The present work focuses in particular on the phenomenon of field line resonance: Alfvén waves bouncing between the northern and southern hemispheres. Such waves play an important part in the energization of magnetospheric particles, the transport of energy from high to low altitude, and the driving of currents at the top of the atmosphere.

TODO: More is needed before we can jump into a description of the present work. Introduce what we're working on a bit ore specifically. Talk about how space is a laboratory that teaches us about plasma in a way that's relevant to both astrophysics and fusion reactors, which are hard to measure. Fishbone instability.

1.1 Structure of the Present Work

Chapter 2 surveys the near-Earth environment. Prominent features of the magnetosphere are defined. The response of the magnetosphere to transient solar wind events is summarized.

Chapter 3 introduces the field line resonance phenomenon, in terms of both the underlying physics and notable work on the topic. Jargon is introduced to clarify important elements of wave structure. Several open questions about field line resonances (FLRs) are offered as motivations for the present work.

Chapter 4 lays the groundwork for a numerical model by exploring the fundamental equations of waves in a cold, resistive plasma — such as Earth's magnetosphere. Characteristic scales are gleaned from the resulting dispersion relations.

Chapter 5 presents Tuna, a new two and a half dimensional simulation designed specifically for the realistic modeling of FLRs. Tuna's non-orthogonal geometry, height-resolved ionosphere, novel driving mechanism, and coupling to the atmosphere are explained.

Chapter 6 considers the addition of electron inertial effects to Tuna, touches on what can be learned from them, and shows that they incur an unreasonable computational cost. (Electron inertia is neglected in the results presented in other chapters.) TODO: Previous work has looked at inertial effects for localized models. The exciting part is that we're looking at a global model.

Chapter 7 describes the core numerical results of the work, unifying several of the questions posed in Chapter 3. Significant depth is added to past work on finite poloidal lifetimes[66, 80]. Interplay between poloidal-toroidal coupling, shear-compressional coupling, and Joule dissipation is considered from several angles.

Chapter 8 puts the numerical results in physical context through the analysis of data from the Van Allen Probes mission. FLR occurrence rates are considered in terms of location, mode structure, and polarization – parameters which have been only partially addressed by other recent FLR surveys[18, 72].

Chapter 9 briefly summarizes the results shown in the above chapters — the code development, analysis of numerical results, and satellite observation — and suggests further directions.

Chapter 2

The Near-Earth Environment

From Earth's surface to a height of a hundred kilometers or so, the atmosphere is a well-behaved fluid: a collisional ensemble of neutral atoms. Higher up, its behavior changes dramatically. As altitude increases, solar ultraviolet radiation becomes more intense, which ionizes atmospheric atoms and molecules. Density also decreases, slowing collisional recombination. Whereas the neutral atmosphere is held against Earth's surface by gravity, the motion of charged particles is dominated by Earth's geomagnetic field, as well as the electromagnetic disturbances created as that field is hammered by the solar wind.

Before discussing specific interactions, it's appropriate to introduce the so-called "frozen-in condition." In a collisionless plasma, magnetic field lines are equiputential contours. Charged particles move freely along the contours, but cannot move across them. Compression of the magnetic field is synonymous with compression of the ambient plasma, and any magnetic field lines that thread a moving plasma are dragged along with it. This assumption is valid throughout most of the magnetosphere — that is, the region of space primarily governed by Earth's magnetic field — and provides an invaluable tool for understanding the large-scale motions of plasmas and fields.

2.1 The Outer Magnetosphere

Plasma behavior within Earth's magnetosphere is ultimately driven by the solar wind: a hot ($\sim$100 eV), fast-moving ($\sim$100 km/s) plasma threaded by the interplanetary magnetic field ($\sim$10 nT)[1]. The density of the solar wind is on the order of $10\,/\mathrm{cm}^3$; in a laboratory setting, this would constitute an ultra-high vacuum (atmospheric density at sea level is $\sim 10^{19}\,/\mathrm{cm}^3$), but compared to much of the magnetopause it's quite dense.

Figure 2.1: TODO: The outer magnetosphere...

The magnetosphere's outer boundary represents a balance between the solar wind dynamic pressure and the magnetic pressure of Earth's dipole field. On the dayside, the dipole is compressed, pushing this boundary to within about $10\,\mathrm{R_E}$ of Earth[2]. The nightside magnetosphere is stretched into a long tail which may exceed $50\,\mathrm{R_E}$ in width and $100\,\mathrm{R_E}$ in length.

[1] Listed values correspond to the solar wind at Earth's orbit.
[2] Distances in the magnetosphere are typically measured in units of Earth radii: $1\,\mathrm{R_E} \equiv 6378\,\mathrm{km}$.

When the interplanetary magnetic field opposes the geomagnetic field at the nose of the magnetosphere, magnetic reconnection occurs. Closed magnetospheric field lines "break," opening up to the interplanetary magnetic field[3]. They then move tailward across the poles, dragging their frozen-in plasma with them. Reconnection in the tail allows magnetic field lines to convect back to the day side, across the flanks. This process is called the Dungey cycle[23].

Viewed from the north, the Dungey cycle involves a clockwise flow of flux and plasma on the dusk side and a counterclockwise flow on the dusk side. The motion is accompanied by a convection electric field, per Ohm's law in an ideal plasma:

$$\underline{E} + \underline{U} \times \underline{B} = 0 \tag{2.1}$$

TODO: Jets from magnetic reconnection... release of magnetic tension!

Consistent with Ampère's law, the interplanetary magnetic field is separated from the magnetosphere by a current sheet: the magnetopause. On the dayside, the magnetopause current flows duskward; on the nightside, it flows dawnward around the magnetotail.

Earth's dipole is significantly deformed in the magnetotail; field lines in the northern lobe of the tail points more or less Earthward, and vice versa. Plasma within the lobes is cool ($\sim$100 eV) and rarefied ($\sim 10^{-2}\,/\mathrm{cm}^3$). The two lobes are divided by the plasma sheet, which is comparably hot ($\sim 10^3$ eV) and dense ($\sim 1\,/\mathrm{cm}^3$). The plasma sheet carries a duskward current which connects to the magnetopause current.

[3] Closed field lines are more or less dipolar; one end connects to the north pole of Earth's magnetic core, and the other end to the south pole. Open field lines are tethered to Earth at one end. In principle, the other end eventually doubles back to Earth, but for practical purposes it is lost to the solar wind. The distinction is important because charged particle motion is guided by magnetic field lines, as discussed in Chapter 3.

2.2 The Inner Magnetosphere

Within about $L \sim 8$ (where L is the McIlwain parameter[4]), the dipole magnetic field is not appreciably deformed by the solar wind. As a result, the structures in the inner magnetosphere follow closely from the motion of charged particles in an ideal dipole field.

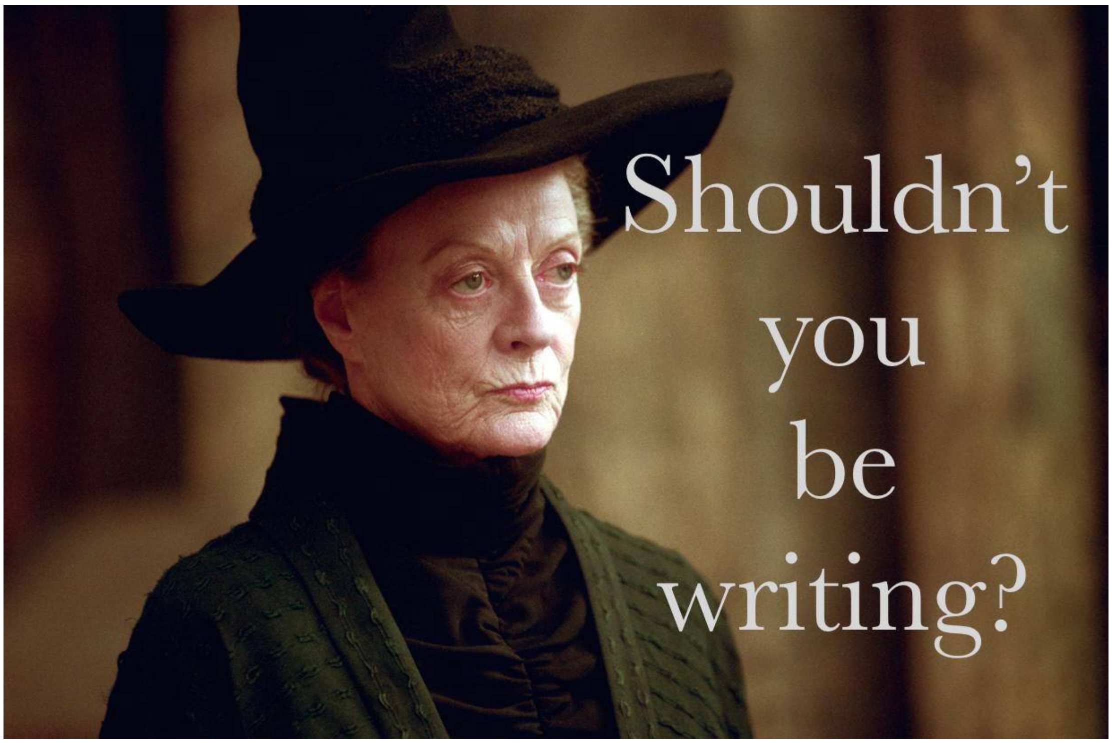

Figure 2.2: TODO: The inner magnetosphere...

The plasmasphere — a cold ($\sim$1 eV), dense ($10^2\,/\mathrm{cm}^3$ to $10^4\,/\mathrm{cm}^3$) torus of corotating plasma — is formed by the outward drift of atmospheric ions along magnetic closed field lines. Its outer boundary is thought to represent a balance between the corotation electric field (per the rotation of Earth's magnetic dipole) and the convection electric

[4]The McIlwain parameter L is used to index field lines in Earth's dipole geometry: $L \equiv \frac{r}{\sin^2\theta}$ for colatitude θ and radius r in Earth radii. For example, the $L = 5$ field line passes through the equatorial plane at a geocentric radius of $5\,\mathrm{R_E}$, then meets the Earth at a colatitude of $\arcsin\sqrt{\frac{1}{5}} \sim 27^\circ$ (equally, a latitude of $\arccos\sqrt{\frac{1}{5}} \sim 63^\circ$).

field (associated with the convection of magnetic flux during the Dungey cycle). Particle density drops sharply at the edge of the plasmasphere; the boundary is called the plasmapause. The plasmapause typically falls around $L = 4$, though during prolonged quiet times it can extend to $L = 6$ or larger.

Energetic particles trapped within the inner magnetosphere are divided into two populations.

The Van Allen radiation belts are made up of particles with energy above $10^5\,\mathrm{eV}$ or so. The inner belt ($L \lesssim 2$) is primarily composed of protons, the decay remnants of neutrons freed from the atmosphere by cosmic rays. The outer belt ($L \gtrsim 4$) is primarily composed of high-energy electrons. The density of radiation belt particles is significantly affected by geomagnetic storms and substorms; a typical value is $10\,/\mathrm{cm}^3$.

Particles with energies of $10^3\,\mathrm{eV}$ to $10^5\,\mathrm{eV}$ make up the ring current, which extends from $L \sim 3$ to $L \sim 5$. Gradient-curvature drift carries ions and electrons in opposite directions; the net result is a westward current. During quiet times, the ring current causes magnetic a southward magnetic field on the order of $1\,\mathrm{nT}$ at Earth's equator, while during geomagnetically active times (discussed in Section 2.4) the effect may $100\,\mathrm{nT}$ or more[5].

2.3 The Ionosphere

Earth's neutral atmosphere is an excellent insulator. Collisions are so frequent that charged particles quickly thermalize and recombine. The breakdown of air molecules into a conductive plasma (as happens during a lightning strike, for example) requires electric fields on the order of $10^9\,\mathrm{mV/m}$.

Cold particles in the magnetosphere are likewise not conducive to currents. In the absence of collisions, electrons and ions drift alongside one another in response to an electric field, creating no net current perpendicular to the magnetic field[6].

[5]For comparison, Earth's dipole field points north at the equator with a magnitude over $10^4\,\mathrm{nT}$.

[6]The so-called E-cross-B drift is associated with a velocity of $\underline{U} = \frac{1}{B^2}\underline{E} \times \underline{B}$, independent of a charged particle's mass or sign.

The ionosphere is a sweet spot between the two regimes. Collisions are frequent enough to disrupt the drift of ions, but not frequent enough to immobilize the electrons. The result is nonzero Pedersen and Hall conductivity, corresponding to current along the electric field and in the $\underline{B} \times \underline{E}$ direction respectively. It is these currents — particularly the Hall current — which give rise to magnetic fields at the ground. Collisions in the ionosphere also give rise to a finite parallel conductivity, allowing for the formation of potential structures along the magnetic field line.

The convection electric field (associated with the Dungey cycle, Section 2.1) drives Pedersen currents in the ionosphere. Pedersen currents flow dawnward on the flanks and duskward across the poles. The currents remain divergence-free by connecting to field-aligned currents at the edges of the polar cap. The field-aligned currents, in turn, connect to the magnetopause current, the cross-tail current, and the (partial) ring current.

When electron density is low, thermal velocities may be unable to carry enough current to satisfy $\nabla \cdot \underline{J} = 0$. This leads to the formation of potential structures along geomagnetic field lines in the ionosphere. Such structures accelerate particles along magnetic field lines, leading to the precipitation of energetic particles into the atmosphere. As the particles thermalize, they excite atmospheric atoms. The resulting spontaneous emission is often in the visible spectrum, giving rise to the aurora.

2.4 Geomagnetic Storms and Substorms

The quiet geomagnetic behavior described above is periodically disturbed by transient solar phenomena such as corotating interaction regions (CIRs) and coronal mass ejections (CMEs). CMEs, as noted in Chapter 1, are bursts of unusually dense solar wind which are ejected from regions of high magnetic activity on the Sun; they are most common at the height of the eleven-year solar cycle. CIRs, on the other hand, occur when a relatively fast region of the solar wind catches up to an earlier and slower-moving pocket of solar wind, resulting in a pair of shockwaves.

During a storm, increased solar wind intensity results in enhanced magnetic reconnection on the dayside. As the newly-opened field lines are swept tailward, the convection electric field is strengthened. The plasmasphere — the outer boundary of which is set by a balance between the convection electric field and the (more or less constant) corotation electric field — sheds its outer layers. A large number of energetic particles are also injected into the ring current[70].

The strength of the storm is gauged by the size of the magnetic perturbation created by the ring current[7]. A small storm has a magnitude of 50 nT to 100 nT. Large storms may reach 250 nT to 500 nT. The Carrington Event, mentioned in Chapter 1, is thought to have exceeded 1700 nT[98].

The main phase of a storm typically lasts for several hours. Storm recovery — the gradual return of the storm index to zero, and the refilling of the plasmasphere — typically lasts several days. Geomagnetic storms occur tens of times per year at the height of the solar cycle, and just a few times per year otherwise.

Whereas storms are prompted by large solar wind events on the dayside, geomagnetic substorms are primarily a nightside occurrence. As flux accumulates in the tail, magnetic tension builds in the stretched field lines. A substorm is an impulsive release of that tension.

TODO: Phases of a substorm. Definition of a substorm comes from [1]. Revised by [71].

At substorm onset, a burst of reconnection occurs in the tail. A jet of plasma is launched Earthward from the reconnection site (and another is launched tailward, and lost to the solar wind). The Earthward plasma injection injects particles into the ring current. The outer radiation belt is depleted, then repopulated. Energetic particles precipitate into the atmosphere, giving rise to a distinctive sequence of auroral signatures over the course of about an hour.

[7]The most commonly used storm index is DST, which is computed hourly using measurements from several ground magnetometers near the equator. The Sym-H index, used in Section 5.3, is computed once per minute.

Concurrent with substorm onset, impulsive Alfvén waves are observed with periods of a minute or two. The precise ordering of events — whether reconnection causes the waves, or vice versa, or if they share a common cause — remains controversial.

Each substorm lasts several hours, including the time it takes for the ring current to return to pre-substorm levels. Several substorms may occur per day during quiet times. During a storm, substorms become far more frequent; by the time one has ended, another may have already begun.

Chapter 3

Field Line Resonance

The motion of a charged particle in a dipole field can be described in terms of three fundamental motions. The first is cyclotron motion. Given a uniform magnetic field line, a particle follows a helical path. It moves in a circular path in a plane normal to the magnetic field line, and keeps a constant velocity along the direction of the field.

The second fundamental motion is bounce motion. As it moves along the magnetic field line like a bead on a wire, the particle experiences a change in magnetic field magnitude. In order to conserve its magnetic moment (also called the first adiabatic invariant), the particle's perpendicular kinetic energy increases in proportion with the magnetic field. When the perpendicular kinetic energy can no longer increase — that is, when all of the particle's kinetic energy is perpendicular — the particle bounces back. (If the particle's parallel kinetic energy is sufficiently large, it doesn't bounce, and instead precipitates into the atmosphere.) Particles undergoing bounce motion continuously move back and forth between the northern and southern hemispheres.

The third fundamental motion is drift motion. Over the course of a particle's cyclotron motion, the Earthward half of the orbit experiences a slightly stronger magnetic field (and thus a slightly smaller orbit radius). The net effect, called the gradient-curvature drift, is an azimuthal motion around Earth.

Characteristic timescales for each of the above motions depend on particle energy. Electron cyclotron motion is on the order of TODO: $\cdots$ in the ionosphere, and closer to TODO: $\cdots$ in the tail; ions gyrate slower by three orders of magnitude due to their larger mass. TODO: Bounce... Drift...

Wave-particle resonance arises when a particle's periodic motion matches with the frequency of a coincident electromagnetic wave[25, 65, 76, 87]. In the particle's rest frame, the wave then appears as a net electric field. This allows a net movement of energy between the wave and the particle. The interaction is analogous to a surfer moving along with — and being accelerated by — a wave in the ocean. Such resonance can arise for any of the three fundamental motions, or even for a combination of them.

In the present work, the waves in question are field line resonances (FLRs). An FLR is a standing harmonic on a geomagnetic field line. It can also be envisioned as a superposition of traveling waves, reflecting back and forth between its northern and southern foot points at the conducting ionosphere.

These waves travel at the Alfvén speed, v_A, defined per

$$v_A^2 \equiv \frac{B^2}{\mu_0 \rho} \qquad \text{or, equally,} \qquad v_A^2 \equiv \frac{1}{\mu_0 \epsilon_\perp} \tag{3.1}$$

Where B is the magnetic field magnitude, ρ is the mass density, and μ_0 is the magnetic constant. The perpendicular electric constant $\epsilon_\perp$ is analogous to the electric constant ϵ_0, and arises in cases (such as the magnetosphere) where a dielectric medium exhibits a preferred direction. In the magnetosphere, mass density and magnetic field strength depend strongly on position. As a result, the Alfvén speed may vary by several orders of magnitude over the length of a field line.

The fundamental equations of field line resonance were presented by Dungey in 1954[22]; since then, they have remained a topic of active study.

TODO: ...in no small part because they are not just relevant to space! Alfvén waves also show up in laboratory plasmas, which are hard to measure directly, and in all sorts of astrophysical contexts.

So-called ultra low frequency waves — of which FLRs are a subset — are categorized by morphology. Continuous (long-lived) pulsations are termed Pc, while irregular pulsations are called Pi. Within each are a number of frequency bands; see Table 3.1[46].

Table 3.1: IAGA Magnetic Pulsation Frequency Bands

	Pc1	Pc2	Pc3	Pc4	Pc5	Pi1	Pi2
Period (s)	0.2–5	5–10	10–45	45–150	150–600	1–40	40–150
Frequency (mHz)	200–5000	100–200	22–100	7–22	2–7	25–1000	7–25

TODO: Boundaries between wave bands are, in practice, not strict. They are sometimes fudged to better match phenomenological boundaries.

FLRs fall into the Pc3, Pc4, and Pc5 ranges. The present work focuses specifically on the Pc4 band: waves with periods of a minute or two. Frequencies in the Pc4 range typically coincide with Alfvén bounce times[1] near the plasmapause: $L \sim 4$ to $L \sim 6$[3, 18, 26, 57][2]. In fact, the large radial gradients in the Alfvén speed near the plasmapause act as an effective potential well, trapping FLRs[17, 51, 54, 55, 64, 90].

In addition to being radially localized, FLRs in the Pc4 frequency band (also called Pc4 pulsations, or just Pc4s) are localized in magnetic local time (MLT[3]). They have also been shown to occur preferrentially on the dayside, during storms or storm recovery[3, 18, 26, 53, 57, 99].

In the inner magnetosphere, the Alfvén frequency — and thus the frequency of FLRs — often coincides with integer or half-integer[4] multiples of particle drift frequencies[19]. The resulting wave-particle interactions can give rise to significant energization and radial diffusion of the particles. In some cases, the waves also include an electric field

[1] The Alfvén frequency is the inverse of the Alfvén bounce time: $\frac{2\pi}{\omega_A} \equiv \oint \frac{dz}{v_A}$.

[2] Not coincidentally, these are the same L-shells where the Van Allen Probes spend most of their time; see Chapter 8.

[3] Noon points toward the Sun and midnight away from it, with 06:00 and 18:00 at the respective dawn and dusk flanks.

[4] See Section 3.1.

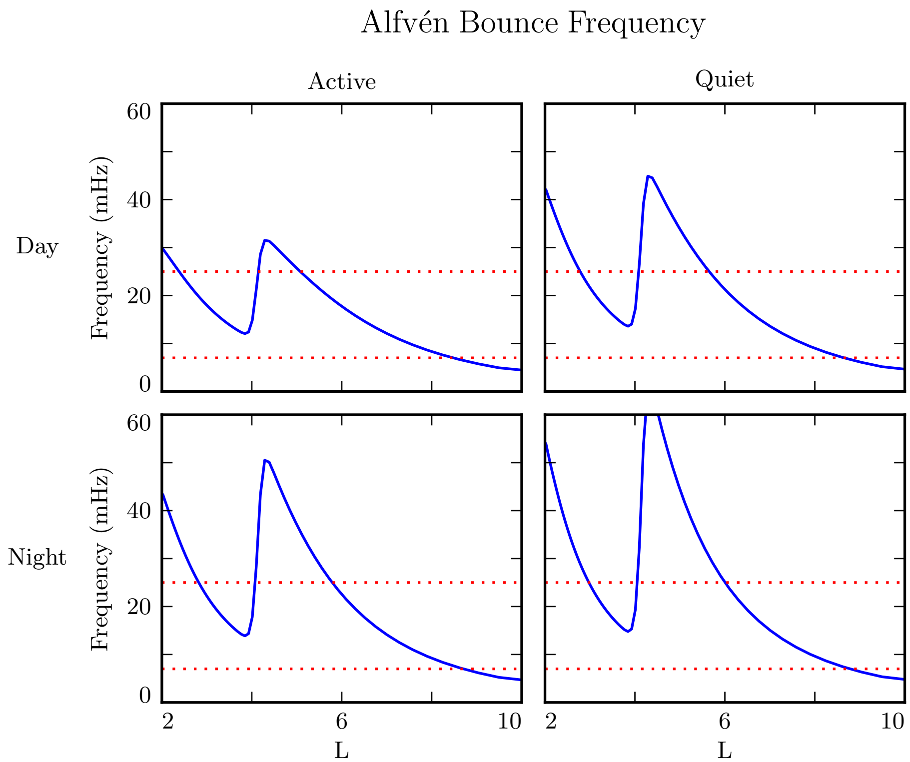

Figure 3.1: The above are bounce frequencies for an Alfvén wave moving back and forth along a geomagnetic field line. Alfvén speeds are computed based on profiles from Kelley[49], as discussed in Section 5.2. Notably, the bounce frequency depends significantly on the position of the plasmasphere, taken here to be at $L = 4$. Dotted lines indicate the Pc4 frequency range: 7 mHz to 25 mHz.

parallel to the background magnetic field, contributing to the precipitation of energetic particles into the neutral atmosphere[33, 34, 96, 106].

The present chapter introduces the structural characteristics of FLRs, how those characteristics affect wave behavior, and several unresolved questions related to that behavior.

TODO: The polarization of long-period Alfvén waves is rotated by $\sim 90°$ when passing through the ionosphere[42]. A wave that is azimuthally polarized in space is polarized north-south on the ground, and vice versa. It has been noted specifically that Pgs exhibit east-west polarized ground signatures[95].

3.1 Harmonic Structure

Wave structure along a geomagnetic field line is indicated by harmonic number. The first (or fundamental) harmonic has a wavelength twice as long as the field line. The electric field perturbation is zero at the ionospheric foot points of the field line, due to the conductivity of the ionosphere. For the first harmonic, this puts an electric field antinode at the equator, along with a node in the perpendicular[5] perturbation to the magnetic field. For the second harmonic, the electric field has a third node at the equator, which is accompanied by an antinode in the perpendicular magnetic field perturbation. Figure 3.2 shows a qualitative sketch of the first and second harmonics: a series of snapshots in time, in the rest frame of the wave. Perpendicular electric and magnetic field perturbations are shown in blue and red respectively.

A first-harmonic FLR that is periodic or localized in the azimuthal direction is conducive to drift-resonant wave-particle interactions[19, 77]. The particle is like a child on a swing: whenever the path of the particle (or child) gets close to the wave (parent), it gets a push, and always in the same direction. The wave fields spend half its time pointing the other direction, just as the parent must shift their weight backward to get ready for the next push, but at that point the particle (child) is far away.

Second-harmonic FLRs interact with particles through the drift-bounce resonance, which is slightly more complicated. As the particle drifts azimuthally, it also zig-zags north-south. The combination of those two periodic motions must align with the phase of the wave electric field. An example path is shown by the purple line in Figure 3.2: the particle experiences a rightward electric field throughout the wave's oscillation.

The drift and drift-bounce resonance conditions is written, respectively[91]:

$$\omega - m\omega_D = 0 \qquad \text{and} \qquad \omega - m\omega_D = \omega_B \tag{3.2}$$

[5] The parallel, or compressional, magnetic field exhibits the same nodes and antinodes as the perpendicular electric field[80].

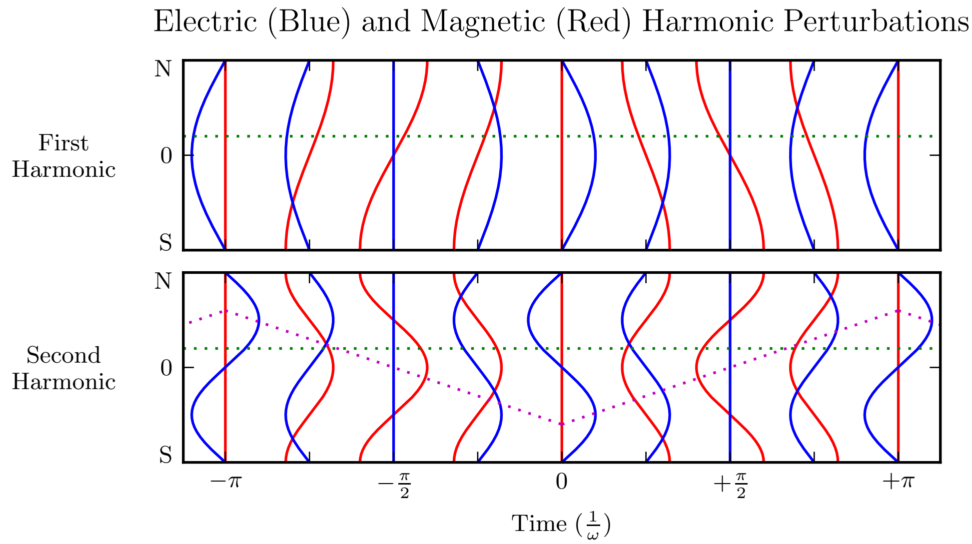

Figure 3.2: The first (or fundamental) harmonic has an an antinode in its perpendicular electric field (blue) at the equator, along with a node in its perpendicular magnetic field perturbation (red). A single satellite can identify the first harmonic by the relative phase of the electric and magnetic field perturbations: an observer north of the equator (green) will see the magnetic field perturbation lead the electric field by $\pm 90°$. The second harmonic is the opposite: it has an electric field node at the equator, and an observer north of the equator will see the magnetic field perturbation lag the electric field by $\mp 90°$. Top and bottom signs correspond to the poloidal (shown) and toroidal polarizations respectively. The purple line sketches the path of a particle in drift-bounce resonance; in the particle's rest frame, the electric field is always to the right.

Where ω is the frequency of the wave, ω_D and ω_B are the particle's drift and bounce frequencies respectively, and m is the wave's azimuthal modenumber, as discussed in Section 3.2.

In principle, the first and second harmonics can be distinguished by their frequencies, even from a single-point observation[16, 35]. In practice, however, this is not a reliable approach[92]. There are significant uncertainties surrounding the mass density profile — and thus the Alfvén speed profile — along a geomagnetic field line.

Harmonic structure can also be deduced by noting the phase offset between the wave magnetic field and its electric field (or the plasma velocity)[18, 95]. In Figure 3.2, the green line indicates an observer just north of the magnetic equator. For a wave polarized in the poloidal direction (see Section 3.3), the observer sees the electric field waveform offset from the magnetic field by a phase of $\pm 90°$, where the top sign is for odd modes and the bottom sign is for even modes. The signs are flipped for toroidally-polarized waves, and again for waves observed south of the equator.

TODO: Talk about imaginary Poynting flux? Standing waves don't move energy. Traveling waves do. In practice, everything is a superposition of the two.

Notably, the measurement of wave phase has only become viable with the advent of satellites carrying both electric and magnetic field instrumentation, such as THEMIS in 2007[4] and the Van Allen Probes[6] in 2012[88].

Strictly speaking, the the phase offset of the electric and magnetic fields does not provide the harmonic number — only its parity. It's reasonably safe to assume that an even mode is the second harmonic; the second harmonic is by far the most commonly observed[45, 85, 93], due in part to its excitement by the antisymmetric balloon instability[10, 12, 14, 87]. However, the distinction between the first and third harmonics is not always clear[15, 35]; this issue is discussed further in Chapter 8. Higher harmonics than that are not expected in the Pc4 frequency band.

TODO: Second-harmonic FLRs are unlikely to cause ground signatures[95].

3.2 Azimuthal Modenumber

The wavelength of an FLR in the azimuthal direction is indicated by its azimuthal modenumber. A wave with modenumber m has an azimuthal wavelength that spans $\frac{24}{m}$ hours in MLT.

Waves with small azimuthal modenumbers ($0 < m < 10$) are typically driven by broadband energy sources at the magnetosphere's boundary, such as variations in the solar wind pressure[20, 39, 50, 109, 110], sporadic magnetic reconnection[43], or Kelvin-Helmholtz waves on the magnetopause[11, 58, 86]. In the low-m regime, the shear and compressional Alfvén waves are coupled, which allows energy to move across field lines

[6]The Van Allen Probes were previously called RBSP, for Radiation Belt Storm Probes.

Figure 3.3: TODO: Large and small azimuthal modenumbers.

until the driving frequency lines up with the local Alfvén frequency[60]. Because of their broadband energy source, low-m FLRs often have a mishmash of frequencies present in their spectra[18], though the spectra are coherent in terms of harmonic[27].

When the azimuthal modenumber is large (or, equally, when the azimuthal wavelength is small), compressional propagation of Alfvén waves becomes evanescent, so the movement of energy is guided by magnetic field lines[16, 80][7]. As a result, FLRs must be driven from within the magnetosphere. Proposed energy sources include phase space gradients near the plasmapause[19], particularly as the plasmasphere refills after a storm or substorm[26, 56].

The atmosphere is known to attenuate waves with small spatial extent in the perpendicular direction[44, 104, 108]. As a result, FLRs may create no signature on the ground if

[7]Equally, the strength of a wave's parallel component hint at its modenumber, a point which is revisited in Chapter 8.

their azimuthal modenumber is large. For example, a recent paper by Takahashi shows a strong (2 nT at $L \sim 10$), clear resonance with $|m| \gtrsim 70$ and no corresponding ground signature[92].

Southwood[87] and Glassmeier[31] show that a low frequency wave passing through the ionosphere on its way to Earth will be attenuated per

$$\frac{B_E}{B_I} = \frac{\Sigma_H}{\Sigma_P} \exp\left(-m \frac{R_I - R_E}{R_E \sin\theta}\right) \tag{3.3}$$

Where B_E and B_I are the magnetic field strengths at R_E (Earth's surface, 6783 km geocentric) and R_I (the ionosphere, ∼6900 km geocentric) respectively. The integrated ionospheric Pedersen and Hall conductivities, Σ_P and Σ_H, are typically within a factor of two of one another. Field lines near the plasmapause can be traced to Earth at $\sin\theta \sim 0.4$. That is, by the time it reaches the ground, the magnetic field from an FLR with $m = 10$ is weaker by a factor of two; at $m = 100$, the factor is closer to 100.

3.3 Poloidal and Toroidal Polarizations

Based on polarization, each FLR can be classified as either poloidal or toroidal. The poloidal mode is a field line displacement in the meridional plane, as shown in Figure 3.4, with an accompanying electric field in the azimuthal direction. The toroidal mode's magnetic displacement is azimuthal, per Figure 3.5; the associated electric field is in the meridional plane.

Both poloidal and toroidal waves are noted for their ability to contribute to the energization and radial diffusion of trapped particles. The poloidal mode interacts more strongly, since its electric field is aligned with the trapped particles' drift motion. Poloidally-polarized waves are also more prone to creating magnetic signatures on the ground, due to ducting in the ionosphere[29, 37].

Toroidal modes have been shown to far outnumber poloidal modes[3]. Perhaps not coincidentally, poloidally-polarized waves rotate asymptotically to the toroidal mode[66, 67, 80]. Poloidal waves with low azimuthal modenumber — such as those driven by

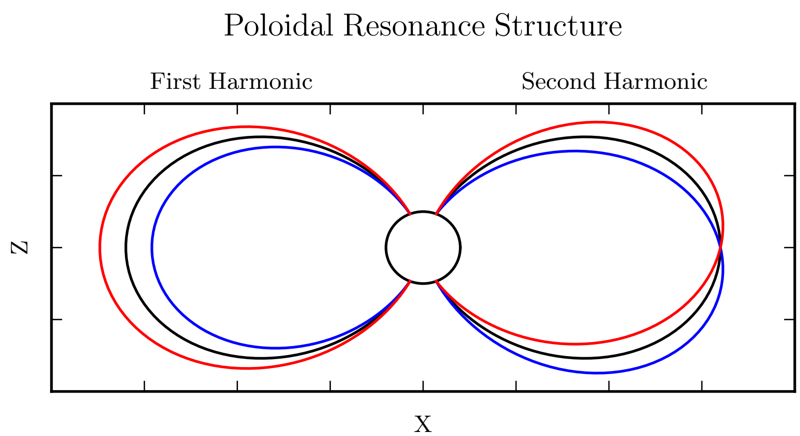

Figure 3.4: The poloidal resonance is a magnetic field in the meridional plane. The displacement is radial near the equator, and can be accompanied by enhancement in the parallel magnetic field near the ionosphere. The first harmonic is shown on the left, and the second harmonic on the right. Lines are colored red and blue only to contrast with the unperturbed black field line.

broadband sources at the magnetopause — rotate on timescales comparable to their oscillation periods.

TODO: Fishbone instability[13, 69]. Like the poloidal mode, but for lab plasmas.

TODO: Poloidal and toroidal modes are coupled by the ionospheric Hall conductivity[48]. The Hall conductivity also increases the "ringtime" of these resonances, allowing them to oscillate through the inductive process rather than be dissipated as Joule heating[102].

TODO: Toroidal modes show a clear frequency dependence with L. Poloidal modes less so. Citation... [27]?

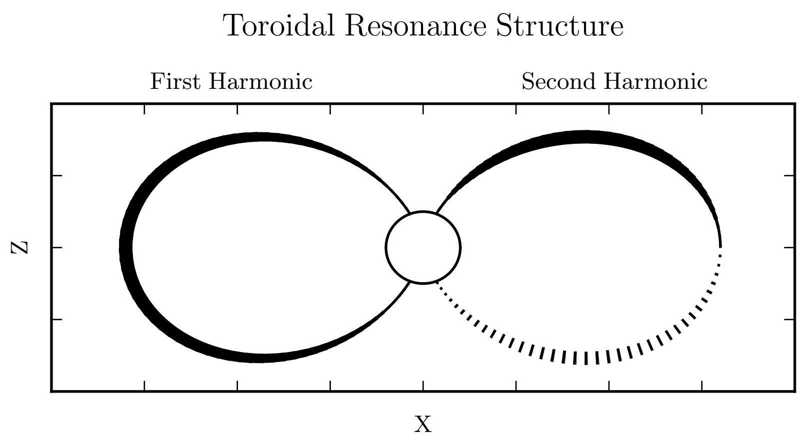

Figure 3.5: A toroidally-polarized FLR has a magnetic perturbation in the azimuthal direction, as shown. Bold lines are taken to be above the page, and dotted lines below the page, with the displacement indicated by the line's width. The first harmonic — where the entire field line oscillates in and out of the page — is shown on the left. The second harmonic is on the right, with northern and southern halves perturbed in opposite directions.

3.4 Giant Pulsations

The study of geomagnetic pulsations long predates satellites, sounding rockets, or even the word "magnetohydrodynamics"[8]. Large, regular oscillations in the magnetic field were noted as early as 1901[6]. Eventually, the term "giant pulsation," or Pg, arose to describe such pulsations.

On the ground, Pgs are notable for their strikingly sinusoidal waveforms, their eastward drifts, and their specific occurrence pattern: Pgs are typically seen pre-dawn, at latitudes of 60° to 70°. Pgs generally fall into the Pc4 frequency band[9]. Their harmonic structure was a source of controversy for decades, but recent multisatellite observations seem to be in agreement that they are odd harmonics, probably fundamental[32, 41, 52, 53, 91, 95]. They are poloidally polarized, with modenumbers $10 \lesssim m \lesssim 40$[30, 41, 77, 83, 95].

[8]The term was first used by Alfvén in the 1940s[2].

[9]The Pc4 range is periods of 45 s to 140 s, while Pgs are often said to range from 60 s to 200 s[8].

Whereas FLRs are waves in space which may produce ground signatures, "giant pulsation" refers to the ground signature specifically[10]. That is, Takahashi's satellite observation of a sinusoidal, morningside, high-m, fundamental poloidal resonance was not classified as a Pg because it did not produce a signal on the ground[92].

TODO: Pgs are localized to within $2°$ to $5°$ in latitude[72, 91, 100].

Due to their remarkably clear waveforms, Pgs are typically found by "visual inspection of magnetometer data"[72]. Over the course of the past century, a number of multi-year (sometimes multi-decade[8]) surveys have totaled nearly one thousand Pg events. On average, a ground magnetometer near $66°$ magnetic latitude observes $\sim$10 Pg events per year[8, 40, 82, 89]. Observations are not distributed uniformly; rather, giant pulsations become more common near the equinox and during times of low solar activity.

Unlike Pc4 pulsations in general, Pgs show no particular correlation with storm phase[72]. However, they do often occur as the magnetosphere recovers from a substorm[72, 83].

3.5 Motivations for the Present Work

A great deal has been learned — and continues to be learned — through observations of field line resonance. However, the cost-to-benefit ratio is climbing. As summarized in the sections above, FLR behavior depends significantly on harmonic structure, azimuthal modenumber, and polarization — not to mention frequency, spectral width, and so on. With each degree of freedom comes the necessity for an additional simultaneous observation.

Similarly, as FLRs have been shown to depend on ever-more-specific magnetospheric conditions, analytical techniques have fallen out of favor. The height-resolved ionosphere, the multidimensional Alfvén speed profile, and the inconvenient geometry combine to create a problem beyond the reasonable purview of pencil and paper.

That is, the topic of field line resonance is ripe for numerical modeling.

[10] Historically, the wave designations shown in Table 3.1 all referred to ground phenomena. Over time, they have come to describe satellite observations as well, including those without corresponding signatures on the ground.

Past models of the magnetosphere have been limited in their consideration of FLRs. Reasons include overly-simplified treatment of the ionospheric boundary, no consideration of the plasmapause, limited range in m, and the inability to compute ground signatures. Chapter 5 presents a model which addresses these issues, allowing the computation of field line resonance with unparalleled attention to realism.

The model allows a bird's-eye view of the structure and evolution of FLRs. As such, not only can several open questions be addressed, but their answers serve to unify a number of seemingly-disparate properties described in the sections above.

The rotation of poloidally-polarized waves to the toroidal mode is investigated. Particular attention is paid to the importance of azimuthal modenumber and ionospheric conductivity. The interplay between said rotation and the transport of energy across field lines — which also depends on azimuthal modenumber — is considered as well.

By their nature, drifting particles have the potential to spur wave-particle interactions at all MLT. However, Pc4 observations are strongly peaked on the dayside. In a 2015 paper, Dai notes, "It is not clear why noncompressional [high-m] Pc4 poloidal waves, which are presumably driven by instability within the magnetosphere, preferrentially occur on the dayside"[18]. Motoba, later that year, echoes, "It is unclear whether other generation mechanisms of fundamental standing waves ... can explain the localization of Pgs in local time"[72]. This, too, is considered numerically: to what degree is field line resonance affected by the (day-night asymmetric) conditions of the ionosphere?

TODO: Transition... With the above in mind, what data would be super helpful?

It's been shown that a ground magnetometer 66° north of the magnetic equator observes ∼10 Pg events per year. It's also been shown that poloidal Pc4s are rare compared to toroidal ones, and that most poloidal Pc4s are even harmonics. However, little attention has been paid to how these rates line up with one another. Given the relative occurrence rate of poloidal and toroidal waves, of odd and even harmonics, and of diffuse and sharp spectral peaks, just how unusual are giant pulsations?

Chapter 4

Waves in Cold Resistive Plasma

Before delving into the implementation of the numerical model, it's instructive to consider the fundamental equations of waves in a cold, resistive plasma. Specifically, the present chapter is concerned with waves much slower than the electron cyclotron frequency. High-frequency waves such as the L and R modes are beyond the scope of the present work — and, in fact, beyond the limits of the model described in Chapter 5.

The evolution of electric and magnetic fields is governed by Ampère's law and Faraday's law. Notably, the present work takes the linearized versions of Maxwell's equations; the vectors $\underline{E}$ and $\underline{B}$ indicate perturbations above the zeroth-order magnetic field.

$$\underline{\underline{\epsilon}} \cdot \frac{\partial}{\partial t}\underline{E} = \frac{1}{\mu_0}\nabla \times \underline{B} - \underline{J} \qquad\qquad \frac{\partial}{\partial t}\underline{B} = -\nabla \times \underline{E} \tag{4.1}$$

Current follows Ohm's law. For currents perpendicular to the background magnetic field, Kirchhoff's formulation is sufficient. Conductivity is much higher along the magnetic field lines[1], so it's appropriate to also include the electron inertial term[2].

$$0 = \underline{\underline{\sigma}}_\perp \cdot \underline{E}_\perp - \underline{J}_\perp \qquad\qquad \frac{1}{\nu}\frac{\partial}{\partial t}J_z = \sigma_0 E_z - J_z \tag{4.2}$$

[1] The dipole coordinate system is defined rigorously in Section 5.1; at present, it's sufficient to take $\hat{z}$ parallel to the zeroth-order magnetic field, and $\hat{x}$ and $\hat{y}$ perpendicular to $\hat{z}$ (and to each other).

[2] Electron inertial effects are not included in the model described in Chapter 5, or in the results in Chapter 7; however, their implementation and impact are explored in Chapter 6.

Derivatives in Equations (4.1) and (4.2) can be evaluated by performing a Fourier transform. They can then be combined, eliminating the magnetic field and current terms.

$$\begin{aligned} 0 &= \underline{E}_\perp + \frac{v_A^2}{\omega^2}\left(\underline{k}\times\underline{k}\times\underline{E}\right)_\perp + \frac{i}{\epsilon_\perp\omega}\underline{\underline{\sigma}}_\perp\cdot\quad\underline{E}_\perp \\ 0 &= E_z \;+ \frac{c^2}{\omega^2}\left(\underline{k}\times\underline{k}\times\underline{E}\right)_z \;+ \frac{i\omega_P^2}{\omega\left(\nu-i\omega\right)}E_z \end{aligned} \tag{4.3}$$

The speed of light, Alfvén speed (including the displacement current correction), plasma frequency, and parallel conductivity are defined in the usual way:

$$c^2 \equiv \frac{1}{\mu_0\epsilon_0} \qquad v_A^2 \equiv \frac{1}{\mu_0\epsilon_\perp} \qquad \omega_P^2 \equiv \frac{ne^2}{m_e\epsilon_0} \qquad \sigma_0 \equiv \frac{ne^2}{m_e\nu} \tag{4.4}$$

Where the perpendicular dielectric constant $\epsilon_\perp$ is analogous to the electric constant ϵ_0, but for electric fields which are perpendicular to the preferred direction of the dielectric medium. As noted in Equation (3.1), $\epsilon_\perp \equiv \frac{\rho}{B^2}$ where ρ is the mass density and B is the magnitude of the (zeroth-order) magnetic field.

Using the vector identity $\underline{k}\times\underline{k}\times\underline{E} = \underline{k}\,\underline{k}\cdot\underline{E} - k^2\underline{E}$, Equation (4.3) can be reassembled into a single expression,

$$0 = \left(\underline{\underline{\mathbb{I}}} + \frac{1}{\omega^2}\underline{\underline{V}}^2\cdot\underline{k}\,\underline{k} - \frac{k^2}{\omega^2}\underline{\underline{V}}^2 + \frac{i}{\omega}\underline{\underline{\Omega}}\right)\cdot\underline{E} \tag{4.5}$$

Where $\underline{\underline{\mathbb{I}}}$ is the identity tensor and in x-y-z coordinates,

$$\underline{\underline{V}}^2 \equiv \begin{bmatrix} v_A^2 & 0 & 0 \\ 0 & v_A^2 & 0 \\ 0 & 0 & c^2 \end{bmatrix} \qquad \text{and} \qquad \underline{\underline{\Omega}} \equiv \begin{bmatrix} \frac{\sigma_P}{\epsilon_\perp} & \frac{-\sigma_H}{\epsilon_\perp} & 0 \\ \frac{\sigma_H}{\epsilon_\perp} & \frac{\sigma_P}{\epsilon_\perp} & 0 \\ 0 & 0 & \frac{\omega_P^2}{(\nu-i\omega)} \end{bmatrix} \tag{4.6}$$

In Equation (4.5), the expression in parentheses is the dispersion tensor. Nontrivial solutions exist only when its determinant is zero. This gives rise to a seventh-order polynomial in ω, so rather than a direct solution it's necessary to consider limits of specific interest.

Without loss of generality, the wave vector $\underline{k}$ may be taken to lie in the x-z plane — that is, with $k_y = 0$. The distinction between the two perpendicular directions is discussed in Section 4.4.

4.1 Guided Propagation

The wave vector of a field line resonance aligns closely to the background magnetic field. By supposing that the two align exactly (that is, taking $k_x = 0$), the parallel and perpendicular components of the dispersion relation are decoupled.

The parallel-polarized component — that is, the solution when $E_x = E_y = 0$ — is quadratic, and thus can be solved directly.

$$0 = \omega^2 + i\nu\omega - \omega_P^2 \qquad \text{so} \qquad \omega = -\frac{i\nu}{2} \pm \sqrt{\omega_P^2 - \frac{\nu^2}{4}} \tag{4.7}$$

It bears noting that the plasma frequency is large — not just compared to Pc4 frequencies, but even compared to the collision frequencies in the ionosphere[3].

Expanding Equation (4.7) with respect to large ω_P, the dispersion relation becomes

$$\omega^2 = \omega_P^2 \pm i\nu\omega_P + ... \tag{4.8}$$

Equation (4.8) can hardly be called a wave, as it does not depend on the wave vector $\underline{k}$. Rather, it is the plasma oscillation[4]: electrons vibrating in response to a charge separation along the background magnetic field.

The plasma oscillation is not specifically relevant to the study of field line resonance. The two phenomena are separated by six orders of magnitude in frequency. The topic

[3]The collision frequency may match or exceed the plasma frequency for a thin slice at the bottom of the ionosphere, where the density of neutral atoms is large; however, it falls off quickly. Above an altitude of 200 km, conservatively[75], the plasma frequency exceeds the collision frequency by an order of magnitude or more.

[4]The plasma oscillation is also called the Langmuir wave, after Irving Langmuir.

is revisited in Chapter 6 insomuch as it is inseparable from the electron inertial effects in Ohm's law.

The perpendicular ($E_z = 0$) components of the dispersion relation give an expression quartic in ω.

$$0 = \omega^4 + 2i\frac{\sigma_P}{\epsilon_\perp}\omega^3 - \left(2k_z^2 v_A^2 + \frac{\sigma_P^2 + \sigma_H^2}{\epsilon_\perp^2}\right)\omega^2 - 2ik_z^2 v_A^2 \frac{\sigma_P}{\epsilon_\perp}\omega + k_z^4 v_A^4 \tag{4.9}$$

Like the parallel-polarized component above, Equation (4.9) can be solved directly. Noting that $\pm$ and $\oplus$ are independent,

$$\omega = \left(\frac{\pm\sigma_H - i\sigma_P}{2\epsilon_\perp}\right) \oplus \sqrt{k_z^2 v_A^2 + \left(\frac{\pm\sigma_H - i\sigma_P}{2\epsilon_\perp}\right)^2} \tag{4.10}$$

Also like the parallel-polarized component, the exact solution is less useful than its Taylor expansion. The Pedersen and Hall conductivities are large near the ionospheric boundary, but fall off quickly; for the vast majority of the field line, the ratios $\frac{\sigma_P}{\epsilon_\perp}$ and $\frac{\sigma_H}{\epsilon_\perp}$ are small compared to field line resonance frequencies. Expanding with respect to small conductivity gives

$$\omega^2 = k_z^2 v_A^2 \oplus k_z v_A \frac{\sigma_H \pm i\sigma_P}{\epsilon_\perp} + ... \tag{4.11}$$

This is the shear Alfvén wave, with a shift to its frequency due to the conductivity of the ionosphere. It travels along the background magnetic field like a bead on a string, with electric and magnetic field perturbations perpendicular to the magnetic field line (and to one another).

4.2 Compressional Propagation

The partner to guided motion is compressional motion; in order for energy to move across field lines, the wave vector must have a component perpendicular to $\hat{z}$. If the wave vector is completely perpendicular to the magnetic field line ($k_z = 0$), the parallel and perpendicular components of the dispersion relation decouple, as in Section 4.1.

The parallel-polarized ($E_x = E_y = 0$) component of the dispersion relation is

$$0 = \omega^3 + i\nu\omega^2 - \left(k_x^2 c^2 + \omega_P^2\right)\omega - ik_x^2 c^2 \nu \tag{4.12}$$

Equation (4.12) can be solved directly, though its solution (as a cubic) is far too long to be useful. Expanding with respect to the large plasma frequency, gives

$$\omega^2 = k^2 c^2 + \omega_P^2 - i\nu\omega_P + ... \tag{4.13}$$

This is the O mode, a compressional wave with an electric field perturbation along the background magnetic field. Like the plasma oscillation discussed in Section 4.1, its frequency is very large compared to that of a field line resonance.

The perpendicular-polarized ($E_z = 0$) component of the compressional dispersion relation is also cubic.

$$0 = \omega^3 + 2i\frac{\sigma_P}{\epsilon_\perp}\omega^2 - \left(2k_x^2 v_A^2 + \frac{\sigma_P^2 + \sigma_H^2}{\epsilon_\perp^2}\right)\omega - ik_x^2 v_A^2 \frac{\sigma_P}{\epsilon_\perp} \tag{4.14}$$

A wave moving across magnetic field lines near the ionospheric boundary will encounter large $\frac{\sigma_P}{\epsilon_\perp}$ and $\frac{\sigma_H}{\epsilon_\perp}$, while at moderate to high altitudes those ratios will be small. Solving Equation (4.14) in those two limits respectively gives:

$$\omega^2 = k_x^2 v_A^2 \pm ik_x v_A \frac{\sigma_P}{\epsilon_\perp} + ... \qquad \text{and} \qquad \omega^2 = k_x^2 v_A^2 + \left(\frac{\sigma_H \pm i\sigma_P}{\epsilon_\perp}\right)^2 + ... \tag{4.15}$$

At first glance, both limits of Equation (4.15) appear to describe a compressional Alfvén wave. The magnetic perturbation is along the background magnetic field — indicating compression of the frozen-in plasma — while the electric field perturbation is perpendicular to both the magnetic field and the wave vector.

However, in the high-conductivity limit, the parenthetical term actually dominates the Alfvén term, taking values as large as $\sim 10^6$ Hz. Waves at such frequencies are beyond the scope of the present work. As a matter of curiosity, however, it bears noting that (as long as $\nu \ll 10^6$ Hz) $\frac{\sigma_H}{\epsilon_\perp}$ reduces to the electron cyclotron frequency, $\frac{eB}{m_e}$.

4.3 High Altitude Limit

In the limit of large radial distance, it's reasonable to take the collision frequency to zero; doing so also neglects the Pedersen and Hall conductivities.

Whereas in Sections 4.1 and 4.2 it was the parallel-polarized component of the dispersion relation that factored out from the other two, the high altitude limit decouples the component polarized out of the x-z plane. The y-polarized dispersion ($E_x = E_z = 0$) is simply:

$$\omega^2 = k^2 v_A^2 \tag{4.16}$$

Equation (4.16) describes an Alfvén wave with an arbitrary angle of propagation. Depending on the angle between the wave vector and the background magnetic field, it could be guided, compressional, or somewhere in between. Regardless of propagation angle, the electric field perturbation is perpendicular to both the direction of propagation and the magnetic field perturbation.

The other two components (from $E_y = 0$) of the high altitude dispersion tensor give an expression quadratic in ω^2:

$$0 = \omega^4 - \left(k_x^2 c^2 + k_z^2 v_A^2 + \omega_P^2\right)\omega^2 + k_z^2 v_A^2 \omega_P^2 \tag{4.17}$$

Which can be solved for

$$\omega^2 = \frac{1}{2}\left(k_x^2 c^2 + k_z^2 v_A^2 + \omega_P^2\right) \pm \sqrt{\frac{1}{4}\left(k_x^2 c^2 + k_z^2 v_A^2 + \omega_P^2\right)^2 - k_z^2 v_A^2 \omega_P^2} \tag{4.18}$$

Noting again that ω_P is very large, the two roots can be expanded to

$$\omega^2 = k_z^2 v_A^2 \left(1 - \frac{k_x^2 c^2 + k_z^2 v_A^2}{\omega_P^2}\right) + ... \qquad \text{and} \qquad \omega^2 = k_x^2 c^2 + k_z^2 v_A^2 + \omega_P^2 + ... \tag{4.19}$$

The first solution of Equation (4.19) is a shear Alfvén wave, as in Equation (4.11). Notably, this form arises only when the parenthetical quantity is close to unity — as it is for FLRs. The inertial limit, where frequencies are close to the plasma frequency, is beyond the scope of the present work. For that same reason, the second solution (which describes an oscillation faster than the plasma frequency) is not further considered.

4.4 Implications to the Present Work

The present section's findings carry three significant implications for the present work.

First — with the exception of the plasma oscillation and similar modes, which are revisited in Chapter 6 — waves propagate at the Alfvén speed. This, in combination with the grid configuration, will constrain the time step that can be used to model them numerically. The time step must be sufficiently small that information traveling at the Alfvén speed cannot "skip over" entire grid cells[5].

Second, the results of the present section allow an estimate of the magnitude of parallel electric field that might be expected from a field line resonance compared to its perpendicular electric field. Between the full dispersion tenfor form in Equation (4.5) and the Alfvén wave described by Equation (4.19),

$$\left|\frac{E_z}{E_x}\right| = \frac{k_x k_z c^2}{\omega^2 - k_x^2 c^2 - \omega_P^2} \sim \frac{k^2 c^2}{\omega_P^2} \tag{4.20}$$

In essence, the relative magnitudes of the parallel and perpendicular electric fields should be in proportion to the square of the relative magnitudes of the electron inertial length

[5]As is the convention, the time step is scaled down from the smallest Alfvén zone crossing time by a Courant factor, typically 0.1, meaning that it takes at least ten time steps to cross a grid cell.

(1 km to 100 km) and the wavelength ($\sim 10^5$ km). That is, parallel electric fields should be smaller than the perpendicular electric fields by six or more orders of magnitude.

Finally, the dispersion relations shown above indicate how the behavior of a field line resonance should behave as the azimuthal modenumber becomes large.

Whereas the shear Alfvén wave's dispersion relation depends only on the parallel component of the wave vector, the compressional Alfvén wave depends on its magnitude: $\omega^2 = k^2 v_A^2$. If the frequency is smaller than kv_A, the wave will become evanescent. The wave vector's magnitude can be no smaller than its smallest component, however, and the azimuthal component scales with the azimuthal modenumber: $k_y \sim \frac{m}{2\pi r}$.

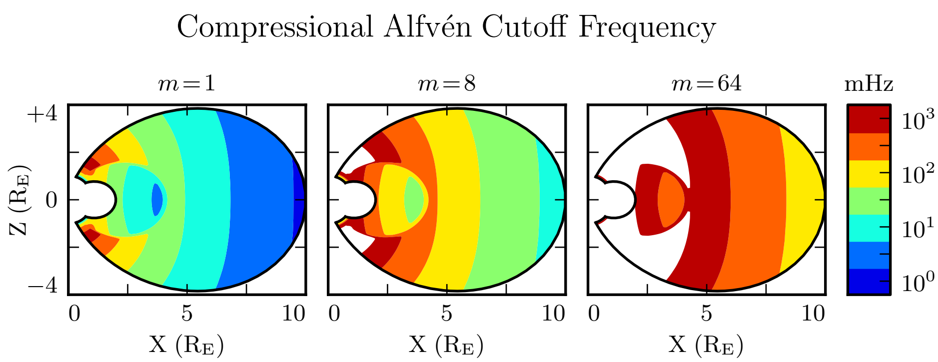

Figure 4.1: Taking $k_y \sim \frac{m}{2\pi r}$ as a lower bound for the magnitude of the wave vector, the above figure demonstrates the lowest frequency at which compressional Alfvén waves may propagate as a function of position and m. Regions shown in white are off the color scale — they have a lower bound on the order of 10^4 mHz or more. The above Alfvén frequency profile is from Kelley[49], for quiet dayside conditions, as discussed in Section 5.2.

This imposes a frequency cutoff on compressional Alfvén waves which scales with the azimuthal modenumber, as shown in Figure 4.1. At small values of m, most of the magnetosphere is conducive to compressional Alfvén waves in the Pc4 frequency range. As m increases, and the wave vector with it, the inner magnetosphere becomes increasingly inaccessible to them.

Chapter 5

“Tuna Half” Dimensional Model

The present section describes the implementation of Tuna, a new two and a half dimensional Alfvén wave code based largely on work by Lysak[59, 63].

The half-integer dimensionality refers to the fact that Tuna's spatial grid resolves a two-dimensional slice of the magnetosphere, but that electric and magnetic fields — as well as their curls — are three-dimensional vectors. This apparent contradiction is reconciled by the use of a fixed azimuthal modenumber, m. Electric and magnetic fields are taken to be complex-valued, varying azimuthally per $\exp(im\phi)$; derivatives with respect to ϕ are then replaced by a factor of im.

Unlike a fully three-dimensional code, Tuna cannot resolve the evolution of wave structures in the azimuthal direction. Furthermore, the model does not allow coupling between the dayside and nightside magnetospheres. What Tuna does offer is efficiency. The model's economical geometry allows it to include a realistic Earthward boundary: grid spacing on the order of 10 km, a height-resolved ionospheric conductivity tensor, and even the computation of magnetic field signatures at the ground. Such features are computationally infeasbile for a large global code.

Tuna was developed with field line resonance in mind. As discussed in Chapter 3, such waves are azimuthally localized, minimizing the importance of Tuna's missing half dimension. Moreover, because field line resonances are known to be affected by both the ionosphere and the plasmasphere, a faithful treatment of the inner magnetosphere is a crucial part of studying them numerically.

Perhaps the most exciting feature of Tuna is its novel driving mechanism: ring current perturbation. Codes similar to Tuna have traditionally been driven using compressional pulses at the outer boundary[59, 63, 102, 103]. This has precluded the investigation of waves with large azimuthal modenumber — such as giant pulsations — which are guided, and thus must be driven from within the magnetosphere.

TODO: The dipole geometry isn't super new, but it's not widely used. The height-resolved ionosphere is new and exciting! Ground signatures are new and exciting!

TODO: The support software — the driver and the plotter — are also significant. Do they get mentioned here? Does the Git repository where the code can be accessed get mentioned here?

5.1 Coordinate System

Field line resonance has traditionally been modeled by straightening the field lines into a rectangular configuration[22, 66], by unrolling the azimuthal coordinate into a cylindrical coordinate system[80], or through the use of dipole coordinates[79][1]:

$$x \equiv -\frac{\sin^2\theta}{r} \qquad\qquad y \equiv \phi \qquad\qquad z \equiv \frac{\cos\theta}{r^2} \tag{5.1}$$

Where r, θ, and ϕ take on their usual spherical meanings of radial distance, colatitude, and azimuthal angle respectively.

The dipole coordinate x is constant over each equipotential shell[2], y is azimuthal angle, and z indexes each field line from south to north. The unit vectors $\hat{x}$, $\hat{y}$, and $\hat{z}$ point

[1] The dipole coordinates x, y and z are perhaps more commonly named μ, ϕ, and ν respectively; however, in the present work, μ and ν take other meanings.

[2] In fact, x is inversely proportional to the McIlwain parameter L.

in the crosswise[3] (radially outward at the equator), azimuthal (eastward), and parallel (northward at the equator) directions respectively.

Notably, the dipole coordinates in Equation (5.1) are normal to one another. While mathematically convenient, they do not readily accommodate a fixed-altitude boundary at the ionosphere, nor do they allow the dipole magnetic field to intersect the boundary at an oblique angle, as Earth's field does. As a solution, a nonorthogonal set of dipole coordinates was developed numerically by Proehl[78], then formalized analytically by Lysak[59] in terms of their contravariant components:

$$u^1 = -\frac{R_I}{r}\sin^2\theta \qquad\qquad u^2 = \phi \qquad\qquad u^3 = \frac{R_I^2}{r^2}\frac{\cos\theta}{\cos\theta_0} \tag{5.2}$$

Above, R_I is the position of the ionosphere relative to Earth's center; it's typically taken to be $1\,\mathrm{R_E} + 100\,\mathrm{km}$.

Like the dipole coordinates x, y, and z, Lysak's coordinates u^1, u^2, and u^3 correspond to L-shell, azimuthal angle, and position along a field line respectively. However, compared to z, u^3 has been renormalized using the invariant colatitude[4] θ_0. As a result, u^3 takes the value $+1$ at the northern ionospheric boundary and -1 at the southern ionospheric boundary for all field lines.

Because Lysak's coordinate system is not orthogonal[5], it's necessary to consider covariant and contravariant basis vectors separately.

$$\hat{e}_i \equiv \frac{\partial}{\partial u^i}\underline{x} \qquad\qquad \hat{e}^i \equiv \frac{\partial}{\partial \underline{x}}u^i \tag{5.3}$$

Covariant basis vectors $\hat{e}_i$ are normal to the curve defined by constant u^i, while contravariant basis vectors $\hat{e}^i$ are tangent to the coordinate curve (equivalently, $\hat{e}^i$ is normal

[3] In the context of in situ measurements taken near the equatorial plane, $\hat{x}$ is referred to as the radial direction; however, the present work extends the dipole grid to low altitudes, where $\hat{x}$ can be more horizontal than vertical. The term "crosswise" is meant to indicate that $\hat{x}$ is defined by the cross product of $\hat{y}$ and $\hat{z}$.

[4] The invariant colatitude is the colatitude θ at which a field line intersects the ionosphere. It is related to the McIlwain parameter by $\cos\theta_0 \equiv \sqrt{1 - \frac{R_I}{L}}$.

[5] Curves of constant u^1 and curves of constant u^3 can intersect at non-right angles.

to the plane defined by constant u^j for all $j \neq i$). These vectors are reciprocal[6] to one another, and can be combined to give components of the metric tensor g[21].

$$\hat{e}^i \cdot \hat{e}_j = \delta^i_j \qquad\qquad g_{ij} \equiv \hat{e}_i \cdot \hat{e}_j \qquad\qquad g^{ij} \equiv \hat{e}^i \cdot \hat{e}^j \tag{5.4}$$

The metric tensor allows rotation between covariant and contravariant representations of vectors.

$$A_i = g_{ij} A^j \quad \text{and} \quad A^i = g^{ij} A_j \quad \text{where} \quad A_i \equiv A \cdot \hat{e}_i \quad \text{and} \quad A^i \equiv A \cdot \hat{e}^i \tag{5.5}$$

In addition, the determinant of the metric tensor is used to define cross products and curls[7].

$$(A \times B)^i = \frac{\varepsilon^{ijk}}{\sqrt{g}} A_j B_k \quad \text{and} \quad (\nabla \times A)^i = \frac{\varepsilon^{ijk}}{\sqrt{g}} \frac{\partial}{\partial u^j} A_k \quad \text{where} \quad g \equiv \det g \tag{5.6}$$

Explicit forms of the basis vectors and metric tensor can be found in the appendix of Lysak's 2004 paper[59]. At present, it's sufficient to note the mapping between Lysak's basis vectors and the usual dipole unit vectors.

$$\hat{x} = \frac{1}{\sqrt{g^{11}}} \hat{e}^1 \qquad\qquad \hat{y} = \frac{1}{\sqrt{g^{22}}} \hat{e}^2 \qquad\qquad \hat{z} = \frac{1}{\sqrt{g_{33}}} \hat{e}_3 \tag{5.7}$$

TODO: Do these need to be written out? Referring people to the code, which will be in a public Git repository, is also a possibility.

The basis vectors can also be mapped to the spherical unit vectors, though Equation (5.8) is valid only at the ionospheric boundary.

$$\hat{\theta} = \frac{1}{\sqrt{g_{11}}} \hat{e}_1 \qquad\qquad \hat{\phi} = \frac{1}{\sqrt{g_{22}}} \hat{e}_2 \qquad\qquad \hat{r} = \frac{1}{\sqrt{g^{33}}} \hat{e}^3 \tag{5.8}$$

[6] The symbol δ^i_j is the Kronecker delta; the present work also makes use of the Levi-Civita symbol ε^{ijk} and Einstein's convention of implied summation over repeated indeces[24].

[7] The square root of the determinant of the metric tensor is called the Jacobian. It's sometimes denoted using the letter J, which is reserved for current in the present work.

The coordinates converge at the equatorial ionosphere, so an inner boundary is necessary to maintain finite grid spacing. It's typically placed at $L = 2$. The outer boundary is at $L = 10$. The dipole approximation of Earth's magnetic field is tenuous at the outer boundary (particularly on the dayside); however, in practice, wave activity is localized inside $L \sim 7$. The grid is spaced uniformly in u^1, which gives finer resolution close to Earth and coarser resolution at large distances.

Spacing in u^3 is set by placing grid points along the outermost field line. The points are closest together at the ionosphere, and grow towards the equator. The spacing increases in a geometric fashion, typically by $3\,\%$.

Typically, Tuna uses a grid 150 points in u^1 by 350 points in u^3. The result is a resolution on the order of $10\,\mathrm{km}$ at the ionosphere, which increases to the order of $10^3\,\mathrm{km}$ at the midpoint of the outermost field line.

There are no grid points in u^2 due to the two-and-a-half-dimensional nature of the model. Fields are assumed to vary as $\exp\left(imu^2\right)$ — equally, $\exp(im\phi)$ — so derivatives with respect to u^2 are equivalent to a factor of im. In effect, the real component of each field is azimuthally in phase with the (purely real) driving, while imaginary values represent behavior that is azimuthally offset.

The simulation's time step is set based on the grid spacing. As is the convention, δt is set to match the smallest Alfvén zone crossing time, scaled down by a Courant factor (typically 0.1). It bears noting that the smallest crossing time need not correspond to the smallest zone; the Alfvén speed peaks several thousand kilometers above Earth's surface, in the so-called Ionospheric Alfvén Resonator[63]. A typical time step is on the order of $10^{-5}\,\mathrm{s}$.

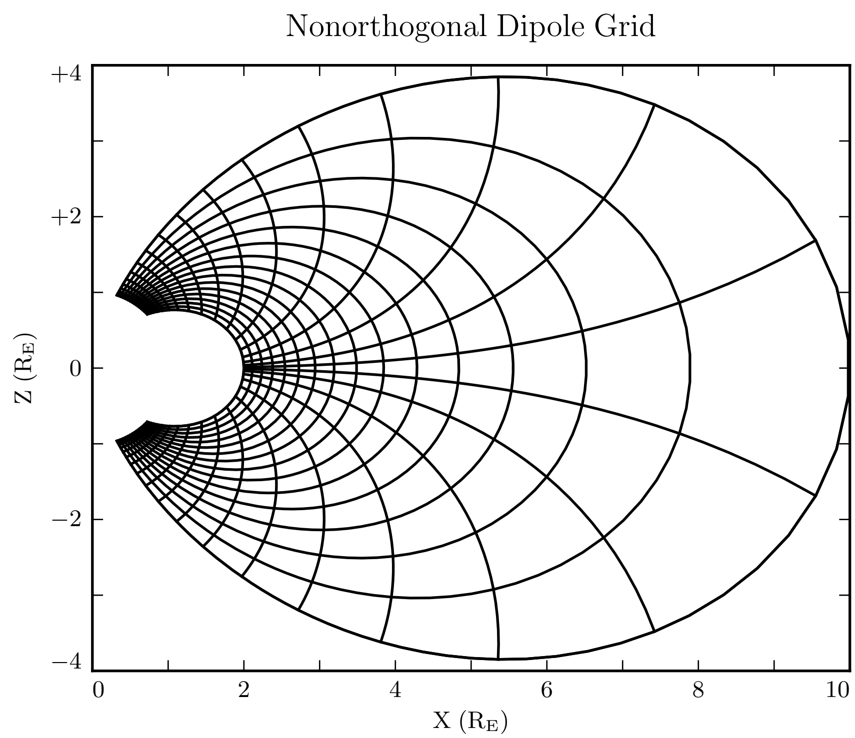

Figure 5.1: The model's nonorthorthogonal dipole grid. Every fifth point is shown in each direction. The high concentration of grid points near Earth's equator is a consequence of the coordinate system, which converges at the equatorial ionosphere. Earth (not shown) is centered at the origin with unit radius.

5.2 Physical Parameter Profiles

Tuna models Earth's magnetic field to be an ideal dipole, so the zeroth-order field strength is written in the usual form:

$$\underline{B}_0 = 3.1 \times 10^4 \,\mathrm{nT} \left(\frac{R_E}{r} \right)^3 \left(2 \cos\theta \, \hat{r} - \sin\theta \, \hat{\theta} \right) \tag{5.9}$$

Number density is taken to be the sum of an inverse-radial-dependent auroral profile and a plasmaspheric profile dependent on the L-shell[63]:

$$n = n_{AZ} \frac{r_{AZ}}{r} + n_{PS} \exp\left(\frac{-L}{L_{PS}}\right) \left(\frac{1}{2} - \frac{1}{2} \tanh \frac{L - L_{PP}}{\delta L_{PP}}\right) \tag{5.10}$$

Where typical values are shown in Table 5.1.

Table 5.1: Typical Parameters for the Tuna Density Profile

Variable	Value	Description
L_{PS}	1.1	Scale L of the plasmasphere.
L_{PP}	4.0	Location of the plasmapause.
δL_{PP}	0.1	Thickness of the plasmapause.
n_{AZ}	10 /cm^3	Number density at the base of the auroral zone.
n_{PS}	10^4 /cm^3	Number density at the base of the plasmasphere.
r_{AZ}	1 $\mathrm{R_E}$	Scale height of the auroral density distribution.

The perpendicular component of the electric tensor, $\epsilon_\perp$, is computed based on Kelley's[49] tabulated low-density values, ϵ_K, which are adjusted to take into account the effects of high density in the plasmapause.

$$\epsilon_\perp = \epsilon_K + \frac{Mn}{B_0^2} \tag{5.11}$$

Where M is the mean molecular mass, which is large ($\sim$28 u) at 100 km altitude, then drops quickly (down to 1 u by $\sim$1000 km)[63].

The Alfvén speed profile is computed from the perpendicular electric constant in the usual way, $v_A^2 \equiv \frac{1}{\mu_0 \epsilon_\perp}$. This form takes into account the effect of the displacement current, which becomes important in regions where the Alfvén speed approaches the speed of light.

While the density profile is held constant for all runs discussed in the present work, the Alfvén speed profile is not. Four different profiles are used for the low-density

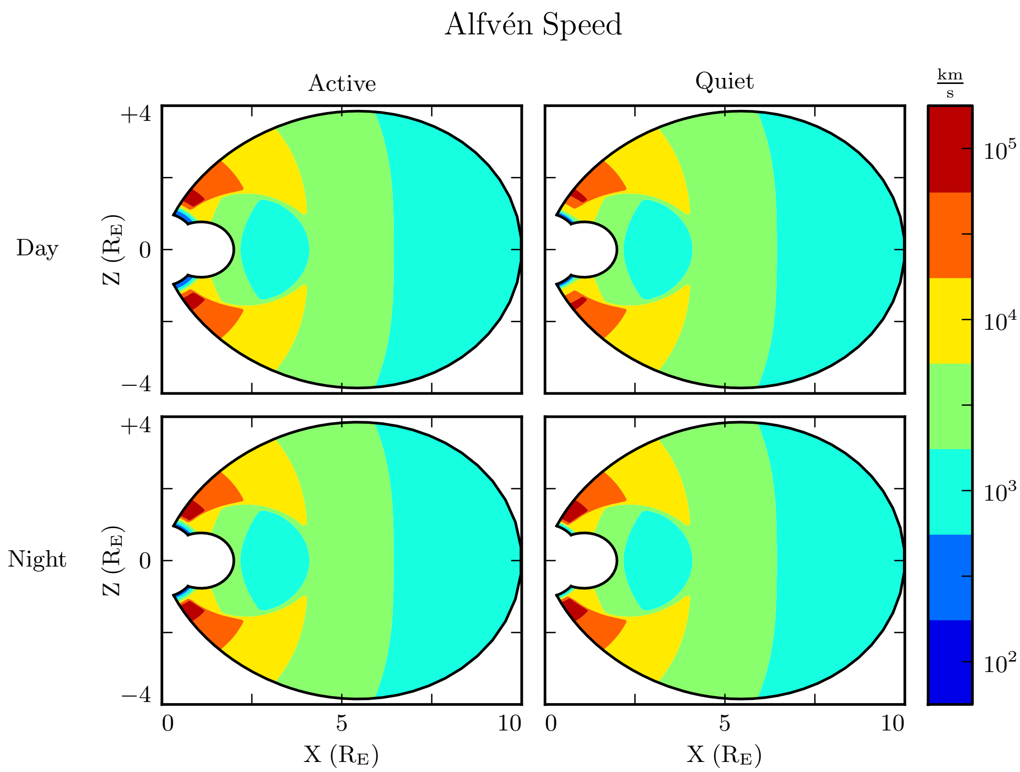

Figure 5.2: Alfvén speed profiles are based on low-density values tabulated by Kelley[49]. They are adjusted to take into account the density of the plasmapause and mass loading near the Earthward boundary.

perpendicular electric constant ϵ_K, corresponding to the differing ionospheric conditions between the dayside and the nightside, and between the high and low points in the solar cycle. These differences are visible in Figure 5.2, particularly in the size of the ionospheric Alfvén resonator (the peak in Alfvén speed in the high-latitude ionosphere).

TODO: Runs are only carried out for day and night... is it even worth showing the flank profile?

Ionospheric conductivity profiles are also based on values tabulated by Kelley, adjusted by Lysak[63] to take into account the abundance of heavy ions near the Earthward boundary. Pedersen, Hall, and parallel conductivities are each resolved by altitude, as shown in Figure 5.3.

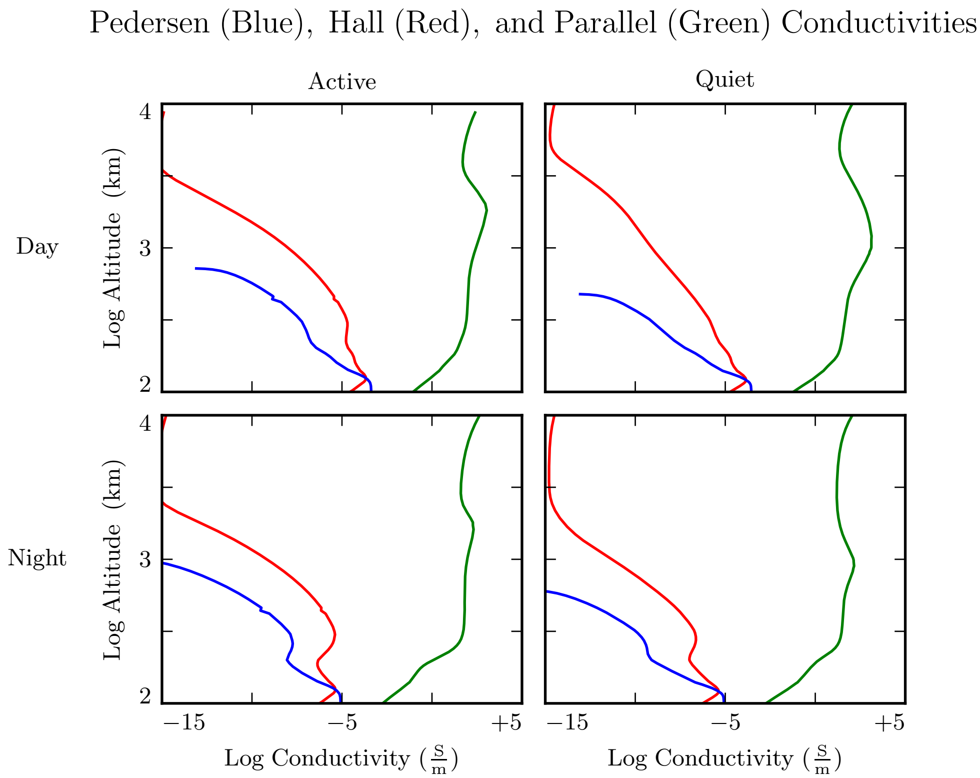

Figure 5.3: Ionospheric conductivity profiles are adapted by Lysak[63] from Kelley's tabulated values[49]. These profiles allow Tuna to simulate magnetosphere-ionosphere coupling under a variety of conditions.

Tuna's physical parameter profiles are static over the course of each run. Even so-called ultra low frequency waves like Pc4 pulsations are fast compared to convective timescales in the magnetosphere.

5.3 Driving

Models similar to Tuna have traditionally been driven using compression at the outer boundary[59, 63, 102, 103]. Such driving acts as a proxy for solar wind compression, Kelvin-Helmholtz effects at the magnetopause, and so on. However, because of the constraints imposed by the dispersion relation for Alfvén waves[8], simulations driven from the outer boundary are constrained to the consideration of waves with low azimuthal modenumber (equivalently, large azimuthal wavelength).

This issue is demonstrated in Figure 5.4. At low modenumber, energy delivered at the outer boundary propagates across field lines in order to stimulate resonances in the inner magnetosphere. However, as modenumber increases, Alfvén waves become increasingly guided, and the inner magnetosphere is unaffected by perturbations at the outer boundary.

In order to simulate high-modenumber Alfvén waves in the inner magnetosphere — such as giant pulsations — a new driving mechanism is necessary. Perturbation of the ring current is a natural choice, as Alfvén waves in the Pc4 range are known to interact with ring current particles through drift and drift-bounce resonances. The ring current is a dynamic region, particularly during and after geomagnetic storms; it's easy to imagine the formation of localized inhomogeneities.

In order to estimate an appropriate magnitude for perturbations of the ring current, the Sym-H storm index is used. The index is measured once per minute, and so cannot directly detect ring current modulations in the Pc4 frequency range. Instead, the index is transformed into the frequency domain, allowing a fit of its pink noise[9].

TODO: Sym-H is basically the same as DST [101].

As shown in Figure 5.5, a Fourier transform of the Sym-H index (taken here from the June 2013 storm) suggests that magnetic field perturbations at Earth's surface due to ring current activity in the Pc4 frequency range could be up to the order of $10^{-2}\,\mathrm{nT}$. Supposing that the ring current is centered around $5\,\mathrm{R_E}$ geocentric, that corresponds to a current on the order of $0.1\,\mathrm{MA}$. Tuna's driving is spread using a Gaussian profile in u^1 (typically centered at $L = 5$) and u^3 (typically centered just off the equator), with a characteristic area of $1\,\mathrm{R_E}^2$; this gives a current density on the order of $10^{-4}\,\mathrm{\mu A/m^2}$.

[8] See Section 4.4.

[9] Pink noise, also called $\frac{1}{f}$ noise, refers to the power law decay present in the Fourier transforms of all manner of physical signals.

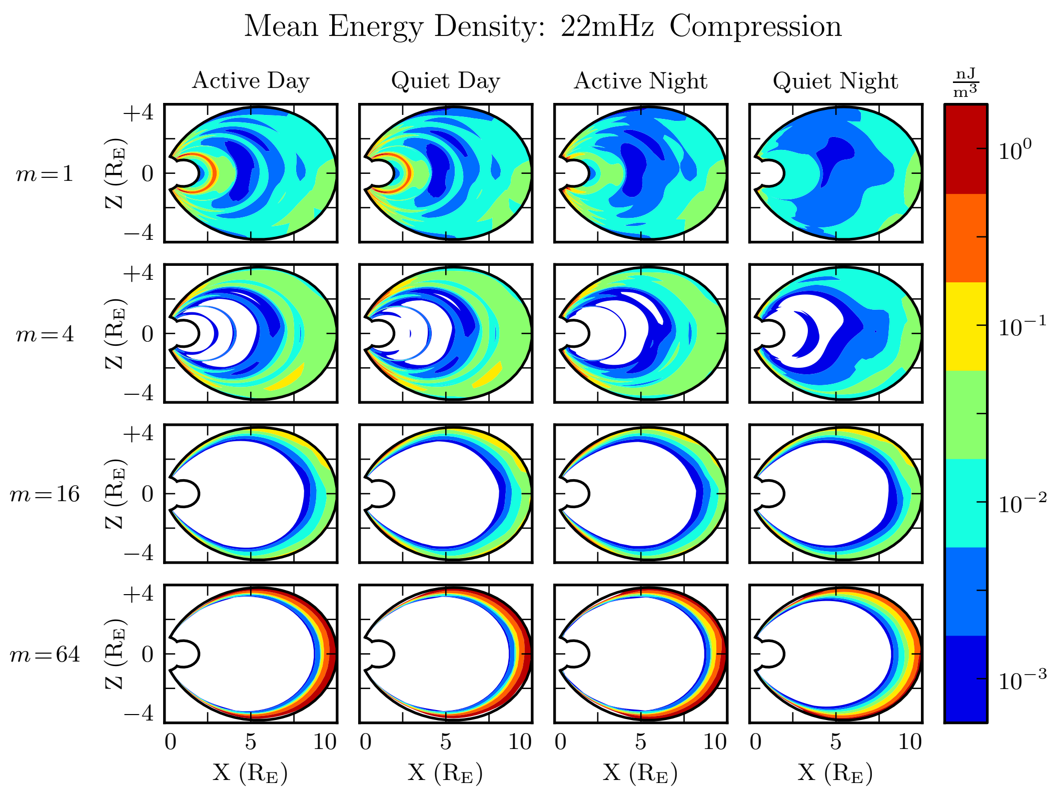

Figure 5.4: Each cell presents the mean energy density over the course of a 300 s run, as a function of position, due to compressional driving at the outer boundary. Azimuthal modenumber varies by row, and ionospheric conditions vary by column. For runs with small azimuthal modenumber, it's clear that energy is able to propagate across field lines and stimulate wave activity in the inner magnetosphere. When the modenumber is large, energy is unable to penetrate to the inner magnetosphere. Notably, the large values on the bottom row should be taken with a grain of salt; it's not clear that the model's results are reliable when waves are continuously forced against the boundary.

TODO: Admittedly, estimating the strength of localized perturbations using Sym-H — an index averaged over the entire globe — is a bit of a kludge.

In situ observations of Pc4 pulsations and giant pulsations have shown waves with modenumbers across the range $1 \lesssim m \lesssim 100$[18, 19, 92]. Simulations are carried out across that range, corresponding to ring current perturbations with azimuthal extent as small as $0.5\,\mathrm{R_E}$.

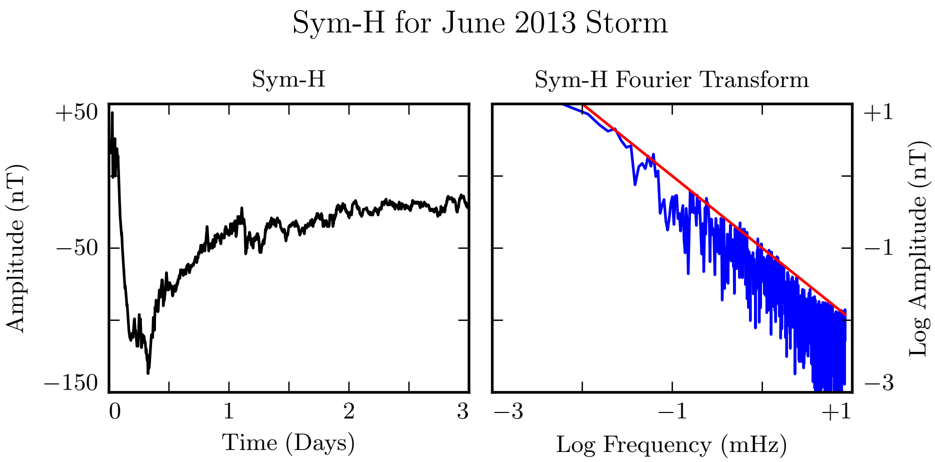

Figure 5.5: The Sym-H storm index[73] measures magnetic perturbations on Earth's surface due to ring current activity. The amplitude of oscillations in the Pc4 range is estimated by fitting the pink noise in its Fourier transform.

TODO: Driving is delivered in the azimuthal component of the current only.

TODO: Driving is sinusoidal.

TODO: In case it's not clear: Chapter 7 discusses ONLY simulations using ring current driving. The only compressional driving we look at is Figure 5.4.

TODO: Driving on the dayside is centered at $L = 5$. On the nightside, due to the increased Alfvén speed, it's moved out to $L = 6$. The Alfvén bounce time at $L = 5$ on the nightside is well above the Pc4 range.

TODO: ACTUALLY we should show the runs driven at $L \sim 5$ across the board. Dayside and nightside. That way we can make a fair comparison.

5.4 Maxwell's Equations

Tuna simulates the evolution of electromagnetic waves in accordance with Ampère's law and Faraday's law. Computation is carried out on a Yee grid[107]: electric fields and magnetic fields are offset by half a time step, and each field component is defined on either odd or even grid points in each dimension to ensure that curls are computed using centered differences.

The Ohmic current in Ampère's law is replaced with $\underline{\underline{\sigma}} \cdot \underline{E}$ per Kirchhoff's formulation of Ohm's law. Then, taking $\underline{J}$ to represent the driving current discussed in Section 5.3, Maxwell's equations can be written

$$\frac{\partial}{\partial t}\underline{B} = -\nabla \times \underline{E} \qquad\qquad \underline{\underline{\epsilon}} \cdot \frac{\partial}{\partial t}\underline{E} = \frac{1}{\mu_0}\nabla \times \underline{B} - \underline{J} - \underline{\underline{\sigma}} \cdot \underline{E} \tag{5.12}$$

It is convenient to introduce shorthand for the curl of each field: $\underline{C} \equiv \nabla \times \underline{E}$ and $\underline{F} \equiv \nabla \times \underline{B} - \mu_0 \underline{J}$. Or, recalling Equation (5.6),

$$C^i = \frac{\varepsilon^{ijk}}{\sqrt{g}} \frac{\partial}{\partial u^j} E_k \qquad\qquad F^i = \frac{\varepsilon^{ijk}}{\sqrt{g}} \frac{\partial}{\partial u^j} B_k - J^i \tag{5.13}$$

In these terms, Faraday's law can simply be written:

$$\frac{\partial}{\partial t} B^i = -C^i \tag{5.14}$$

Writing each component out explicitly, and using the metric tensor (per Equation (5.5)) to eliminate contravariant magnetic field components[10], Equation (5.14) becomes:

$$\begin{aligned} B_1 &\leftarrow B_1 - g_{11}\, \delta t\, C^1 - g_{13}\, \delta t\, C^3 \\ B_2 &\leftarrow B_2 - g_{22}\, \delta t\, C^2 \\ B_3 &\leftarrow B_3 - g_{31}\, \delta t\, C^1 - g_{33}\, \delta t\, C^3 \end{aligned} \tag{5.15}$$

Note that the $\leftarrow$ operator is used in Equation (5.15) to indicate assignment, rather than equality. Terms on the left are new, while those on the right are old.

[10] Fields are stored only in terms of their covariant components, and curls in terms of their contravariant components. This reduces Tuna's memory footprint (since each field need not be stored twice) as well as its computational cost (since time need not be spent rotating between bases). As a result, Tuna's solutions to Maxwell's equations are linear expressions whose coefficients are a mishmash of physical constants and geometric factors. To save time, each coefficient is computed once and stored, rather than being multiplied out from scratch with each time step.

Unlike Faraday's law, Ampère's law cannot be trivially solved. Not only does the derivative of $\underline{E}$ depend on its own future value, but the crosswise and azimuthal components of the equation are coupled by the Hall terms in the conductivity tensor. Fortunately, the electric tensor can be inverted, allowing a solution by integrating factors:

$$\underline{\underline{\epsilon}} \cdot \frac{\partial}{\partial t}\underline{E} = \frac{1}{\mu_0}\underline{F} - \underline{\underline{\sigma}} \cdot \underline{E} \qquad \text{becomes} \qquad \left(\underline{\underline{\Omega}} + \underline{\underline{\mathbb{I}}}\frac{\partial}{\partial t}\right) \cdot \underline{E} = \underline{\underline{V}}^2 \cdot \underline{F} \tag{5.16}$$

Where $\underline{\underline{\mathbb{I}}}$ is the identity tensor and in x-y-z coordinates[11],

$$\underline{\underline{V}}^2 \equiv \frac{1}{\mu_0}\underline{\underline{\epsilon}}^{-1} = \begin{bmatrix} v_A^2 & 0 & 0 \\ 0 & v_A^2 & 0 \\ 0 & 0 & c^2 \end{bmatrix} \quad \text{and} \quad \underline{\underline{\Omega}} \equiv \underline{\underline{\epsilon}}^{-1} \cdot \underline{\underline{\sigma}} = \begin{bmatrix} \frac{\sigma_P}{\epsilon_\perp} & \frac{-\sigma_H}{\epsilon_\perp} & 0 \\ \frac{\sigma_H}{\epsilon_\perp} & \frac{\sigma_P}{\epsilon_\perp} & 0 \\ 0 & 0 & \frac{\sigma_0}{\epsilon_0} \end{bmatrix} \tag{5.17}$$

Multiplying through by $\exp\left(\underline{\underline{\Omega}}\, t\right)$ and applying the product rule, Equation (5.16) becomes[12]

$$\frac{\partial}{\partial t}\left(\exp\left(\underline{\underline{\Omega}}\, t\right) \cdot \underline{E}\right) = \exp\left(\underline{\underline{\Omega}}\, t\right) \cdot \underline{\underline{V}}^2 \cdot \underline{F} \tag{5.18}$$

Equation (5.18) can then be integrated over a small time step δt and expressed in terms of the assignment operator introduced in Equation (5.15).

$$\underline{E} \leftarrow \exp\left(-\underline{\underline{\Omega}}\, \delta t\right) \cdot \underline{E} + \delta t \, \exp\left(-\underline{\underline{\Omega}}\, \tfrac{\delta t}{2}\right) \cdot \underline{\underline{V}}^2 \cdot \underline{F} \tag{5.19}$$

The tensor exponential can be evaluated by splitting $\underline{\underline{\Omega}}$ into the sum of its diagonal and Hall components [13]. The Hall exponential condenses into sines and cosines, giving a rotation around the magnetic field line:

$$\underline{E} \leftarrow \exp\left(-\underline{\underline{\Omega}}'\, \delta t\right) \cdot \underline{\underline{R}}_z\left(\tfrac{-\sigma_H \delta t}{\epsilon_\perp}\right) \cdot \underline{E} + \delta t \, \underline{\underline{V}}^2 \cdot \exp\left(-\underline{\underline{\Omega}}'\, \tfrac{\delta t}{2}\right) \cdot \underline{\underline{R}}_z\left(\tfrac{-\sigma_H \delta t}{2\epsilon_\perp}\right) \cdot \underline{F} \tag{5.20}$$

[11] Note the parallel component of the present definition of $\underline{\underline{\Omega}}$ differs slightly from that used in Chapter 4, due to the present neglect of inertial effects; see Chapter 6.

[12] Tensor exponentiation is analogous to scalar exponentiation[38]: $\exp\left(\underline{\underline{T}}\right) \equiv \sum_n \frac{1}{n!}\underline{\underline{T}}^n$.

[13] For tensors, $\exp\left(\underline{\underline{S}} + \underline{\underline{T}}\right) = \exp\left(\underline{\underline{S}}\right)\exp\left(\underline{\underline{T}}\right)$ as long as $\underline{\underline{S}} \cdot \underline{\underline{T}} = \underline{\underline{T}} \cdot \underline{\underline{S}}$.

Where

$$\underline{\underline{R}}_z(\theta) = \begin{bmatrix} \cos\theta & -\sin\theta & 0 \\ \sin\theta & \cos\theta & 0 \\ 0 & 0 & 1 \end{bmatrix} \qquad \text{and} \qquad \underline{\underline{\Omega}}' \equiv \begin{bmatrix} \frac{\sigma_P}{\epsilon_\perp} & 0 & 0 \\ 0 & \frac{\sigma_P}{\epsilon_\perp} & 0 \\ 0 & 0 & \frac{\sigma_0}{\epsilon_0} \end{bmatrix} \tag{5.21}$$

The parallel component of term of Equation (5.20) is simply

$$E_z \leftarrow E_z \exp\left(\tfrac{-\sigma_0 \delta t}{\epsilon_0}\right) + c^2 \delta t F_z \exp\left(\tfrac{-\sigma_0 \delta t}{2\epsilon_0}\right) \tag{5.22}$$

Or, using Equation (5.7) to map to the covariant basis,

$$E_3 \leftarrow E_3 \exp\left(\tfrac{-\sigma_0 \delta t}{\epsilon_0}\right) + c^2 \delta t \left(g_{31} F^1 + g_{33} F^3\right) \exp\left(\tfrac{-\sigma_0 \delta t}{2\epsilon_0}\right) \tag{5.23}$$

Tuna's conductivity profile gives a minimum value of $\frac{\sigma_0 \delta t}{\epsilon_0}$ on the order of 10^3, making $\exp\left(\frac{-\sigma_0 \delta t}{\epsilon_0}\right)$ far too small to be stored in a double precision variable[14]. That is, this model takes E_3 (and, proportionally, E_z) to be uniformly zero. This issue is revisited in Chapter 6.

The perpendicular components of Equation (5.20) give the expressions:

$$\begin{aligned} E_1 + \frac{g^{13}}{g^{11}} E_3 \leftarrow \quad & E_1 \cos\left(\tfrac{-\sigma_H \delta t}{\epsilon_\perp}\right) \exp\left(\tfrac{-\sigma_P \delta t}{\epsilon_\perp}\right) \\ & + E_2 \sin\left(\tfrac{-\sigma_H \delta t}{\epsilon_\perp}\right) \exp\left(\tfrac{-\sigma_P \delta t}{\epsilon_\perp}\right) \sqrt{\frac{g^{22}}{g^{11}}} \\ & + E_3 \cos\left(\tfrac{-\sigma_H \delta t}{\epsilon_\perp}\right) \exp\left(\tfrac{-\sigma_P \delta t}{\epsilon_\perp}\right) \frac{g^{13}}{g^{11}} \\ & + F^1 \cos\left(\tfrac{-\sigma_H \delta t}{2\epsilon_\perp}\right) \exp\left(\tfrac{-\sigma_P \delta t}{2\epsilon_\perp}\right) \frac{v_A^2 \delta t}{g^{11}} \\ & + F^2 \sin\left(\tfrac{-\sigma_H \delta t}{2\epsilon_\perp}\right) \exp\left(\tfrac{-\sigma_P \delta t}{2\epsilon_\perp}\right) \frac{v_A^2 \delta t}{\sqrt{g^{11} g^{22}}} \end{aligned} \tag{5.24}$$

[14] Not coincidentally, $\frac{\sigma_0}{\epsilon_0}$ can also be written $\frac{\omega_P^2}{\nu}$. At the ionosphere, the collision frequency ν is fast compared to field line resonance timescales, but it's still slow compared to the plasma frequency.

and

$$
\begin{aligned}
E_2 \longleftarrow & -E_1 \sin\left(\tfrac{-\sigma_H \delta t}{\epsilon_\perp}\right) \exp\left(\tfrac{-\sigma_P \delta t}{\epsilon_\perp}\right) \sqrt{\frac{g^{11}}{g^{22}}} \\
& + E_2 \cos\left(\tfrac{-\sigma_H \delta t}{\epsilon_\perp}\right) \exp\left(\tfrac{-\sigma_P \delta t}{\epsilon_\perp}\right) \\
& - E_3 \sin\left(\tfrac{-\sigma_H \delta t}{\epsilon_\perp}\right) \exp\left(\tfrac{-\sigma_P \delta t}{\epsilon_\perp}\right) \frac{g^{13}}{\sqrt{g^{11} g^{22}}} \\
& - F^1 \sin\left(\tfrac{-\sigma_H \delta t}{2\epsilon_\perp}\right) \exp\left(\tfrac{-\sigma_P \delta t}{2\epsilon_\perp}\right) \frac{v_A^2 \delta t}{\sqrt{g^{11} g^{22}}} \\
& + F^2 \cos\left(\tfrac{-\sigma_H \delta t}{2\epsilon_\perp}\right) \exp\left(\tfrac{-\sigma_P \delta t}{2\epsilon_\perp}\right) \frac{v_A^2 \delta t}{g^{22}}
\end{aligned}
\tag{5.25}
$$

The E_3 terms in Equations (5.24) and (5.25) can be ignored at present. They are revisited in Chapter 6.

It bears recalling that the driving current is defined as part of $\underline{F}$, per Equation (5.13). When the driving current is purely azimuthal ($J^1 = J^3 = 0$), the driving is in principle applied to both the poloidal and the toroidal electric fields through F^2. However, in practice, the driving applied to the toroidal electric field is vanishingly small. The driving current J^2 is localized around $5\,\mathrm{R_E}$ geocentric, and $\exp\left(\tfrac{-\sigma_P \delta t}{2\epsilon_\perp}\right)$ drops off quickly with altitude.

5.5 Boundary Conditions

Dirichlet and Neumann boundary conditions are applied to the electric field components and magnetic field components respectively. That is, electric fields are forced to go to zero at the inner and outer boundaries, and magnetic fields are forced to have a zero derivative normal to the inner and outer boundaries.

These boundary conditions can in principle cause nonphysical reflections at the boundary[15]. However, in practice, wave activity is concentrated well within the simulation domain. Simulation results are robust under an exchange of Dirichlet and Neumann

[15] See, for example, the bottom row of Figure 5.4.

boundary conditions (though a self-inconsistent set of boundary condidtions, such as applying Neumann boundary conditions to B_1 but Dirichlet boundary conditions to B_3, quickly causes instability).

The Earthward boundary conditions are as follows.

Between the top of the neutral atmosphere and the bottom of the ionosphere, the model includes a thin, horizontal current sheet representing the ionosphere's E layer[59]. By integrating Ampère's law over the layer, it can be shown[29] that the horizontal electric field values at the edge of the grid are determined by the jump in the horizontal magnetic fields:

$$\underline{\underline{\Sigma}} \cdot \underline{E} = \frac{1}{\mu_0} \lim_{\delta r \to 0} \left[\hat{r} \times \underline{B} \right|_{R_I - \delta r}^{R_I + \delta r} \tag{5.26}$$

The integrated conductivity tensor $\underline{\underline{\Sigma}}$ can be written in θ-ϕ coordinates as[59]:

$$\underline{\underline{\Sigma}} \equiv \begin{bmatrix} \frac{\Sigma_0 \Sigma_P}{\Sigma_0 \cos^2\alpha + \Sigma_P \sin^2\alpha} & \frac{-\Sigma_0 \Sigma_H}{\Sigma_0 \cos^2\alpha + \Sigma_P \sin^2\alpha} \\ \frac{\Sigma_0 \Sigma_H}{\Sigma_0 \cos^2\alpha + \Sigma_P \sin^2\alpha} & \Sigma_P + \frac{\Sigma_H^2 \sin^2\alpha}{\Sigma_0 \cos^2\alpha + \Sigma_P \sin^2\alpha} \end{bmatrix} \tag{5.27}$$

Where α is the angle between the magnetic field and the vertical direction, given by $\cos\alpha \equiv \frac{-2\cos\theta}{\sqrt{1+3\cos^2\theta}}$, and Σ_P, Σ_H, and Σ_0 are the height-integrated Pedersen, Hall, and parallel conductivities respectively. Their values are determined by integrating Kelley's[49] conductivity profiles from Earth's surface to the ionospheric boundary; values are shown in Table 5.2.

Table 5.2: Integrated Atmospheric Conductivity (S)

	Σ_0	Σ_P	Σ_H
Active Day	424	0.65	6.03
Quiet Day	284	0.44	4.02
Active Night	9	0.01	0.12
Quiet Night	9	0.01	0.12

An expression for the horizontal electric fields at the boundary can be obtained by inverting Equation (5.26). After mapping to covariant coordinates per Equation (5.8), and taking $\Sigma \equiv \det \underline{\underline{\Sigma}}$,

$$\begin{aligned} E_1 &\leftarrow \frac{1}{\mu_0 \Sigma} \lim_{\delta r \to 0} \left[\qquad -\Sigma_{\theta\phi} B_1 - \sqrt{\frac{g_{11}}{g_{22}}} \Sigma_{\phi\phi} B_2 \right|_{R_I - \delta r}^{R_I + \delta r} \\ E_2 &\leftarrow \frac{1}{\mu_0 \Sigma} \lim_{\delta r \to 0} \left[\sqrt{\frac{g_{22}}{g_{11}}} \Sigma_{\theta\theta} B_1 + \qquad \Sigma_{\phi\theta} B_2 \right|_{R_I - \delta r}^{R_I + \delta r} \end{aligned} \tag{5.28}$$

In order to compute the atmospheric magnetic field, a scalar magnetic potential (Ψ such that $\underline{B} = \nabla \Psi$) is computed as a linear combination of harmonics. The neutral atmosphere is considered to be a perfect insulator, giving $\nabla \times \underline{B} = 0$. Combined with $\nabla \cdot \underline{B} = 0$ (per Maxwell's equations), Ψ satisfies Laplace's equation, $\nabla^2 \Psi = 0$.

Laplace's equation can be solved analytically; however, a numerical solution is preferrable to ensure orthonormality on a discrete and incomplete[16] grid. After separating out the radial and azimuthal dependence in the usual way, the latitudinal component of Laplace's equation can be written in terms of $s \equiv -\sin^2 \theta$:

$$\left(4s^2 + 4s\right) \frac{d^2}{ds^2} Y_\ell + (4 + 6s) \frac{d}{ds} Y_\ell - \frac{m^2}{s} Y_\ell = \ell \, (\ell + 1) \, Y_\ell \tag{5.29}$$

Using centered differences to linearize the derivatives, Equation (5.29) becomes a system of coupled linear equations, one per field line. It can be solved numerically for eigenvalues $\ell \, (\ell + 1)$ and eigenfunctions Y_ℓ[17]. In terms of the harmonics Y_ℓ, Ψ between the Earth's surface and the top of the atmosphere can be written using eigenweights a_ℓ and b_ℓ:

$$\Psi = \sum_\ell \left(a_\ell \, r^\ell + b_\ell \, r^{-\ell - 1} \right) Y_\ell \tag{5.30}$$

[16] As discussed in Section 5.1, the grid is constrained to finite L, which excludes the equator as well as the poles.

[17] Solving Laplace's equation analytically results in spherical harmonics indexed by both ℓ and m, the separation constants for θ and ϕ respectively. In two and a half dimensions, ϕ is not explicitly resolved, so m is set manually.

As a boundary condition for Ψ, Earth is assumed to be a perfect conductor. This forces the magnetic field at Earth's surface to be horizontal; that is, $B_r = \frac{\partial}{\partial r}\Psi = 0$. Noting that solutions to Laplace's equation are orthonormal, each element of the sum in Equation (5.30) must be independently zero at R_E. This allows the coefficients a_ℓ and b_ℓ to be expressed in terms of one another.

$$b_\ell = \frac{\ell}{\ell + 1} R_E^{2\ell+1} a_\ell \tag{5.31}$$

The current sheet at the top of the atmosphere is assumed to be horizontal, so the radial component of the magnetic field must be the same just above and just below it. Taking the radial derivative of Equation (5.30) at the top of the atmosphere, and eliminating b_ℓ with Equation (5.31), gives

$$B_r = \sum_\ell \ell \, a_\ell \, R_I^{\ell-1} \left(1 - \lambda^{2\ell+1}\right) Y_\ell \qquad \text{where} \qquad \lambda \equiv \frac{R_E}{R_I} \sim 0.975 \tag{5.32}$$

The summation can be collapsed by "integrating" over a harmonic[18]. Inverse harmonics can be obtained by inverting the eigenvector matrix. Then $Y_\ell \cdot Y_{\ell'}^{-1} = \delta_{\ell\ell'}$ by construction.

$$a_\ell = \frac{1}{\ell \, R_I^{\ell-1}} \frac{B_r \cdot Y_\ell^{-1}}{1 - \lambda^{2\ell+1}} \tag{5.33}$$

Combining Equations (5.30), (5.31), and (5.33) allows the expression of Ψ at the top and bottom of the atmosphere as a linear combination of radial magnetic field components at the bottom of the ionosphere.

$$\begin{aligned}
\Psi_E &= \sum_\ell Y_\ell \, \frac{R_I}{\ell \, (\ell - 1)} \frac{(2\ell - 1) \, \lambda^\ell}{1 - \lambda^{2\ell+1}} B_r \cdot Y_\ell^{-1} \\
\Psi_I &= \sum_\ell Y_\ell \, \frac{R_I}{\ell \, (\ell - 1)} \frac{(\ell - 1) + \ell \, \lambda^{2\ell+1}}{1 - \lambda^{2\ell+1}} B_r \cdot Y_\ell^{-1}
\end{aligned} \tag{5.34}$$

[18] Because the functions are defined on a discrete grid, their inner product is not an integral, but a sum: $B_r \cdot Y_\ell^{-1} \equiv \sum_i B_r[i] \, Y_\ell^{-1}[i]$.

Horizontal magnetic fields are obtained by taking derivatives of Ψ.

$$B_1 = \frac{\partial}{\partial u^1}\Psi \qquad\qquad B_2 = \frac{\partial}{\partial u^2}\Psi \tag{5.35}$$

Horizontal magnetic field values at the top of the atmosphere are used to impose boundary conditions on the electric fields at the bottom of the ionosphere, per Equation (5.28). Those at Earth's surface are valuable because they allow a direct comparison between model output and ground magnetometer data, after being mapped to physical coordinates per Equation (5.8).

Chapter 6

Electron Inertial Effects

As laid out in Chapter 5, Tuna resolves neither parallel currents nor parallel electric fields. This is unfortunate; parallel electric fields generated by kinetic and inertial Alfvén waves (including fundamental field line resonances[81, 97]) are a topic of particular interest in the study of auroral particle precipitation.

Parallel currents and electric fields can be added to Tuna through the consideration of electron inertial effects in Ohm's law:

$$0 = \sigma_0 E_z - J_z \qquad \text{becomes} \qquad \frac{1}{\nu}\frac{\partial}{\partial t} J_z = \sigma_0 E_z - J_z \tag{6.1}$$

With the addition of the electron inertial term, it is necessary to track the parallel current independent of the parallel electric field[1]. Solving by integrating factors[2] gives

$$J_3 \leftarrow J_3 \, \exp(-\nu \delta t) + \delta t \, \frac{ne^2}{m_e} E_3 \, \exp\!\left(-\nu \tfrac{\delta t}{2}\right) \tag{6.2}$$

[1] The parallel current J_z is defined on the same points of the Yee grid as E_z. It is offset in time by half of a time step.

[2] The integrating factors technique is laid out explicitly for Ampère's law in Section 5.4.

From there, the parallel electric field can be updated directly; Equation (5.23) is replaced by the following:

$$E_3 \leftarrow E_3 + c^2 \delta t \, \left(g_{31} F^1 + g_{33} F^3 \right) - \frac{\delta t}{\epsilon_0} J_3 \tag{6.3}$$

The present section explores the complications that arise from the addition of the electron inertial term to Ohm's law, as well as a few results that may be gleaned despite those complications. Notably — for reasons discussed in Section 6.3 — the results presented in Chapter 7 do not make use of the electron inertial term.

Inertial effects have been considered in previous numerical work, such as by Lysak and Song in 2001[61], but never at the global scale. Lysak and Song considered waves in the ionospheric Alfvén resonator, with frequencies of hundreds of mHz. Their work did not account for the effects of the dipolar geometry, such as differenced that might arise between poloidal and toroidal resonances. In fact, in that work, circular polarization (essentially a superposition of poloidal and toroidal modes) was noted to be a promising avenue for future work.

6.1 The Boris Factor

With the addition of the electron inertial term, a cyclical dependence appears between Ampère's law and Ohm's law:

$$\frac{\partial}{\partial t} E_z \sim -\frac{1}{\epsilon_0} J_z \qquad \text{and} \qquad \frac{\partial}{\partial t} J_z \sim \frac{ne^2}{m_e} E_z \qquad \text{so} \qquad \frac{\partial^2}{\partial t^2} E_z \sim -\omega_P^2 E_z \tag{6.4}$$

That is, electron inertial effects come hand in hand with the plasma oscillation.

As mentioned in Chapter 4 and shown in Figure 6.1, plasma oscillation is quite fast — several orders of magnitude smaller than Tuna's time step as determined in Section 5.1 ($\sim$10 µs). This poses a conundrum. At Tuna's usual time step, the plasma oscillation becomes unstable within seconds[3]. On the other hand, reducing the time step by three

[3] For stability, $\omega_P \delta t < 1$ is necessary.

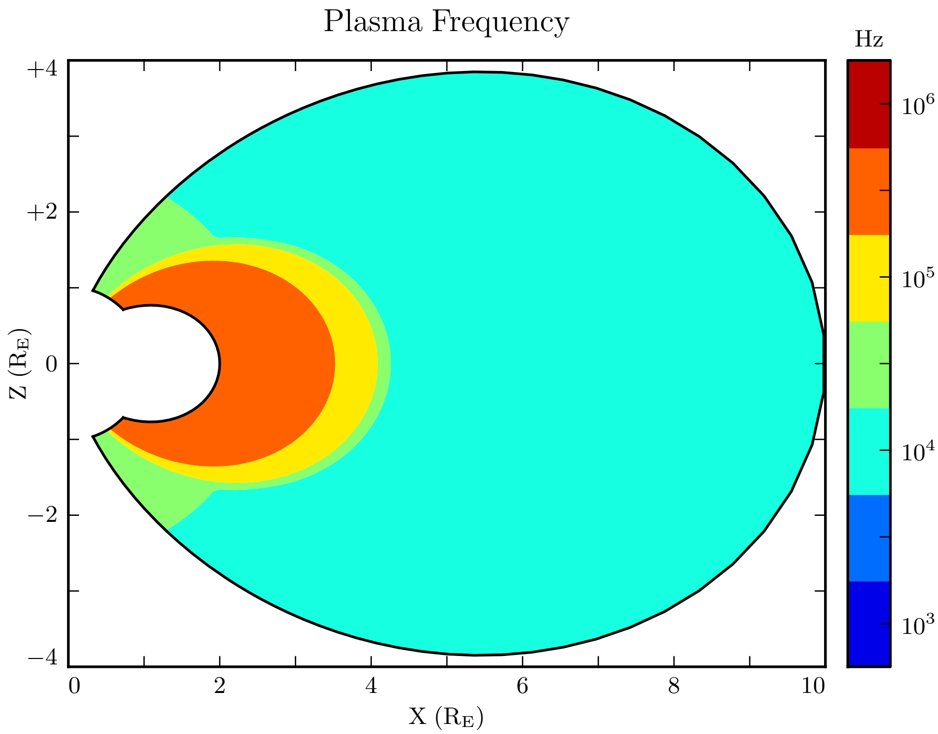

Figure 6.1: The plasma frequency reaches a peak value just under 10^6 Hz near the equator. Outside the plasmasphere, its value is closer to 10^4 Hz, which is still not well-resolved by Tuna's usual time step.

orders of magnitude to resolve the plasma oscillation is computationally infeasible; a run slated for an hour would require six weeks to complete.

As it happens, this problem can be solved by artificially increasing the parallel electric constant above its usual value of ϵ_0. Doing so lowers both the speed of light and the plasma frequency within the simulation.

This technique — and others like it — has been widespread in numerical modeling since it was presented by Boris in 1970[7]. More recently, Lysak and Song considered its use specifically for the case of electron inertial effects[61]. The following paraphrases their argument.

Supposing that the current and electric field are oscillating at frequency ω, the parallel components of Ampère's law and Ohm's law can be written

$$-i\omega\epsilon_0 E_z = \frac{1}{\mu_0}\left(\nabla\times\underline{B}\right)_z - J_z \qquad\qquad -\frac{i\omega}{\nu}J_z = \sigma_0 E_z - J_z \tag{6.5}$$

Then, eliminating the current, the parallel electric field can be related to the curl of the magnetic field by[4]

$$\left(1-\frac{\omega^2-i\nu\omega}{\omega_P^2}\right)E_z = \frac{c^2}{\omega_P^2}\left(\nu-i\omega\right)\left(\nabla\times\underline{B}\right)_z \tag{6.6}$$

In Equation (6.6), $\frac{c}{\omega_P}$ is the electron inertial length. While the speed of light and the plasma frequency each depend on ϵ_0, their ratio does not. This allows an estimation of how much the model should be affected by an artificially-large electric constant (and thus an artificially-small plasma frequency). So long as $\frac{\omega^2-i\nu\omega}{\omega_P^2}$ remains small compared to unity, the model should behave faithfully.

For waves with periods of a minute or so, even perhaps-implausibly large Boris factors are allowed; for example, increasing ϵ_0 by a factor of 10^6 gives $\left|\frac{\omega^2+i\omega\nu}{\omega_P^2}\right| \lesssim 0.01$.

6.2 Parallel Currents and Electric Fields

As discussed in Section 4.4, parallel electric fields in this regime are expected to be six or more orders of magnitude smaller than the perpendicular electric fields. Numerical results show general agreement: in Figure 6.2, the parallel electric field appears comparable to its perpendicular counterparts only after its been scaled up by six orders of magnitude.

As such, the inclusion of electron inertial effects does not appreciably impact the simulation's gross behavior; in Faraday's law, $\nabla\times\underline{E}$ is essentially unaffected. Side by side

[4]From Equation (4.4), $c^2 \equiv \frac{1}{\mu_0\epsilon_0}$ and $\sigma_0 \equiv \frac{ne^2}{m_e\nu}$ and $\omega_P^2 \equiv \frac{ne^2}{m_e\epsilon_0}$.

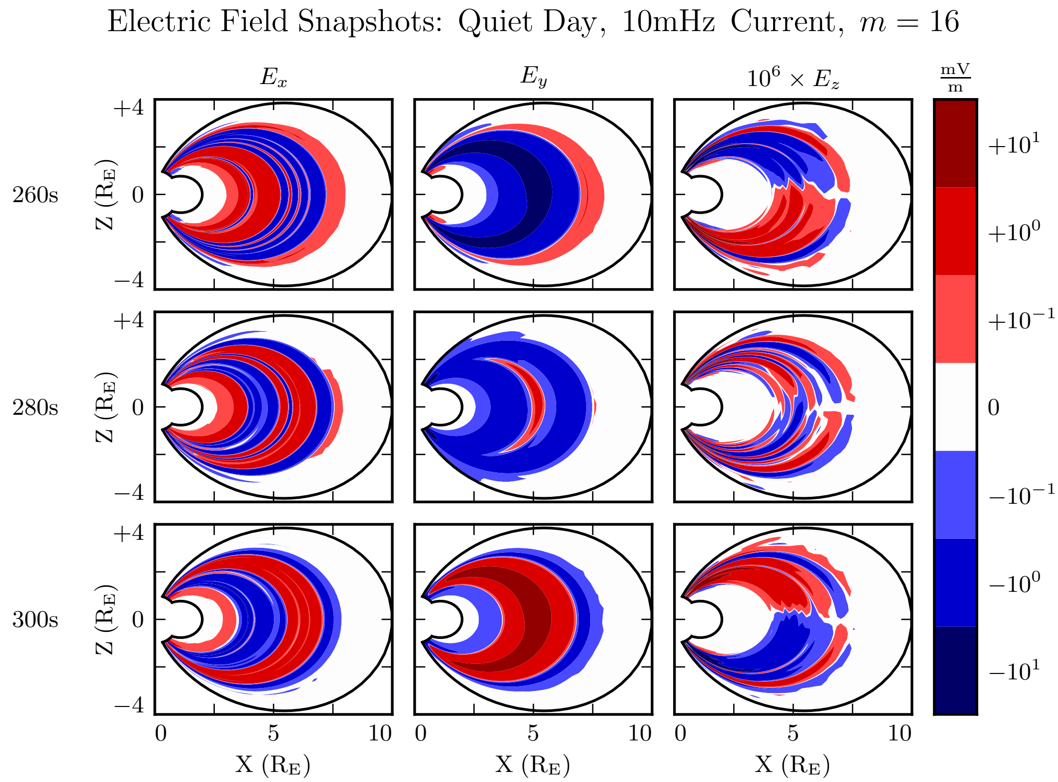

Figure 6.2: Parallel electric fields are smaller than perpendicular electric fields by about six orders of magnitude. As a result, parallel electric fields do not contribute significantly to $\nabla \times \underline{E}$ in Faraday's law.

snapshots of the magnetic fields in runs carried out with and without electron inertial effects are not visibly distinguishable[5] (not shown).

Even if there is no significant feedback through Faraday's law, it's informative to consider the structures that arise in parallel currents and electric fields driven by perturbations in the ring current. For example, in Figure 6.2, the parallel electric field perturbation (with maxima near the ionosphere) exhibits the opposite harmonic structure to the perpendicular electric field components (which peak near the equator).

[5]In a sense, this is reassuring. It ensures that the present section does not cast doubt on the results presented in Chapter 7, where electron inertial effects are neglected.

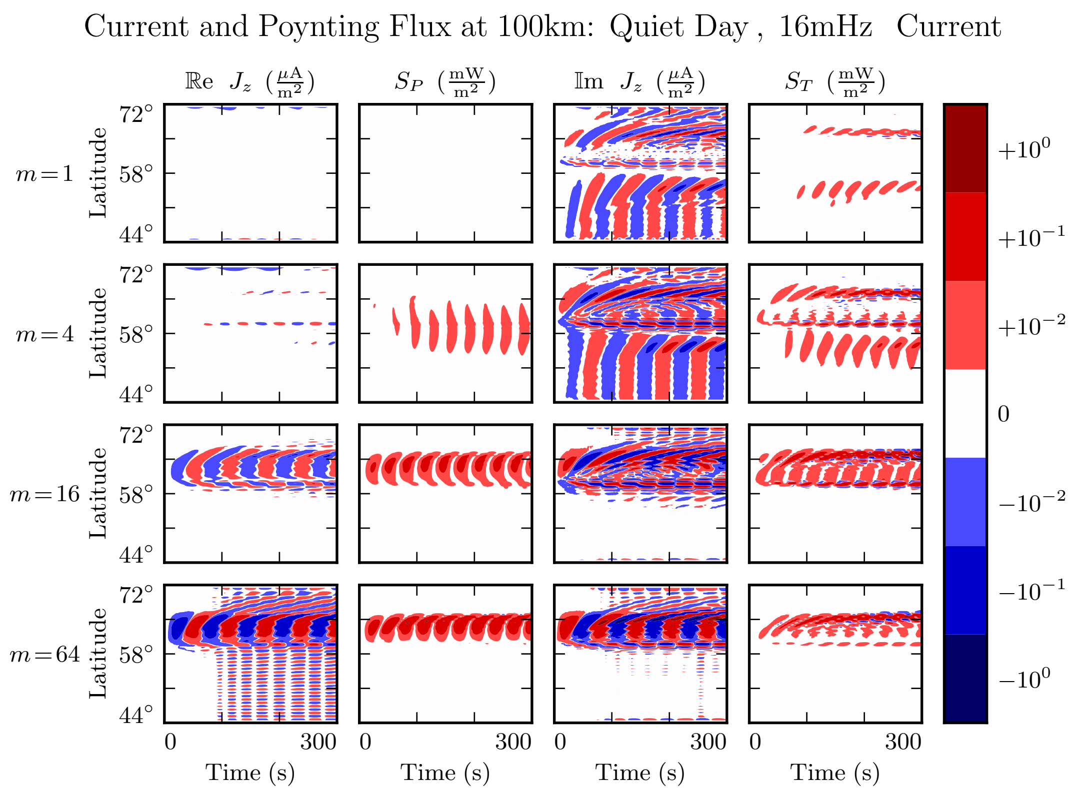

Figure 6.3: Four runs are shown above, one per row, with azimuthal modenumbers of 1, 4, 16, and 64. Columns show slices at 100 km of the real parallel current, poloidal Poynting flux, imaginary current, and toroidal Poynting flux respectively. The similarity visible across columns suggests that the real parallel current follows the poloidal Poynting flux, while the imaginary parallel current follows the toroidal Poynting flux (the toroidal fields are imaginary). At least, this is the case in regions of significant Hall conductivity.

At low altitude, the Hall conductivity muddles the poloidal and toroidal electric fields. In this region, as shown in Figure 6.3, parallel currents coincide with strong Poynting flux. The imaginary component of the current lines up with the toroidal Poynting flux (which comes from imaginary E_x and imaginary B_y^*), while the real current lines up with the poloidal Poynting flux (E_y and B_x^* are real)[6].

[6]As mentioned in Chapter 5, poloidal field components are in practice overwhelmingly real, indicating that they coincide azimuthally with the (real) driving. Toroidal components are overwhelmingly imaginary, which corresponds to an azimuthal offset.

Four runs are shown in Figure 6.3, one per row, with azimuthal modenumbers 1, 4, 16, and 64. The first and third columns show the real and imaginary components of the parallel current respectively, in units of $\mu A/m^2$, sliced at an altitude of 100 km, the edge of the simulation domain. The second and fourth columns are the poloidal and toroidal Poynting flux respectively, in units of mW/m^2. Latitude is shown on the vertical axis, and time on the horizontal axis.

At higher altitude, where the Hall conductivity is small, parallel current is associated only with the toroidal mode. Figure 6.4 shows data from the same runs as Figure 6.3, arranged in the same way, but the values are taken at an altitude of 1000 km instead of 100 km.

In Figure 6.4, as in Figure 6.3, the imaginary component of the parallel current (third column) coincides more or less with the toroidal Poynting flux (fourth column). However, the real component of the parallel current (first column) is vanishingly small, even when the poloidal Poynting flux (second column) is strong.

TODO: Is this expected? Tikhonchuk[97] looks specifically at the toroidal mode when considering shear Alfvén waves. Does the poloidal mode count as compressional even when it's guided? In his 2001 paper, Lysak[61] talks about how circularly-polarized waves might be interesting. That would be a superposition of the poloidal and toroidal modes, right? In that paper, he's looking at modes with frequencies of 1 Hz or so, in the context of the IAR. Lysak and Song's 2003 paper[62] looks at the toroidal mode, also in the IAR (?).

Notably, the Poynting flux waveforms are rectified — they primarily carry energy Earthward. The current, on the other hand, alternates between upward and downward flow. This effect presumably arises because the current is a linear quantity while the Poynting flux is quadratic: the electric and magnetic fields that make it up oscillate in phase, so their product is positive even when they are negative.

The magnitude of the parallel current tops out over $1\,\mu A/m^2$, just shy of the up-to-tens of $\mu A/m^2$ inferred from ground observations and seen in situ[9, 47, 84].

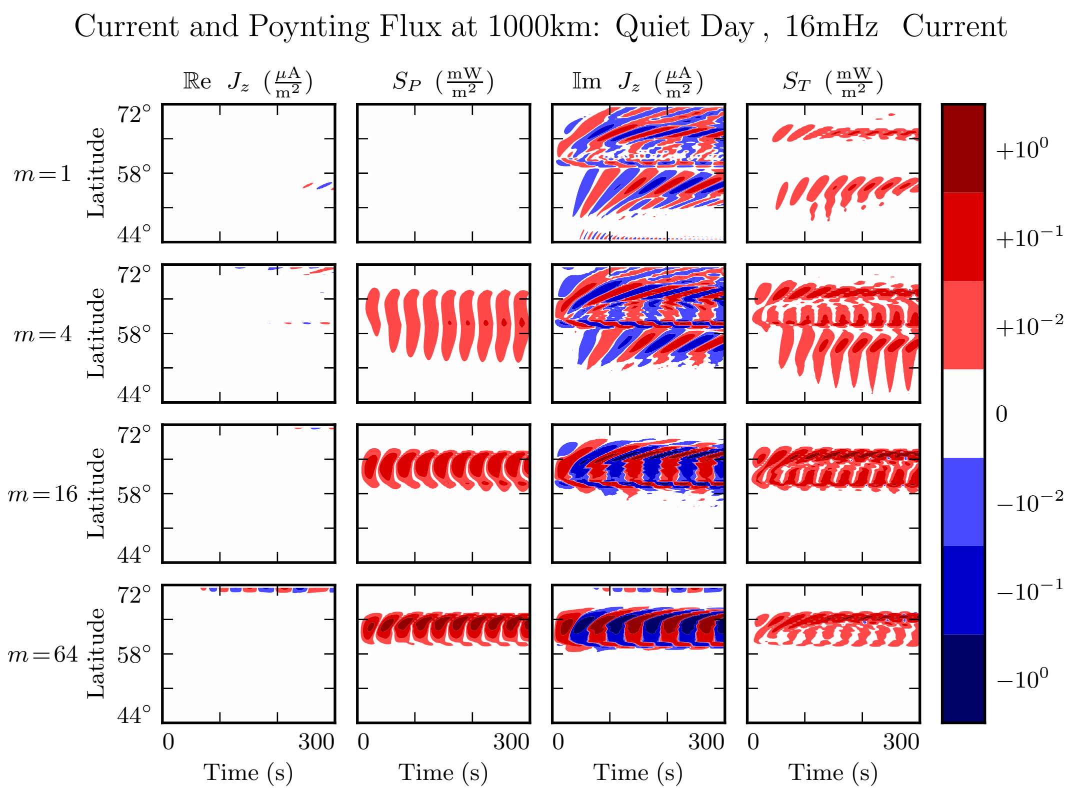

Figure 6.4: The above figure shows the same runs as Figure 6.3, except that the slices are taken at an altitude of 1000 km instead of 100 km. Morphological similarities are still evident between the imaginary parallel current and the toroidal Poynting flux. However, without the Hall conductivity to couple the modes, the poloidal mode does not appear to carry significant current along the field line.

It's also possible to consider the effect of parallel currents and electric fields on the ionosphere's energy budget, per Poynting's theorem:

$$\frac{\partial}{\partial t} u = -\nabla \cdot \underline{E} - \underline{J} \cdot \underline{E} \tag{6.7}$$

As shown in Figure 6.5, little energy transfer in the ionosphere is mediated by perpendicular components of the Poynting flux. The parallel component of $\underline{J} \cdot \underline{E}$ is comparably unimportant. The energy deposited in the ionosphre by the Poynting flux matches closely with the energy lost to Joule dissipation — as it should, to conserve energy

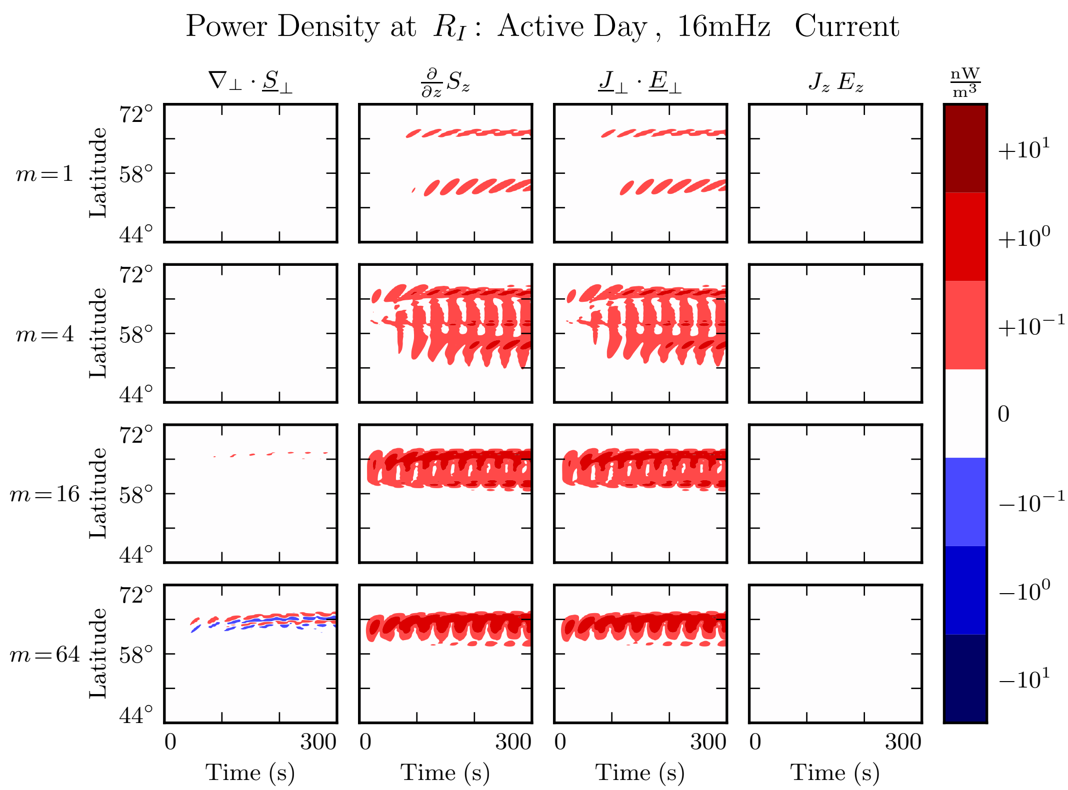

Figure 6.5: While field-aligned currents can be of significant size, they are not particularly good at depositing energy in the ionosphere. Energy deposited by the Poynting flux matches closely with Joule dissipation from the perpendicular currents, while $J_z E_z$ is smaller by several orders of magnitude.

— but according to the model, parallel currents and electric fields do not contribute significantly.

6.3 Inertial Length Scales

It's not quite fair to compare the parallel and perpendicular contributions to $\nabla \times \underline{E}$ as is done in Section 6.2. Perpendicular electric fields are on the order of 1 mV/m, with wavelengths on the order of 10^5 km; they give rise to magnetic field gradients around

0.1 nT/s. Parallel electric fields, closer to 10^{-6} mV/m, would need to vary over length scales of 0.1 km to match with that.

Such scales are believable. The characteristic length scale of the plasma oscillation is the electron inertial length, $\frac{c}{\omega_P}$, which is on the order of 1 km in the auroral ionosphere and 0.1 km in the low-altitude plasmasphere. However, Tuna's usual grid doesn't resolve structures so fine; its resolution bottoms out closer to 10 km. That is, with the inclusion of electron inertial effects, Tuna's grid is too coarse to resolve all of the waves expected to be present. The model is prone to instability as a result.

Figure 6.6 shows a run with perpendicular resolution smaller than the electron inertial length, side by side with an analogous run on the usual grid. In order to carry out the inertial-scale run, several concessions were made to computational cost. The run simulates only a duration of 100 s (other results in previous sections and in Chapter 7 show 300 s), and the grid covers only the auroral latitudes from $L = 5$ to $L = 7$.

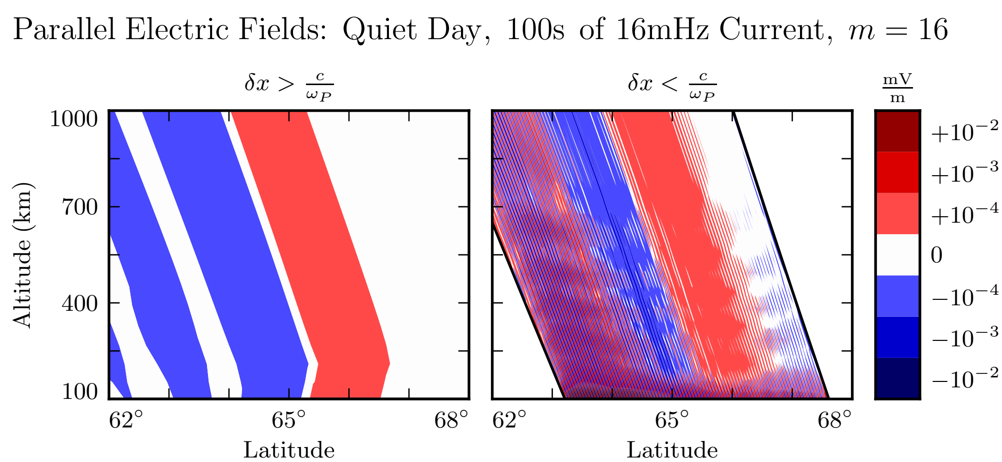

Figure 6.6: The parallel electric field develops significant structure when the perpendicular grid resolution is smaller than the electron inertial length. Unfortunately, such runs are prohibitively expensive. The lower panel — which still fails to resolve wave structure properly — represents a 100-fold increase in computational time.

Even so, the run presents a significant computational expense. Spread over 16 cores, a 100 s run on Tuna's usual grid takes well under an hour. The inertial-scale run barely finished in 96 hours, the cutoff at the Minnesota Supercomputing Institute[7].

The snapshot shown in Figure 6.6 uses a perpendicular grid resolution of 0.7 km at the Earthward edge, which just satisfies the Nyquist rate for the minimum inertial length of 1.7 km. It's still too coarse. There is clearly some small-scale structure developing in the ionosphere, but it's not well resolved. The large number of "wigglies" portends an imminent crash.

6.4 Discussion

TODO: The dispersion relation in Chapter 4 suggests that parallel electric fields should be smaller than perpendicular electric fields by at least six orders of magnitude. Tuna agrees.

TODO: Tuna computes parallel currents a bit weaker than those that are observed — $\sim 1\,\mu\text{A/m}^2$ rather than $\sim 10\,\mu\text{A/m}^2$. The currents accompany the toroidal mode, but not the poloidal mode, except where the two are coupled by a strong Hall conductivity. Is this expected?

TODO: When inertial effects are not properly resolved, the code is prone to instability. Resolving inertial scales properly presents a prohibitive computational expense.

Electron inertial effects present a promising first-principles-based approach to the investigation of parallel currents and electric fields associated with field line resonances. Unfortunately, because of the large differences in scale between Pc4 pulsations and the plasma oscillation, the proper deployment of inertial effects presents a prohibitive computational expense. Results shown in Chapter 7 make use of the core version of Tuna presented in Chapter 5, which does not include the effects of electron inertia.

[7] Runtime goes as the inverse square of grid resolution. Not only does finer resolution require more grid cells, but it also gives rise to proportionally smaller crossing times, imposing a smaller time step.

Chapter 7

Numerical Results

TODO: An overarching motivation for the present work is that FLRs exhibit significant behavioral changes as a result of their azimuthal modenumbers, but that prior models have been unable to provide a good picture.

7.1 Modenumber and Compression

It's well known that the poloidal FLR mode is compressional at low modenumber, but guided at high modenumber. However, the relationship is not well quantified. Theoretical work has historically been concerned with the limits $m \to 0$ and $m \to \infty$[16, 80], and only a handful of satellite observations have explicitly considered an event's azimuthal modenumber[19, 72, 92]. Using results from Tuna, the present section examines the strength of the poloidal wave's compressional component at an ensemble of finite modenumbers.

Figures 7.1 and 7.2 show magnetic field snapshots taken from a pair of runs. The first uses a small azimuthal modenumber, and the second uses a large one. The runs are otherwise identical: both simulations use the quiet dayside ionospheric profile, and both are driven at 22 mHz.

The differences between the two runs are striking. At low modenumber, wave activity is visible throughout the simulation domain. Structure in the poloidal magnetic field is only vaguely governed by the dipole geometry, and the compressional magnetic field is comparably strong to the two perpendicular components.

In contrast, at high modenumber, the poloidal magnetic field is localized to the L-shells where the driving is delivered: $4 \lesssim L \lesssim 6$. The compressional field is weaker than the poloidal field by at least an order of magnitude. A third-harmonic poloidal mode is visible at the outer boundary — its magnitude is just barely large enough to be visible on the logarithmic scale. The gap between $L \sim 5$ (where 22 mHz matches a first-harmonic FLR) and $L \sim 10$ (where 22 mHz matches a third-harmonic FLR) speaks to the evanescence of non-guided waves above the compressional Alfvén cutoff frequency[1].

In both the low-m and high-m runs, toroidal activity is more or less coincident with poloidal activity — as is to be expected, since the driving is purely poloidal, and the poloidal mode rotates to the toroidal mode over time. It is further notable that the toroidal mode is sharply guided. Particularly in Figure 7.2, strong, narrow, toroidal FLRs of opposite phase can be seen oscillating very close to one another. Strong poloidal waves, in contrast, are smeared in L.

Snapshots are not shown for runs carried out using the other ionospheric profiles (active day, quiet night, and active night). The morphology of their waves is qualitatively similar. The differences between the profiles is considered in Sections 7.2 to 7.4.

Figure 7.3 quantifies the compressional component of the poloidal mode as a function of modenumber. Each subplot corresponds to a different run of Tuna — the runs shown in Figures 7.1 and 7.2 are in the rightmost column, second from the top and second from the bottom respectively. The red line indicates the ratio between the RMS compressional magnetic fieldand the RMS poloidal magnetic field; both averages are taken over the entire simulation "volume" each time step. Mean values are shown in black.

[1] See Section 4.4.

At $m = 1$, the compressional and poloidal magnetic fields are comparable in magnitude. As m increases, however, the compressional component quickly falls off. The compressional component is half the strength of the poloidal component at $m \sim 5$, and a quarter by $m \sim 10$.

A slight frequency dependence is apparent across each row in Figure 7.3. Compressional coupling falls off slower for waves at higher frequency. This is because higher-frequency waves are that much closer to the cutoff frequency (described in Section 4.4), and so their propagation across L-shells is that much less evanescent.

Similarly, poloidal waves are more prone to compression on the nightside. Due to the higher Alfvén speed on the nightside, driving is delivered at $L \sim 6$ instead of $L \sim 5$. The cutoff frequency depends inversely on radial distance. For nightside runs (not shown), $\left|\frac{B_z}{B_x}\right|$ falls to $50\,\%$ at $m \sim 8$ and to $25\,\%$ at $m \sim 16$.

Notably, the waves considered in the present work are fundamental harmonics. The compressional behavior of the poloidal mode may vary for the (more-common) second harmonic: Radoski suggests that the asymptotic value of $\left|\frac{B_z}{B_x}\right|$ is inversely proportional to the harmonic number[80].

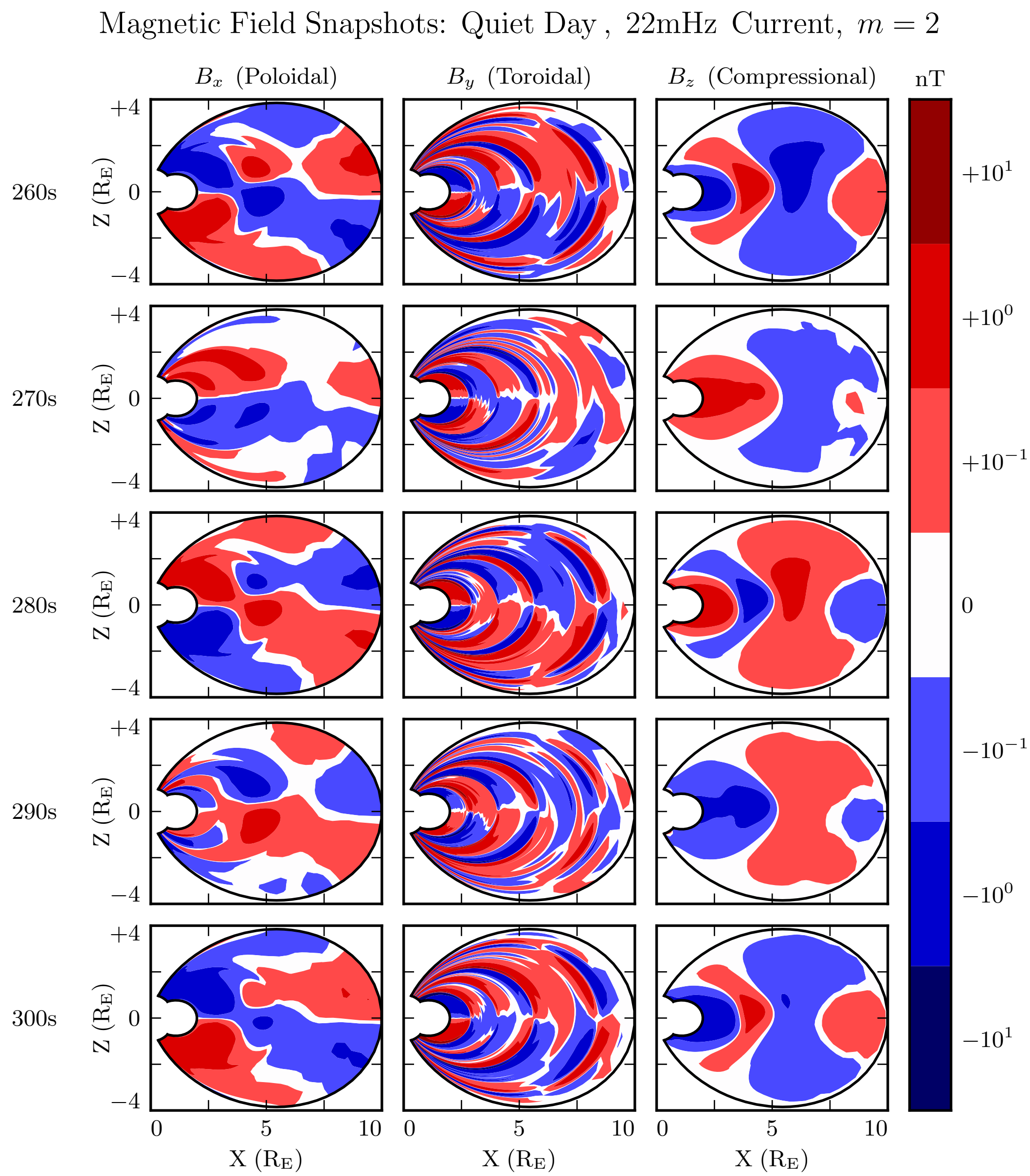

Figure 7.1: Each row in the above figure is a snapshot in time. The three columns show the simulated poloidal, toroidal, and compressional magnetic field. Due to the run's low azimuthal modenumber, the poloidal mode has a significant compressional component. This is visible both in the fact that B_z is comparable in size to B_x, and in that structure in B_x is only vaguely guided by the geometry of the magnetic field. Toroidal waves, in contrast, are sharply guided.

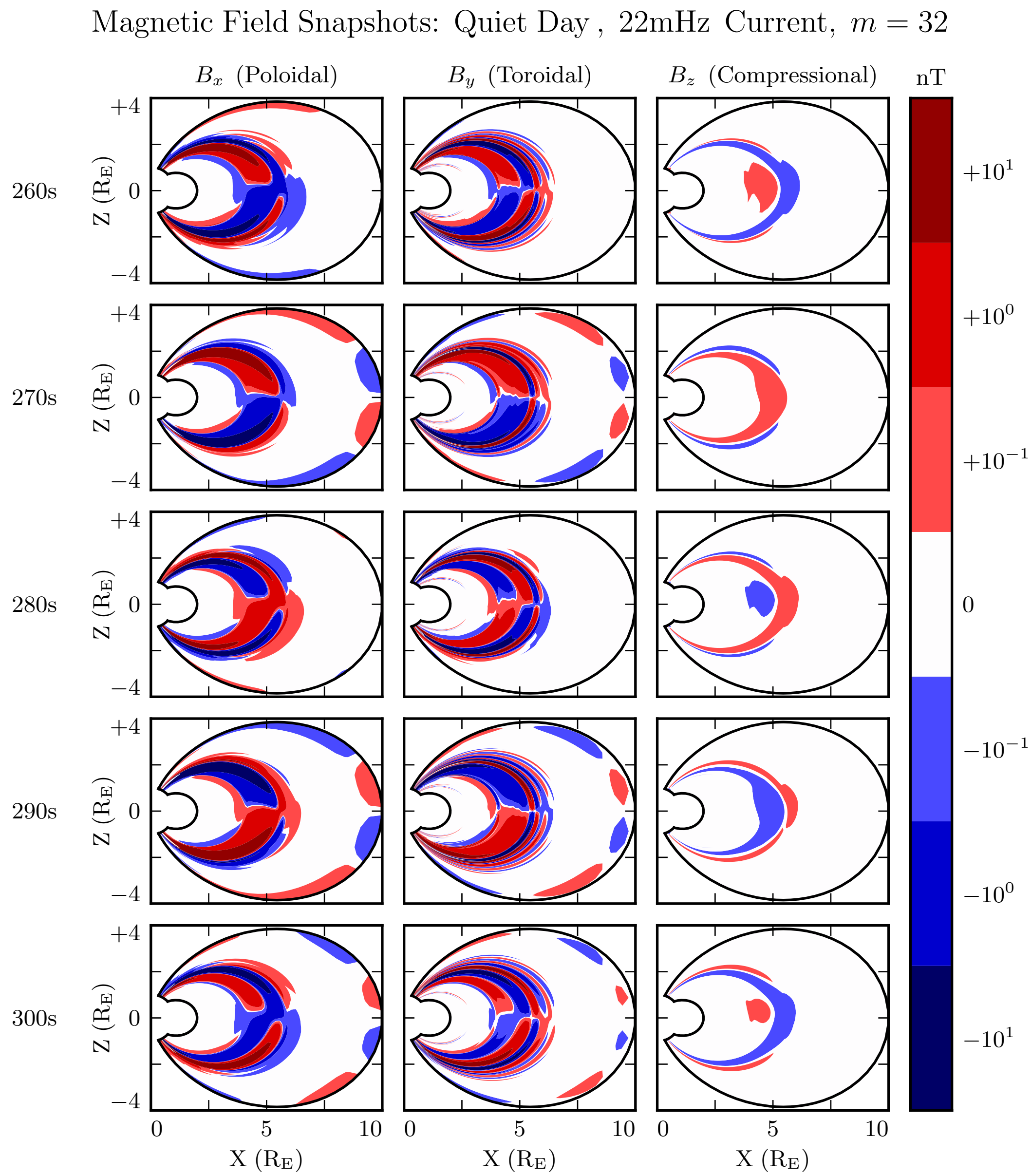

Figure 7.2: The above figure is analogous to Figure 7.1, but the runs use a larger azimuthal modenumber. The change has a dramatic effect. The poloidal wave is concentrated much more sharply in L, and its compressional component is weakener by an order of magnitude. Regardless of modenumber, toroidal waves exist at a range of L shells similar to poloidal waves, and show sharp definition across L-shells.

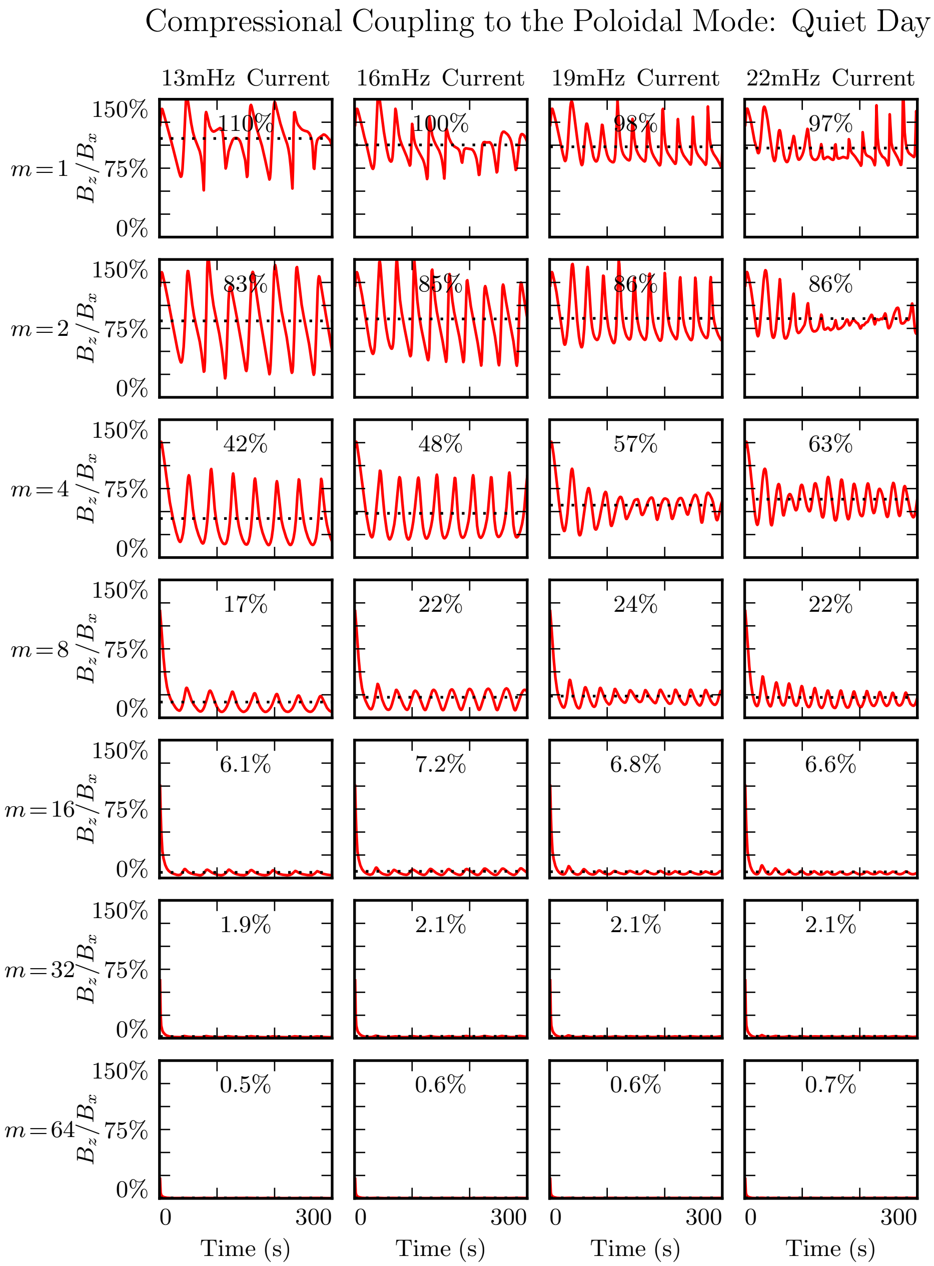

Figure 7.3: Each subplot above corresponds to a different run; the runs shown in Figures 7.1 and 7.2 are in the rightmost column, second from the top and second from the bottom respectively. Red lines indicate the ratio between the RMS compressional and poloidal magnetic fields. Mean values are shown in black. The compressional field is comparable to the poloidal field at $m = 1$, but falls quickly.

7.2 Resonance and Rotation on the Dayside

In his 1974 paper, Radoski argues that a poloidally-polarized wave should asymptotically rotate to the toroidal polarization[80] as a result of the curved derivative in the meridional plane. The question of finite poloidal lifetimes is considered further in a 1995 paper by Mann and Wright[66]. Their numerical work used a straightened field line, with an Alfvén speed gradient in the "radial" direction. They also found a rotation over time from poloidal to toroidal polarization, with the characteristic time proportional to the azimuthal modenumber.

The present section builds on the aforementioned results by relaxing several of their non-physical assumptions. Tuna's geometry is more realistic than Radoski's half-cylinder or the box model usede by Mann and Wright. Previous work has considered the evolution of an initial condition, while the simulations shown below include driving delivered over time. In addition, Tuna features a finite, height-resolved ionospheric conductivity profile, rather than the perfectly-reflecting boundaries used in the past.

Each subplot in Figure 7.4 is analogous to Figure 3 in Mann and Wright's paper[66]. Blue lines show the total energy in the poloidal mode as a function of time. Red lines show toroidal energy. Runs are organized analogous to those in Figure 7.3: drive frequency is constant down each column, and azimuthal modenumer is constant across each row. Axis bounds are held constant across all subplots. The poloidal and toroidal energy are computed by integrating over the electromagnetic energy density, per Poynting's theorem:

$$U_P = \int \frac{dV}{2\mu_0} \left(B_x^2 + \frac{1}{v_A^2} E_y^2 \right) \qquad\qquad U_T = \int \frac{dV}{2\mu_0} \left(B_y^2 + \frac{1}{v_A^2} E_x^2 \right) \tag{7.1}$$

Where the differential volume dV is computed using the Jacobian[2] to account for Tuna's unusual geometry. The integral is evaluated in u^1 and u^3 but not u^2 (Tuna's missing half-dimension), which gives energy in units of gigajoule per radian. More than anything else, this serves as a reminder that Pc4 pulsations are localized in MLT.

[2] See Section 5.1.

The 28 runs shown in Figure 7.4 use an ionospheric profile corresponding to the dayside during times of low solar activity, where the conductivity is relatively high. The active and quiet dayside profiles are briefly contrasted in Section 7.4; for the most part, the focus of the present work is on the difference between the dayside and the nightside (Section 7.3). Differences between the two dayside profiles are small in comparison.

The fact that red (toroidal) lines appear at all in Figure 7.4 speaks to a net rotation of energy from the poloidal mode to the toroidal. As discussed in Section 5.3, Tuna's driving is delivered purely into the poloidal electric field (reflecting a perturbation in the magnitude of the ring current).

As expected, the rotation from poloidal to toroidal is slowest at large azimuthal modenumbers. The toroidal energy overtakes the poloidal energy within a single drive period at $m = 4$; at $m = 64$, the most of the energy is in the poloidal mode for $\sim$10 periods. However, the relationship between azimuthal modenumber and rotation timescale is not linear, as was suggested by Mann and Wright. Instead, in a practical setting, the rotation is fastest at $m \sim 4$.

This is explained by the compressional character of the poloidal mode. At very low modenumber, energy in the poloidal mode moves readily across L-shells. A significant fraction of that energy is lost to the outer boundary before rotating to the toroidal mode. At high modenumber — as discussed in Section 7.1 — compressional propagation is evanescent, so all energy in the poloidal mode must ultimately rotate to the toroidal mode or be lost to Joule dissipation.

Joule dissipation is a major player in the system's energy economy. However, due to the highly conductive dayside ionosphere, dissipation timescales are in the tens of Pc4 wave periods. Energy loss through Joule dissipation asymptotically balances energy input from driving, but most of that energy is not lost until after it has rotated from the poloidal mode to the toroidal. As such, in most runs shown in Figure 7.4, the energy content of the toroidal mode asymptotically exceeds that of the poloidal mode.

The asymptotic energy content of the system also depends on how well the drive frequency matches the local eigenfrequency. If the two do not match, energy is lost to destructive interference between the standing wave and the driving.

In principle, energy moves between the poloidal and toroidal modes due to their direct coupling through the ionospheric Hall conductivity. In practice, this effect is small. When the runs shown in Figure 7.4 are repeated with the Hall conductivity set to zero, the resulting energy curves are not visibly different.

The low-m runs at 19 mHz merit additional discussion. These runs accumulate energy over a large number of wave periods, while the low-m waves at 13 mHz, 16 mHz, and 22 mHz do not. This effect is likely nonphysical. At 19 mHz, a third-harmonic resonance forms very close to the outer boundary. The resonance is likely enhanced by nonphysical reflections against the simulation's boundary conditions.

The presence of individual harmonics can be seen in the contours shown in Figures 7.5 and 7.6. These figures show the same runs as Figure 7.4, arranged in the same way on the page. However, instead of showing the total energy integrated over the simulation domain, the energy densities are averaged over the volume of each flux tube individually. Figure 7.5 shows contours of poloidal energy density and Figure 7.6 shows toroidal energy density.

The top few rows of Figure 7.5 confirm that the poloidal mode's compressional nature is to blame for its failure to accumulate energy at low modenumber. Waves move so readily across field lines that no visible amount of energy builds up at $L \sim 5$, the location of the driving. Some energy moves inward, and is trapped by the peak in Alfvén speed just inside the plasmapause, while the rest moves to the outer boundary. The time spent moving across field lines counts against the poloidal mode's finite lifetime, inhibiting the buildup of poloidal energy density even at L-shells where the wave matches the local eigenfrequency.

As m increases, the energy distribution becomes more concentrated in L, though individual features remain fairly broad. At $m = 8$, runs at 13 mHz and 16 mHz are inclined to build up energy just inside the plasmapause, while those at 19 mHz and 22 mHz resonate just outside the plasmapause; in all four cases, the energy is spread over a range of at least 1 in L.

The peak energy density in the bottom-right run (22 mHz driving, $m = 64$) is by far the largest of any run in Figure 7.5. The azimuthal modenumber is large, so the poloidal mode is purely guided; energy is not smeared across multiple L-shells. And, crucially, the frequency of the driving matches closely with the Alfvén frequency at $L \sim 5$. Other runs on the bottom row are also guided, but they reach lower asymptotic energy densities because of a mismatch between the drive frequency and the local eigenfrequency — resulting in destructive interference between the standing wave and its driver.

The eigenfrequencies in the magnetosphere are significantly affected by the location of the plasmapause. When the runs in Figure 7.5 are repeated with the plasmapause at $L = 5$ instead of $L = 4$, the strongest resonance at $L \sim 5$ drops from 22 mHz to 16 mHz (not shown).

Whereas the poloidal contours are smeared over a swath of L-shells (though the high-m runs less so), the toroidal contours in Figure 7.6 appear only where the wave frequency matches the local eigenfrequency. A horizontal line drawn through the Alfvén speed frequency profiles (recall Figure 3.1) intersects the profile up to three times: once as the Alfvén frequency drops through the Pc4 range from its low-latitude peak, again as the Alfvén frequency rises sharply at the plasmapause, and a third time as the Alfvén frequency drops asymptotically. Toroidal waves can be seen resonating at all three of these locations in the $m = 4$, 22 mHz run in Figure 7.6, along with a third harmonic at large L. This is consistent with observations: toroidal resonances are noted for having frequencies which depend strongly on L, in contrast to the poloidal mode's less-strict relationship between frequency and location.

In only one of the runs shown in Figure 7.5 does the poloidal mode attain an energy density on the order of $10^{-1}\,\mathrm{nJ/m^3}$. On the other hand, the toroidal mode reaches $\sim 10^{-1}\,\mathrm{nJ/m^3}$ in six of the runs in Figure 7.6. That is, the poloidal mode only exhibits a high energy density on the dayside only when conditions are ideal; the toroidal mode isn't nearly so particular.

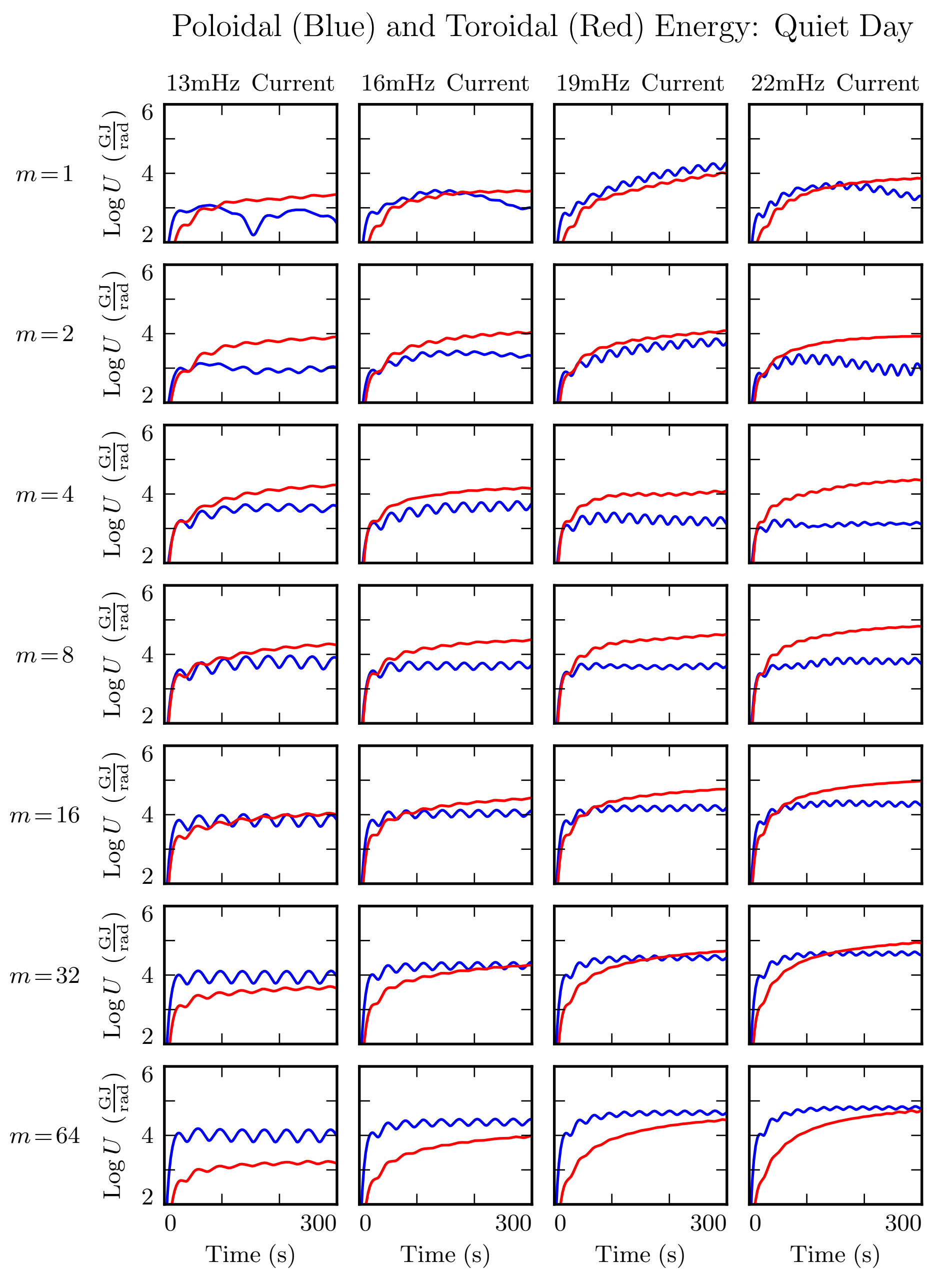

Figure 7.4: TODO: Lorem ipsum dolor sit amet, consectetur adipiscing elit, sed do eiusmod tempor incididunt ut labore et dolore magna aliqua. Ut enim ad minim veniam, quis nostrud exercitation ullamco laboris nisi ut aliquip ex ea commodo consequat. Duis aute irure dolor in reprehenderit in voluptate velit esse cillum dolore eu fugiat nulla pariatur.

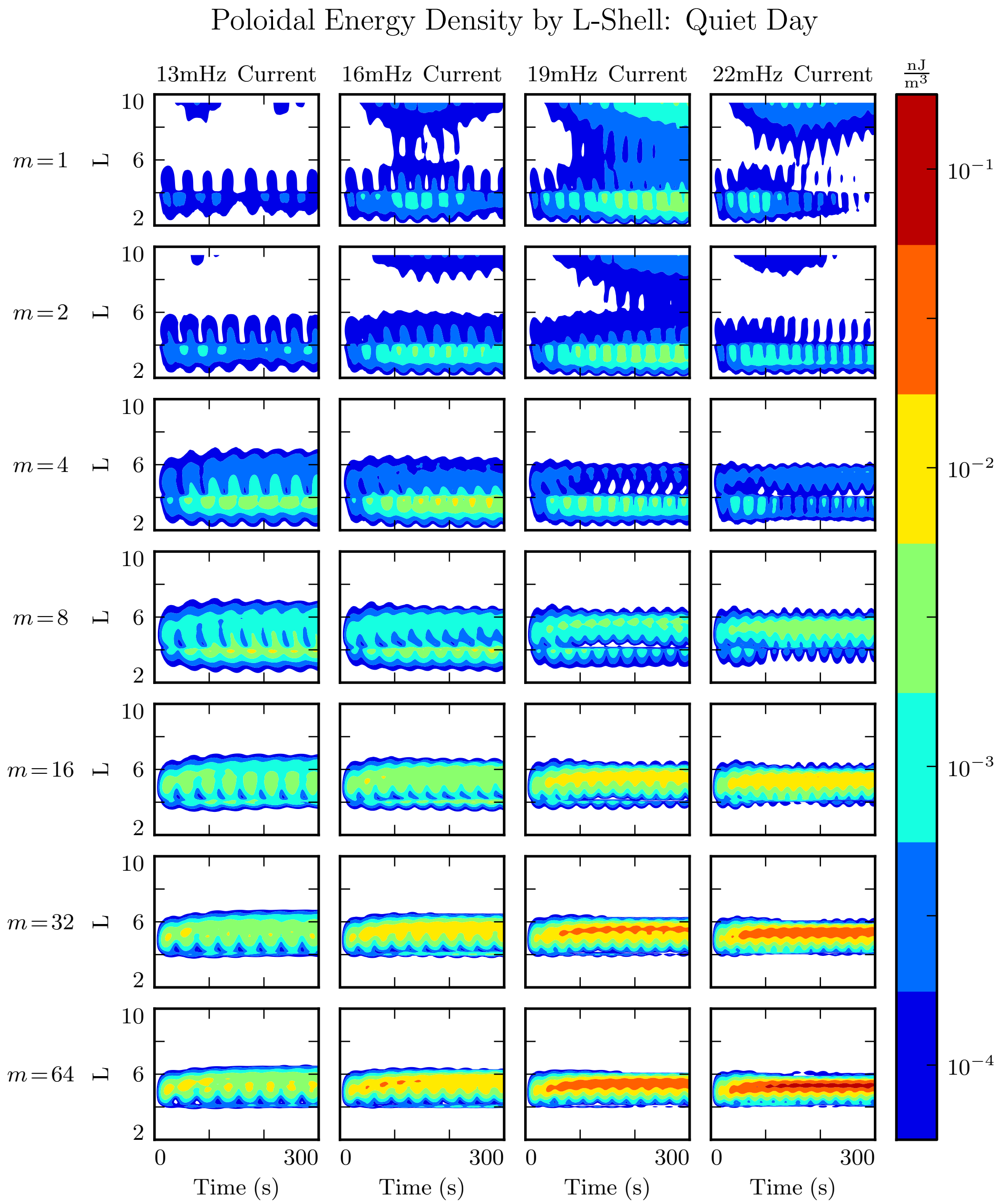

Figure 7.5: TODO: Lorem ipsum dolor sit amet, consectetur adipiscing elit, sed do eiusmod tempor incididunt ut labore et dolore magna aliqua. Ut enim ad minim veniam, quis nostrud exercitation ullamco laboris nisi ut aliquip ex ea commodo consequat. Duis aute irure dolor in reprehenderit in voluptate velit esse cillum dolore eu fugiat nulla pariatur.

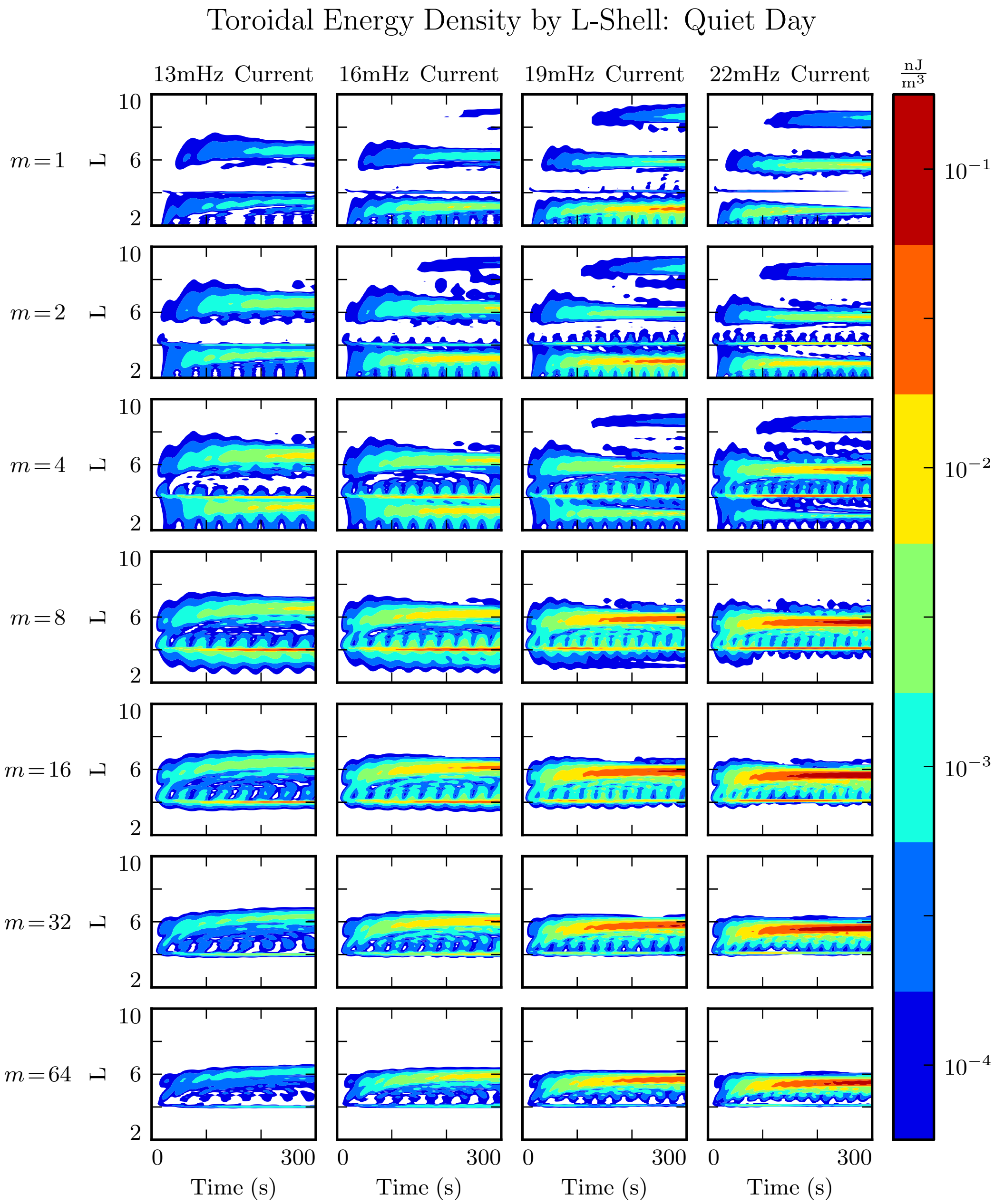

Figure 7.6: TODO: Lorem ipsum dolor sit amet, consectetur adipiscing elit, sed do eiusmod tempor incididunt ut labore et dolore magna aliqua. Ut enim ad minim veniam, quis nostrud exercitation ullamco laboris nisi ut aliquip ex ea commodo consequat. Duis aute irure dolor in reprehenderit in voluptate velit esse cillum dolore eu fugiat nulla pariatur.

7.3 Resonance and Rotation on the Nightside

TODO: ACTUALLY we should show the runs driven at $L \sim 5$ across the board. Dayside and nightside. That way we can make a fair comparison.

Compared to the dayside ionosphere employed in Section 7.2, the nightside exhibits two major differences. The ionospheric conductivity is lower, and the Alfvén speed is higher. As a result of the higher Alfvén speed, driving on the nightside is delivered at $L \sim 6$ instead of $L \sim 5$. Runs in the present section specifically use Tuna's ionospheric profile corresponding to the nightside during quiet solar conditions; the active nightside is discussed briefly in Section 7.4, but for the most part the present work is concerned with the behavior of the nightside compared to that on the dayside.

Other than the change in ionospheric profile, Figures 7.7 to 7.9 are analogous to Figures 7.4 to 7.6. Each subplot corresponds to a different 300 s run of Tuna. Drive frequency is constant down each column, and azimuthal modenumber is constant across each row.

The low conductivity on the nightside gives rise to strong Joule dissipation. Waves are damped out in just a few bounces, so asymptotic energy values are reached quickly. No combination of frequency and modenumber gives rise to the accumulation of energy over multiple drive periods.

As on the dayside, rotation of energy from the poloidal to toroidal mode is fastest at $m \sim 4$. Unlike the dayside, however, dissipation on the nightside is fast compared to the rotation of energy to the toroidal mode. Toroidal energy does not asymptotically exceed the poloidal energy by a significant margin in any run. At $m = 64$, where the rotation timescale is slowest, no more than TODO: $\cdots$ of the energy in the poloidal mode rotates to the toroidal mode before being lost.

TODO: The damping on the quiet nightside is so severe that basically nothing resonates anywhere. Should we show the active nightside instead?

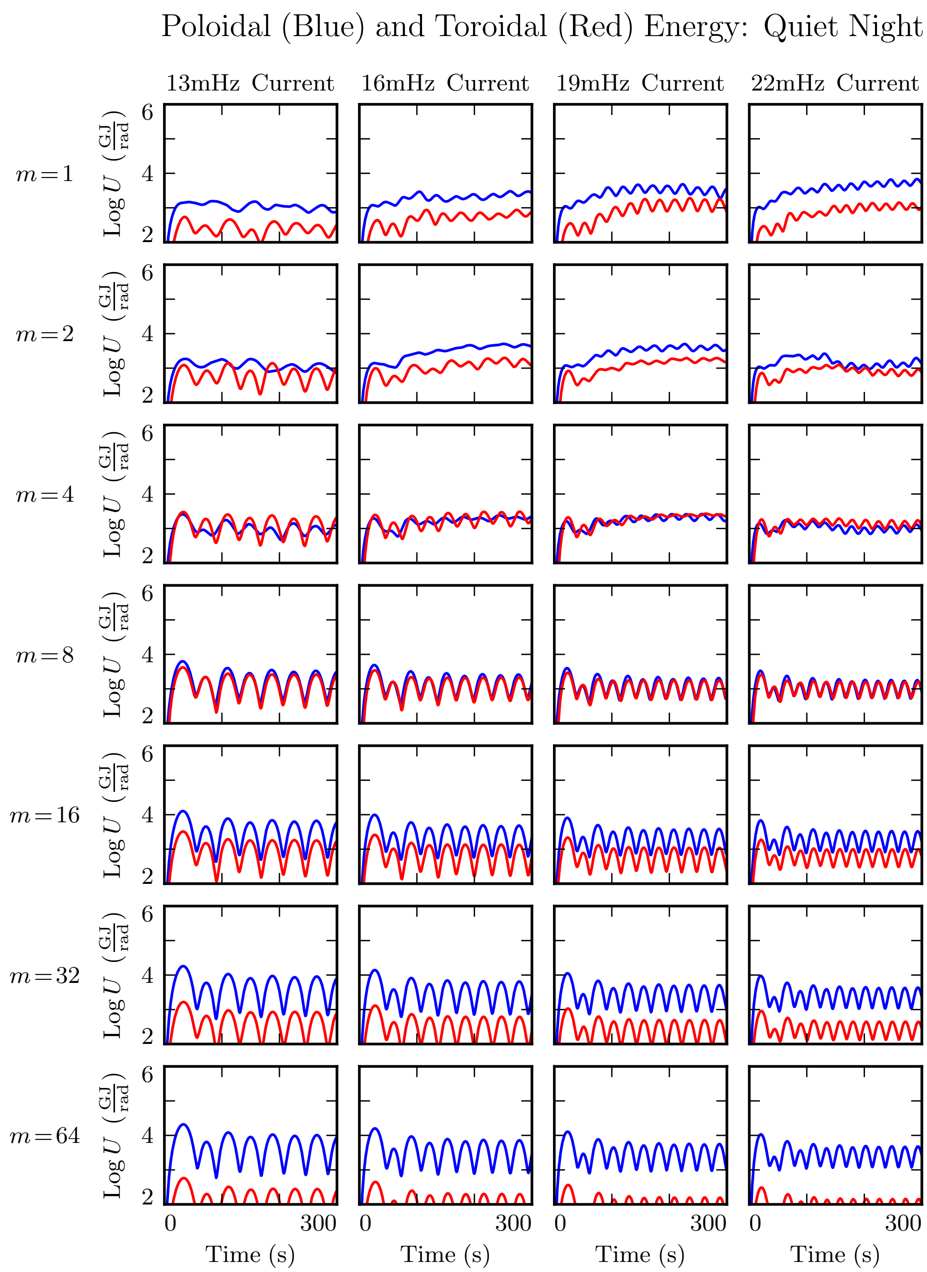

Figure 7.7: TODO: Lorem ipsum dolor sit amet, consectetur adipiscing elit, sed do eiusmod tempor incididunt ut labore et dolore magna aliqua. Ut enim ad minim veniam, quis nostrud exercitation ullamco laboris nisi ut aliquip ex ea commodo consequat. Duis aute irure dolor in reprehenderit in voluptate velit esse cillum dolore eu fugiat nulla pariatur.

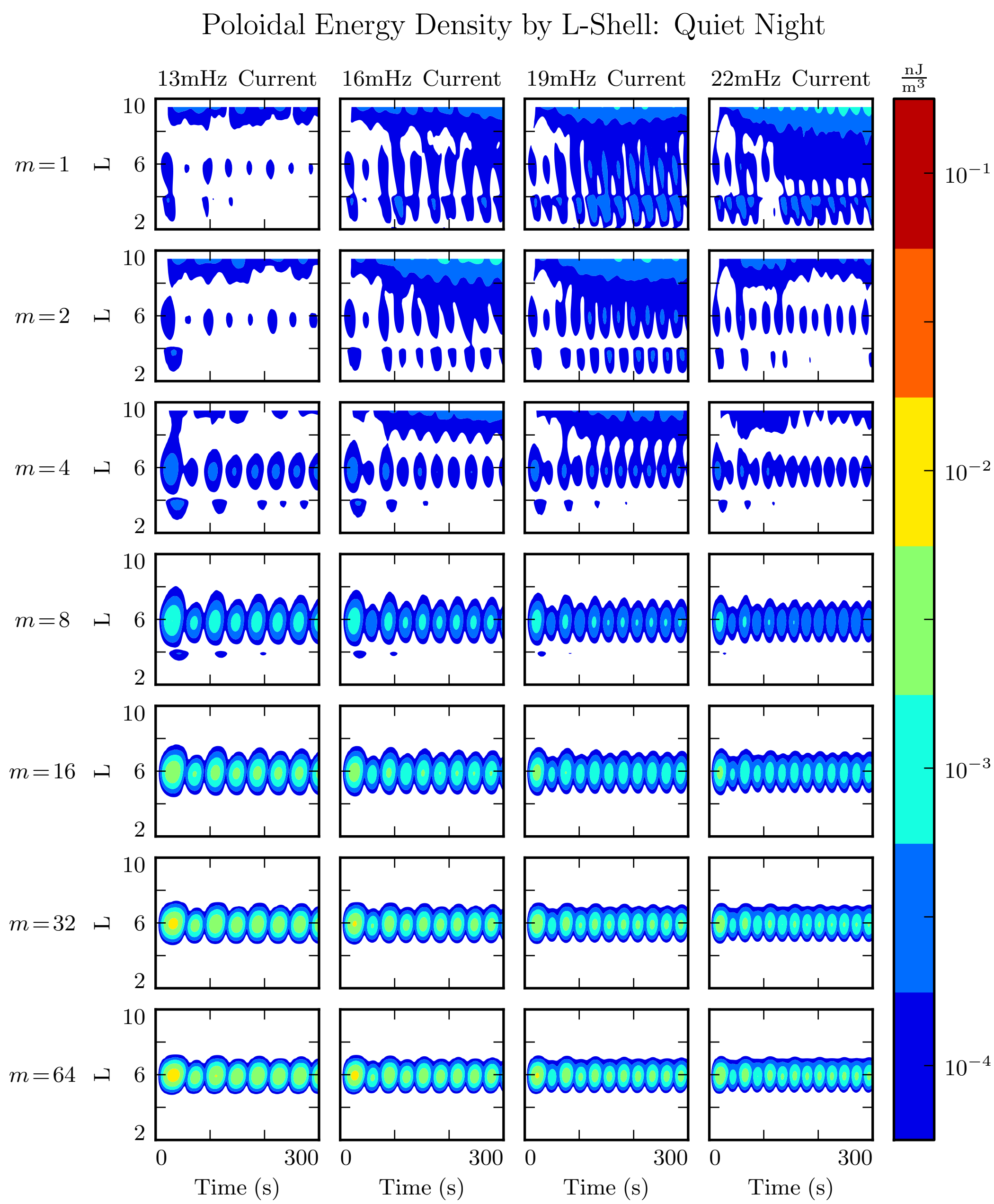

Figure 7.8: TODO: Lorem ipsum dolor sit amet, consectetur adipiscing elit, sed do eiusmod tempor incididunt ut labore et dolore magna aliqua. Ut enim ad minim veniam, quis nostrud exercitation ullamco laboris nisi ut aliquip ex ea commodo consequat. Duis aute irure dolor in reprehenderit in voluptate velit esse cillum dolore eu fugiat nulla pariatur.

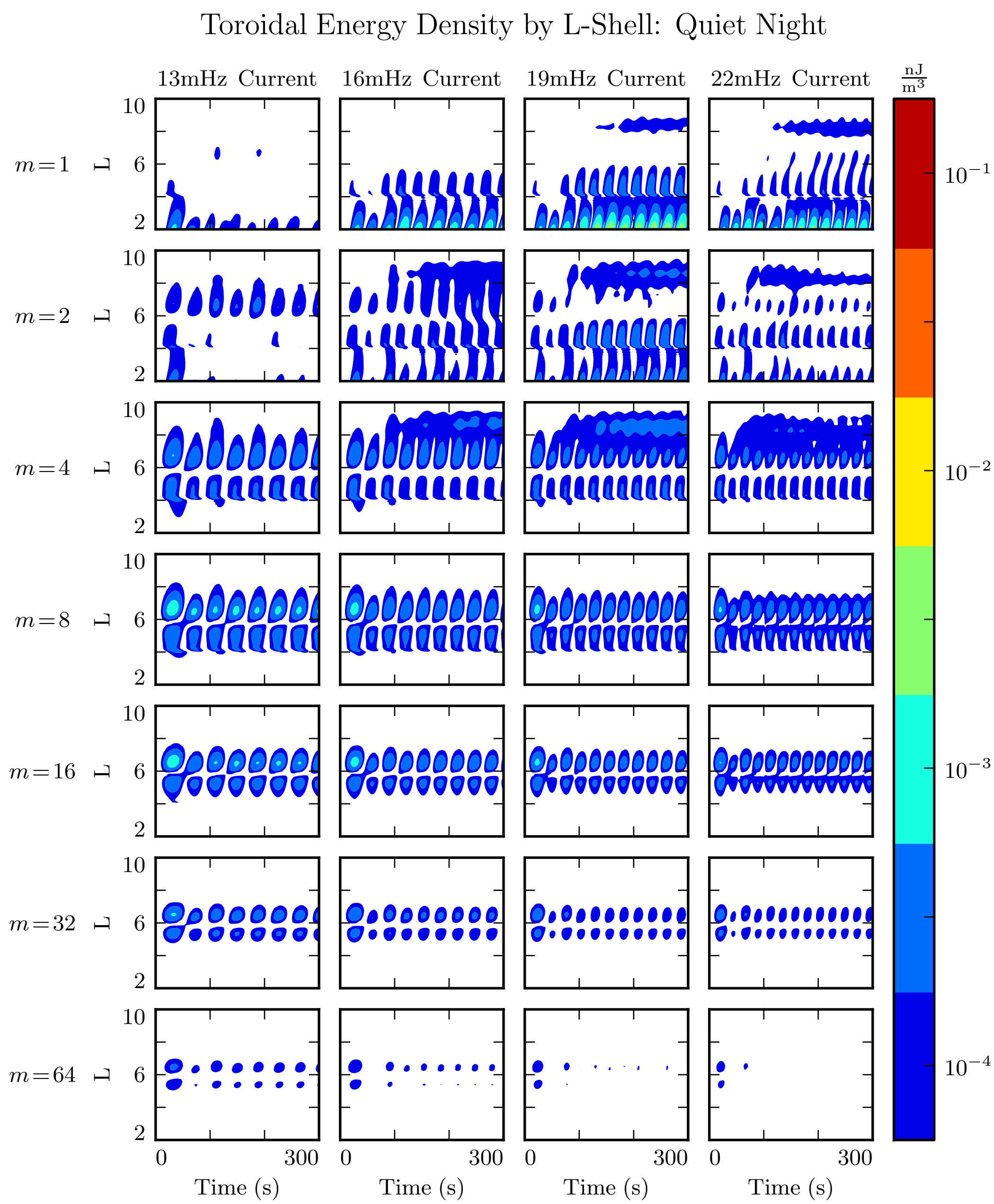

Figure 7.9: TODO: Lorem ipsum dolor sit amet, consectetur adipiscing elit, sed do eiusmod tempor incididunt ut labore et dolore magna aliqua. Ut enim ad minim veniam, quis nostrud exercitation ullamco laboris nisi ut aliquip ex ea commodo consequat. Duis aute irure dolor in reprehenderit in voluptate velit esse cillum dolore eu fugiat nulla pariatur.

7.4 Ground Signatures and Giant Pulsations

TODO: Pgs show counterclockwise at low latitude and clockwise at high latitude. We see that! Regardless of latitude, B_ϕ is always at the same phase with respect to the driving. But B_θ has a phase which varies by latitude.

While the majority of the action is in space, the majority of FLR observations have historically been ground-based. The present section explores the same simulations discussed in Sections 7.2 and 7.3, but in terms of their ground signatures rather than their broad energy distributions.

As in the figures shown in Sections 7.2 and 7.3, each row in Figures 7.10 and 7.11 shows runs at a different modenumber. The columns are magnetic field contours; the vertical axis is latitude, and the horizontal axis is time. The four columns are components of the magnetic field signatures at the ground: the north-south magnetic field (first and third columns) and the east-west magnetic field (second and fourth columns). The pair on the left show a simulation carried out using the active ionospheric profile, and the pair on the right show a simulation using the quiet profile.

Notably, the magnetic polarization of a low frequency Alfvén wave is rotated by $\sim 90^\circ$ as it passes through the ionosphere[42]. The east-west field on the ground (B_ϕ) corresponds to the poloidal polarization in space, and the north-south field on the ground (B_θ) corresponds to the toroidal mode.

The most striking feature of Figures 7.10 and 7.11 is the modenumber dependence. As modenumber increases, the magnetic field signatures become sharply localized in latitude. At high m, ground signatures are concentrated between 60° and 70°, peaking near 64° on the dayside and 66° on the nightside. Appropriately enough, these latitudes lie at the $L \sim 5$ and $L \sim 6$ respectively.

TODO: Is it weird that we see no ducting from the ionosphere? Does the ionosphere duct ULF waves in the θ direction, or just in ϕ?

At low modenumber, magnetic signatures are weak on the ground because the waves in space are also weak. At high modenumber, waves in space are strong, but so is the attenuation of magnetic signatures by the ionosphere[3]. The “sweet spot” at which magnetic ground signatures are maximized falls at $m = 16$ to $m = 32$.

Tuna shows stronger ground signatures on the dayside than on the nightside, more or less in proportion with the difference in magnitude in space. Energy on the dayside (which depends on field magnitude squared) peaks an order of magnitude larger than that on the nightside. Peak ground signatures on the dayside are larger by a factor of five: 45 nT compared to 10 nT. On both the dayside and the nightside, peak ground signatures are in B_ϕ, the east-west magnetic field component; both are also at $m = 16$, and both are seen in runs using the ionospheric profile for quiet solar activity.

TODO: Check the other frequencies to make sure these are the real maxima. Probably also should print the maximum magnitude at the bottom of the subplot.

These results match well with observations of giant pulsations, which tend to be east-west polarized, and are most often observed near 66°, with azimuthal modenumbers of 16 to 35, at the bottom of the solar cycle[95]. Pgs are most commonly observed pre-dawn, but dawn and dusk ionospheric profiles are not implemented for Tuna at present.

[3] See Equation (3.3).

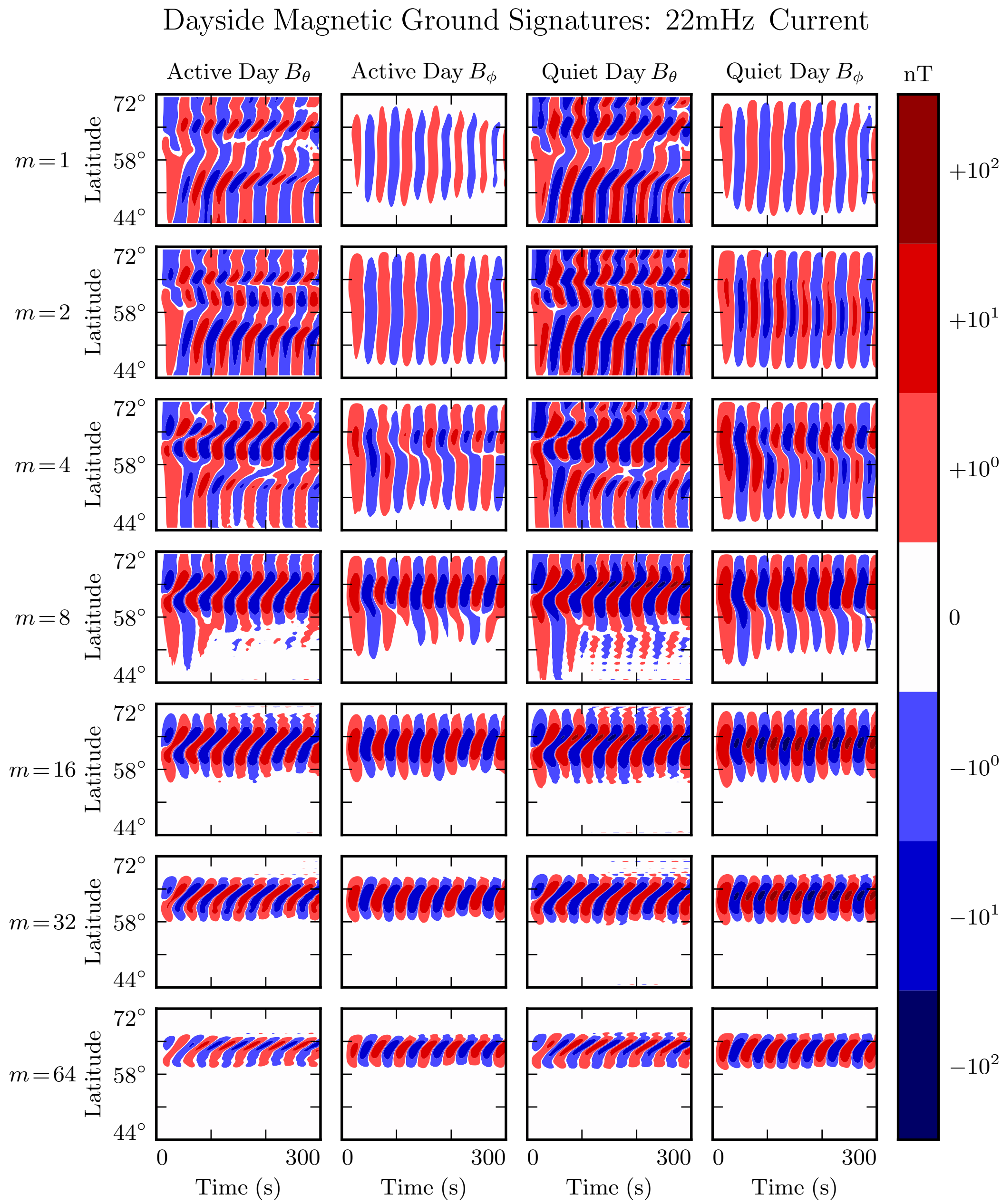

Figure 7.10: TODO: Lorem ipsum dolor sit amet, consectetur adipiscing elit, sed do eiusmod tempor incididunt ut labore et dolore magna aliqua. Ut enim ad minim veniam, quis nostrud exercitation ullamco laboris nisi ut aliquip ex ea commodo consequat. Duis aute irure dolor in reprehenderit in voluptate velit esse cillum dolore eu fugiat nulla pariatur.

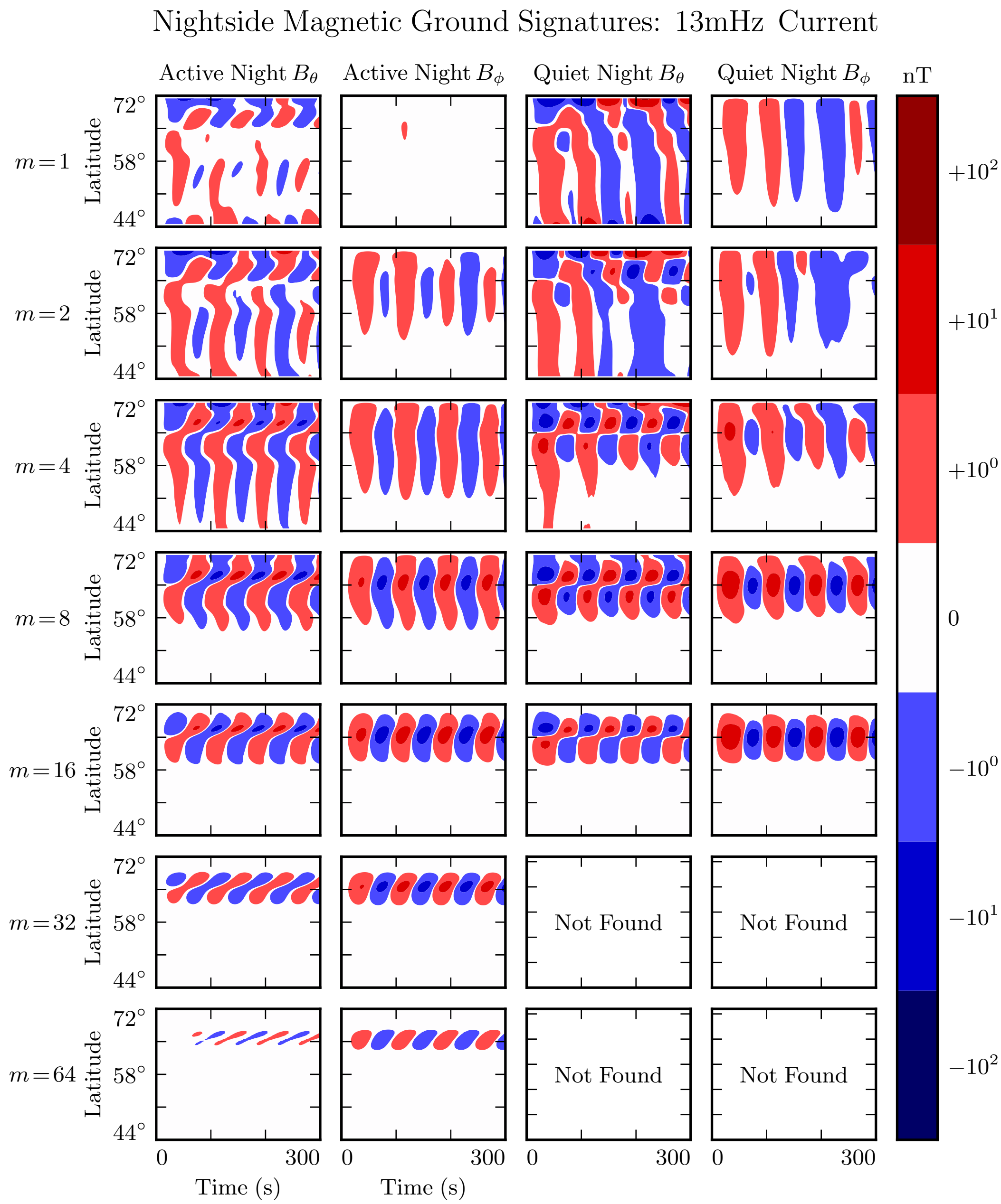

Figure 7.11: Nightside ground signatures are less strongly peaked than those on the dayside, but qualitative features are the same: the strongest signals are in B_ϕ, peaked over just a few degrees in latitude, at a modenumber of 16 or 32, under quiet ionospheric conditions.

7.5 Discussion

TODO: Make this section read nicely.

Poloidal FLRs rotate to the toroidal mode over time. Toroidal modes do not appear to rotate back to the poloidal mode. When m is small, the rotation is comparable to an oscillation period; when m is large, rotation timescales are comparable to ten periods, sometimes more.

On the dayside, little damping takes place over rotation timescales, so the toroidal mode asymptotically exceeds the toroidal mode. The exception is waves with low modenumber, where poloidal waves can escape by propagating across field lines. An evaluation of what happens then — whether they bounce back off the magnetopause, for example — is beyond the scope of the present work.

On the nightside, the conductivity of the ionosphere is low enough that damping timescales become comparable to oscillation timescales. Waves are weaker, since they are unable to accumulate energy over as many periods. High-m toroidal waves are particularly weak, since the dissipation timescale is faster than the poloidal-to-toroidal rotation timescale.

Waves resonate best when the frequency of the driving matches the local eigenfrequency where it's delivered. The eigenfrequency is significantly affected by the size of the plasmasphere.

The poloidal mode, due to its compressional character, exhibits an energy profile which is smeared in L. The toroidal mode, on the other hand, forms sharp resonances where the drive frequency matches the local eigenfrequency. This may explain why the observed frequencies of poloidal waves depend weakly on L, while the frequencies of toroidal waves are strongly dependent on L.

At low m, ground signatures are weak because waves in space are weak because energy can easily escape through the simulation's outer boundary. At large m, ground signatures are attenuated by the ionosphere. The "sweet spot" in azimuthal modenumber at which ground signatures are strongest is around 16 to 32. Furthermore, ground signatures are strongest when ionospheric profiles corresponding to solar minimum are used.

Driving in the poloidal electric field gives rise to primarily ground signatures polarized primarily in the east-west direction at the ground. And, when the frequency of the driving does not match the local eigenfrequency, the high-m resonates weakly in place, rather than tunneling across field lines to resonate strongly somewhere else.

These findings imply, awkwardly, that the morphology of giant pulsations may reveal relatively little about their origins. One can consider a hypothetical magnetosphere subject to constant driving: broadband in frequency, broadband in modenumber, just outside the plasmapause. Low-m poloidal waves will quickly rotate to the toroidal mode (and/or propagate away). High-m waves will resonate in place, accumulating energy over time, and giving rise to "multiharmonic toroidal waves"[91]; Fourier components that do not match the local eigenfrequency will quickly asymptote. Waves with very high modenumbers will be attenuated by the ionosphere. The response on the ground will be significantly stronger during quiet solar conditions. In other words, the measurements on the ground will look very much like a giant pulsation.

TODO: Notably, the present work offers no explanation as to Pgs' distinctive distribution in MLT!

Chapter 8

Van Allen Probe Observations

The results presented in Chapter 7 are interesting on their own, but become particularly valuable when combined with observational data. Unfortunately, only a small number of studies to date have explored how Pc4 observation rate is affected by the harmonic and polarization structure of those waves.

While Pc4 pulsations have previously been studied in terms of both harmonic[5, 16, 28, 45, 85, 94] and polarization[3, 18, 19, 53, 57], little work has considered both at the same time. This has largely been due to observational constraints. The classification of a wave's harmonic is best carried out by computing the phase offset of the magnetic and electric field waveforms, simultaneous in situ measurements of which have only recently become available as part of the THEMIS[4] and Van Allen Probe[88] missions. The Van Allen Probes (launched in 2012) are particularly well-suited to the study of Pc4 pulsations as their apogee of $L \sim 6$ coincides closely with eigenfrequencies in the Pc4 range.

The present chapter uses data from the Van Allen Probes' EFW instrument[105] to survey the occurrence rate of FLRs in the Pc4 range as a function of harmonic parity and polarization, as well as magnitude, frequency, and phase. The tools used to perform the present analysis — SPEDAS and the SPICE kernel — are publicly available. They, along with the Python routines used to download, filter, and plot the data, can be found in a Git repository at `https://github.com/chizarlicious/RBSP`.

TODO: Set this up, along with Tuna, at `https://github.com/chizarlicious/UMN_Space-Physics`.

8.1 Sampling Bias and Event Selection

The present analysis makes use of Van Allen Probe data from October 2012 to August 2015 — the entire range available at the time of writing. Between the two probes, that's just over 2000 days of observation.

For the purposes of Pc4 pulsations, it's reasonable to consider the two probes to be independent observers. Nearly all Pc4 events occur near apogee ($L \gtrsim 5$), at which point the two probes are several hours apart in MLT. Pc4 events are typically not large enough to be seen by both probes simultaneously, and not long enough in duration to be seen by two probes passing through the same region of space several hours apart.

TODO: Quantify how often an event is seen by both probes?

Electric and magnetic field waveforms are collected using the probes' EFW and EMFISIS instruments respectively. Values are cleaned up by averaging over the ten-second spin period. Three-dimensional electric field data is then obtained using the $\underline{E} \cdot \underline{B} = 0$ assumption. Notably, this assumption is taken only when the probe's spin plane is offset from the magnetic field by at least 15°. The rest of the data — about half — is discarded, which introduces a sampling bias against the flanks.

A further bias is introduced by the probes' non-integer number of precessions around Earth. As of July 2014, apogee had precessed once around Earth[18]. The present work considers roughly one and a half precessions; the nightside has been sampled at apogee twice as often as the dayside.

The spatial distribution of usable data — that is, data for which three-dimensional electric and magnetic fields are available — is shown in Figure 8.1. Bins are unitary in L and in MLT. Distribution in magnetic latitude is not shown; the Van Allen Probes are localized to within $\sim$10° of the equatorial plane.

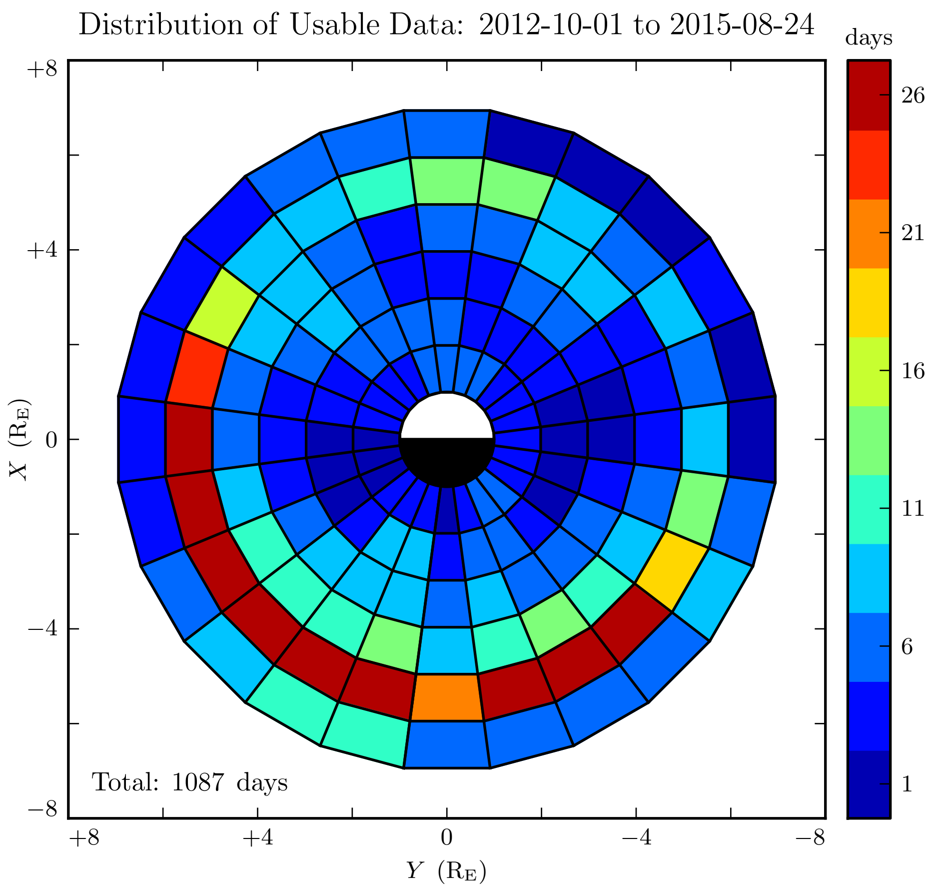

Figure 8.1: Three-dimensional electric field values are computed by assuming $\underline{E} \cdot \underline{B} = 0$. Data is discarded whenever the magnetic field falls within 15° of the spin plane, which introduces a bias against the flanks. Furthermore, the probes have completed one and a half precessions around Earth; the dayside has been sampled once at apogee, and the nightside twice.

Field measurements are transformed from GSE coordinates into the same dipole coordinates used in Chapters 5 and 7. The z axis (parallel to the background magnetic field) is estimated using a ten-minute running average of the magnetic field measurements. The y axis is set parallel to $\hat{z} \times \underline{r}$, where $\underline{r}$ is the probe's geocentric position vector. The x axis is then defined per $\hat{x} \equiv \hat{y} \times \hat{z}$. This scheme guarantees that the axes are right-handed and pairwise orthogonal[57].

The ∼1000 days of usable data are considered half an hour at a time, which gives a frequency resolution of ∼0.5 mHz in the discrete Fourier transform. Spectra are computed for all six field components: $\widetilde{B}_x$, $\widetilde{B}_y$, $\widetilde{B}_z$, $\widetilde{E}_x$, $\widetilde{E}_y$, and $\widetilde{E}_z$. The background magnetic field is subtracted before transforming the magnetic field components, leaving only the perturbation along each axis[1]. Each waveform is also shifted vertically so that its mean over the thirty minute event is zero.

Frequency-domain Poynting flux is computed from the electric and magnetic field transforms. A factor of L^3 compensates the compression of the flux tube, so that the resulting values are effective at the ionosphere. Poloidal and toroidal Poynting flux, respectively, are given by:

$$\widetilde{S}_P \equiv -\frac{L^3}{\mu_0}\widetilde{E}_y\widetilde{B}_x^* \qquad\qquad \widetilde{S}_T \equiv \frac{L^3}{\mu_0}\widetilde{E}_x\widetilde{B}_y^* \tag{8.1}$$

The poloidal and toroidal channels are independently checked for Pc4 waves. For each channel, a Gaussian profile is fit to the magnitude of the Poynting flux, $|\widetilde{S}(\omega)\,|$. If the fit fails to converge, or if the peak of the Gaussian does not fall within 5 mHz of the peak value of $\widetilde{S}$, the event is discarded. Events are also discarded if their frequencies fall outside the Pc4 frequency range (7 mHz to 25 mHz) or if their amplitudes fall below $10^{-2}\,\mathrm{mW/m^2}$ (out of consideration for instrument sensitivity).

Events are discarded if their parity is ambiguous. The electric field and the magnetic field must be coherent at a level of 0.9 or better (judged at the discrete Fourier transform point closest to the peak of the Gaussian fit). Any event within 3° of the magnetic equator is also not used; as discussed in Chapter 3, in order to distinguish an odd mode from an even mode, it's necessary to know whether the observation is made north or south of the equator.

TODO: How much time do the probes spend within 3° of the magnetic equator?

A visual inspection of events shows that those with broad "peaks" in their spectra are typically not peaked at all — they are noisy spectra with several spectral features grouped just closely enough to trick the fitting routine. A threshold is set at a FWHM

[1]As in Chapters 5 and 7, B_x, refers not to the full magnetic field in the x direction, but to the perturbation in the x direction from the zeroth-order magnetic field. The same is true for B_y and B_z.

of 3 mHz (equally, a standard deviation of 1.27 mHz). Any event with a Gaussian fit broader than that is discarded.

Notably, events are not filtered on their phase — that is, on the division of their energy between standing and traveling waves. This is the topic of Section 8.5.

TODO: Are we biased in terms of DST? What's the distribution look like for the good data and for the bad data?

8.2 Events by Mode

The filters described in Section 8.1 yield 762 Pc4 events, the spatial distribution of which is shown in Figure 8.2. In each bin, the event count is normalized to the amount of usable data, per Figure 8.1. Bins shown in white contain zero events. The rate in the bottom corner is an overall mean, weighing each bin equally.

TODO: Bins should be weighted by L. The small inner bins count too much right now, and are dragging down the average.

Consistent with previous work, Pc4 events peak on the dayside and are rarely observed at $L < 4$. Nearly 30 % of the usable data shown in Figure 8.1 is taken at $L < 4$, yet only 16 of the 762 events appear there.

On the other hand, the present work runs contrary to Dai's 2015 result in terms of Pc4 event rates with respect to the plasmapause (not shown). His analysis found (poloidal) Pc4 pulsations to be comparably common inside and outside the plasmapause[18]. In the present work, only 40 of the 762 events (5 %) fall inside the plasmasphere, despite the fact that 40 % of the available data falls within the plasmasphere. The disparity is not likely due to a difference in sampling — Dai's work, like the present work, uses data from the Van Allen Probes mission. Rather, the difference is likely due to disagreement in how the plasmapause is defined. Dai identifies the plasmapause by the maximum gradient in electron number density, while the present work takes an electron density of $100\,/\mathrm{cm}^3$ to mark the plasmapause[2].

[2] Per ongoing work by Thaller.

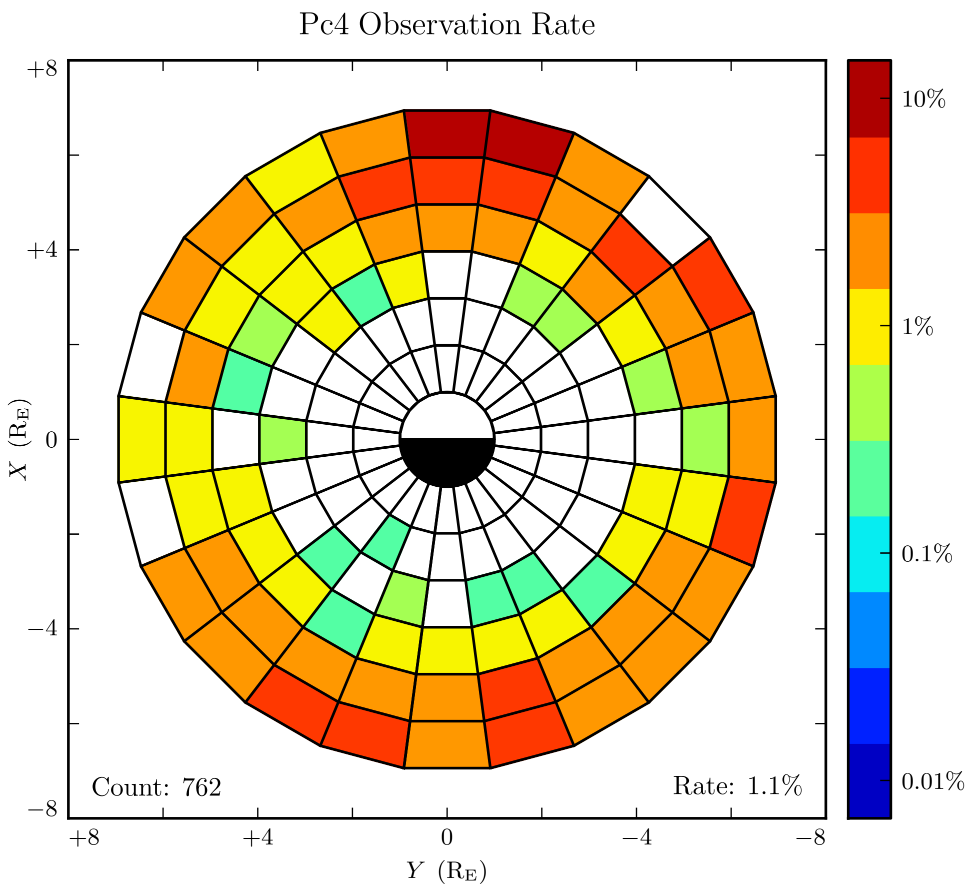

Figure 8.2: The above figure shows the spatial distribution of all 762 observed Pc4 events. Counts are normalized by the amount of usable data in each bin. The value in the bottom-right corner is the mean of the rate in each bin; it's an estimate of how often Pc4 events would be observed if the sampling were distributed uniformly in space. Events where the poloidal and toroidal channel trigger simultaneously (~10 % of cases) are counted as only a single event. Bins shown in white contain zero events.

In Figure 8.3, events are partitioned by parity and polarization, yielding 124 odd poloidal events, 214 even poloidal events, 415 odd toroidal events, and 83 even toroidal events — a total of 836 events. The total is greater than 762 because in ~10 % of events, the poloidal and toroidal channels trigger independently. Such cases are marked as a single event in Figure 8.2, but the toroidal and poloidal events are both shown in Figure 8.3.

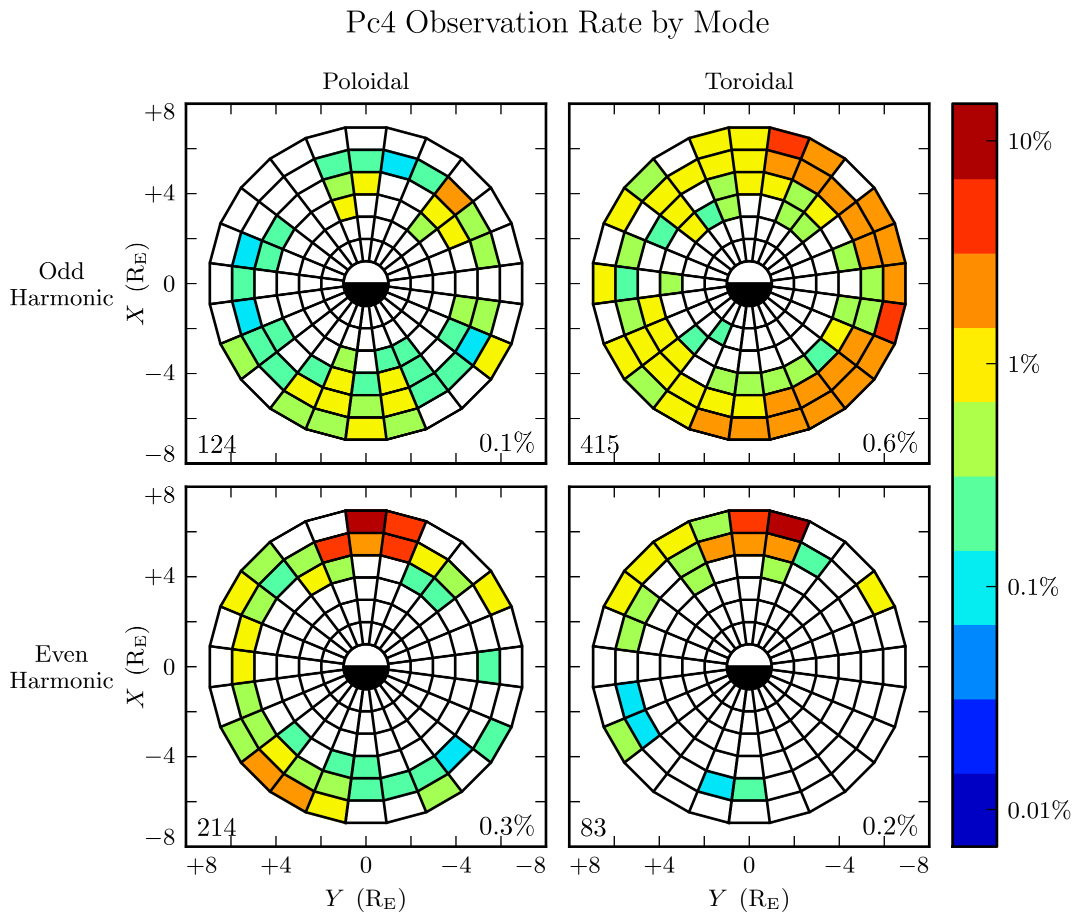

Figure 8.3: The above figure shows the spatial distribution for the same 762 events shown in Figure 8.2, partitioned by polarization and parity. The selection criteria described in Section 8.1 ensure that both properties are known for all events. Event counts are normalized by the time spent by the amount of usable data in each bin. Counts shown in the bottom-left corners do not sum to 762 because some events trigger on both the poloidal channel and the toroidal channel. Bins shown in white contain zero events.

Double-triggering can be taken as a vague proxy for event quality. When the channels both trigger independently, the two events almost always (71 of 74 events) exhibit the same parity. This suggests a poloidal wave with suffient power, and a sufficient narrow spectral peak, that it can still be seen after much of its energy has rotated to the toroidal mode.

TODO: Show plot of double-triggering events.

Odd double-triggering events are spread broadly in MLT. They rarely occur twice on the same day (23 events spread over 20 days), are observed at comparable rates regardless of DST.

Even-harmonic double-triggering events, on the other hand, are mostly seen near noon, and are significantly more common when DST $< -30\,\mathrm{nT}$. Even events are also more concentrated than odd ones. The 48 even-harmonic double-events are spread over 20 days, and 35 of them are spread over just 7 days. This clustering — where the poloidal and toroidal channel both trigger for five to ten half-hour events in the same day — is prevalent regardless of DST.

The distribution of even poloidal events in Figure 8.3 is consistent with that reported by Dai[18]: the observation rate is peaked at noon, and smeared across the dusk side. Notably, Dai's work focused on even poloidal waves. While he did not explicitly remove odd events from his sample, he did introduce a threshold in the magnetic field. This threshold is preferrentially satisfied by even waves (which have a magnetic field antinode near the equator) compared to odd waves (which have a magnetic field node). Dai characterized the parity of only a quarter of his events; among those, he found even harmonics to outnumber odd harmonics ten-to-one.

In fact — to the degree that they can be straightforwardly compared — the distributions in Figure 8.3 also show agreement with work by Anderson[3] (using AMPTE/CCE), Kokubun[53] (using ATS6), Liu[57] (using THEMIS), and Motoba[72] (using GOES). Toroidal events dominate overall, and are primarily seen on the morning side. Poloidal events are spread broadly in MLT, with a peak near noon and distinctive odd harmonics in the early morning.

Crucially, the present work can offer insight into how previous results fit together. Unlike events considered in previous works, those shown in Figure 8.3 have all been categorized in terms of both polarization and parity. And, perhaps more importantly, the selection process has not introduced a bias with respect to polarization or parity (at least not an obvious one).

Not only does Figure 8.3 show that toroidal events outnumber poloidal events, but it also shows that toroidal events are predominantly odd harmonics — as opposed to the primarily-even poloidal events. This may suggest that odd poloidal waves are more likely than even ones to be driven at low modenumber (allowing a prompt rotation of that energy to the toroidal mode). One might expect low-m poloidal modes to be driven by a broad, sudden change in solar wind dynamic pressure, for instance. The relative scarcity of odd poloidal observations on the dayside may indicate a short-lived source. At low m, energy rotates to the toroidal mode on the order of a wave period; without an ongoing source, there would be no poloidal wave to observe.

TODO: Actually, it looks like odd poloidal waves are split about half-and-half around $\left|\frac{B_z}{B_x}\right| = 0.2$. Compressional odd modes are more common near midnight. Noncompressional ones are mostly in the morning. Even poloidal events are skewed toward low m. This is probably worth showing.

TODO: Odd poloidal events are skewed nightward compared to odd toroidal events. This is not surprising. Per Chapter 7, nightside poloidal events are less likely to give rise to toroidal events than those on the dayside. Even events too, actually. The toroidal distribution looks like the poloidal distribution, but skewed dayward.

This would furthermore be consistent with even modes' apparent dearth of ground signatures[95]. If even harmonics tend to be produced at higher modenumber than odd ones, even harmonics would be expected to produce ground signatures less often[3].

Even poloidal modes and even toroidal modes exhibit similar distributions in space: both are peaked at noon and smeared across the dusk flank, with little activity on the dawn side. This is further support for the even poloidal wave as a significant source for the even toroidal mode.

TODO: People have talked about this. Is there a conventional explanation for dawn-dusk asymmetry?

TODO: What else do we want to say here? Or does the rest of the commentary belong in the later sections? Note that plots in future sections are lower resolution, to make sure that the number of bins remains much smaller than the number of events.

[3] See Equation (3.3).

TODO: How does this relate to the numerical results in Chapter 7?

8.3 Events by Amplitude

One might reasonable be concerned that the spatial distributions presented in Figure 8.3 are dominated by these small events, while Pc4 events large enough to be noteworthy follow a different distribution entirely. The goal of the present section is to address that concern.

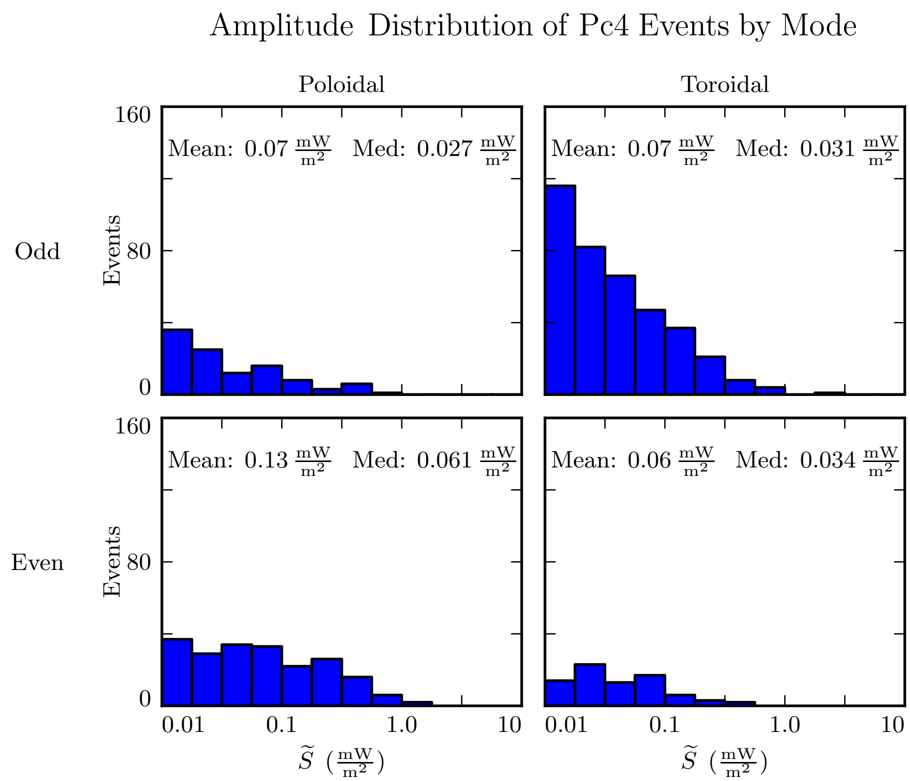

Figure 8.4: Amplitude distribution is shown for Pc4 events by parity and polarization, based on the peak of the spectrum's Gaussian fit. Odd poloidal events, odd toroidal events, and even toroidal events fall off sharply with increasing amplitude, while the even poloidal events are distributed more broadly — the mean and median of the even poloidal distribution is twice as large as that of the others.

The distribution of event magnitudes is presented in Figure 8.4, graded based on the peak of the Gaussian fit of each event's Poynting flux, $|\widetilde{S}(\omega)|$. Mean and median values are listed for each mode. Most events are small, with Poynting flux well below $0.1\,\mathrm{mW/m^2}$ when mapped to the ionosphere. Only a handful of events — 3 out of 762 — exceed $1\,\mathrm{mW/m^2}$, typically taken to be the threshold at which visible auroral arcs form. One such event is shown in Figure 8.5.

TODO: Say something about this event? Not really clear what purpose is served by this example, actually. As a matter of curiosity, the apparent wave activity in the toroidal channel did not pass the event selection trigger because the electric and magnetic waveforms are not coherent.

Perhaps the most notable feature of Figure 8.4 is the relative uniformity of the distribution of even poloidal events. If a higher magnitude threshold is imposed, as shown in Figure 8.6, the proportion of even poloidal events rises.

The spatial bins in Figure 8.6 are larger than those in Section 8.2; this change reflects an effort to keep the number of events large compared to the number of bins, even when considering relatively small subsets of the data. The larger bins — two hours wide in MLT and divided at $L = 5$ radially — are also used in Sections 8.4 and 8.5. All of the large-binned bullseye plots also share a common logarithmic color bar.

All else being equal, one might expect the amplitude distribution of even toroidal modes to mimic that of even poloidal modes, since poloidal waves asymptotically rotate to toroidal waves. However, this does not seem to be the case. The mean and median magnitudes are more or less consistent for even toroidal modes, odd toroidal modes, and odd poloidal modes, while even poloidal modes are twice as large by those metrics. This would seem to imply that large even poloidal modes have disproportionately high modenumbers, and thus deliver energy to the toroidal mode less efficiently. This explanation is also unsatisfying, however; Figure 8.6 shows that even poloidal and toroidal modes both become more concentrated near noon at high amplitude, suggesting a common origin.

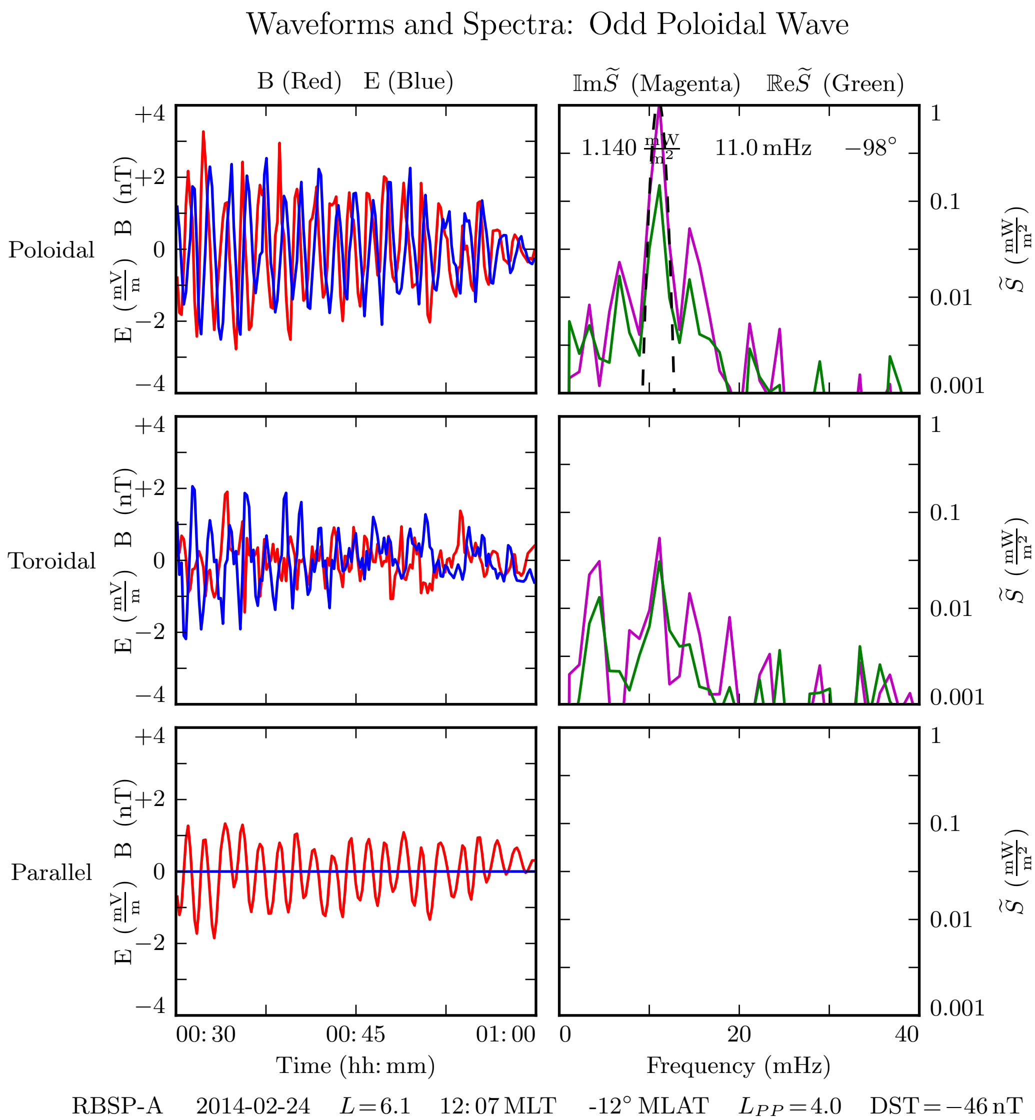

Figure 8.5: TODO: ···

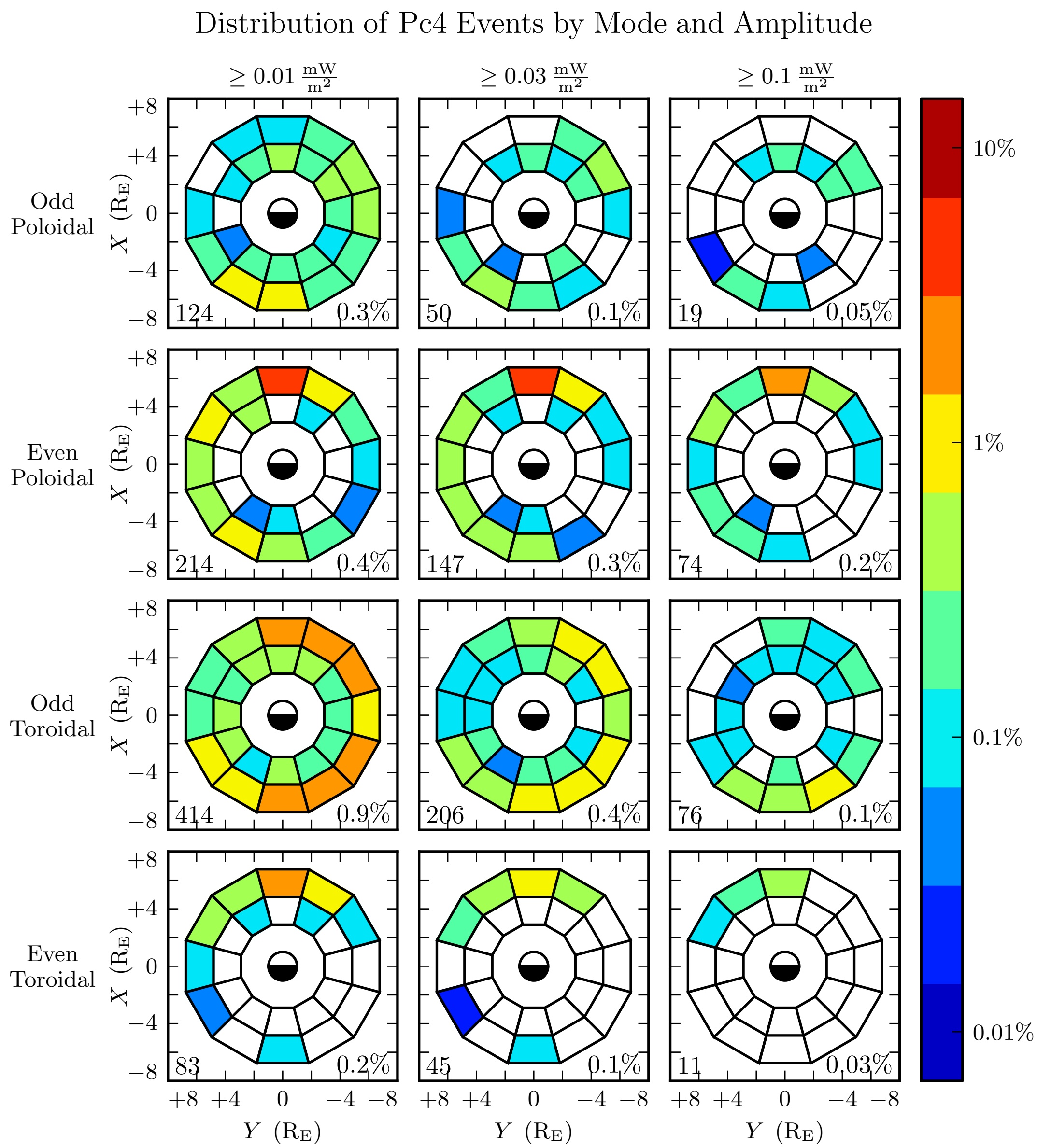

Figure 8.6: The above figure shows the distribution of Pc4 event observations by mode. Event magnitude cutoff is constant down each column, and increases from left to right. Stronger even events appear to become more concentrated on the dayside as the amplitude increases. Even poloidal events also become significantly more numerous relative to the other three modes, from 26 % at a cutoff of $0.01\,\mathrm{mW/m^2}$ to 41 % at $0.1\,\mathrm{mW/m^2}$.

8.4 Events by Frequency

The difference in magnetospheric conditions between the dayside and the nightside suggest that different eigenfrequencies should arise between dayside and nightside resonances at the same L-shell. In fact, this phenomenon has been observed directly; the frequencies of azimuthally-drifting FLRs have been shown to change over time[72]. The effect is attributed to the difference in mass loading (and thus Alfvén speed) as a function of MLT.

This effect was furthermore apparent in the numerical results shown in Chapter 7, where Alfvén speeds on the dayside (based on empirical profiles) gave rise to significantly higher eigenfrequencies than those on the nightside.

In Figure 8.7, events at 11 mHz to 17 mHz (center column) do seem to be shifted nightward compared to those at 7 mHz to 11 mHz (left column), but the effect is far more pronounced than what is suggested by Sections 7.2 and 7.3.

TODO: We should show the runs driven at $L \sim 5$ across the board. Dayside and nightside. That way we can make a fair comparison.

As might be expected, even events are more prevalent than first-harmonic-dominated odd events higher in the Pc4 range. Events at 7 mHz to 11 mHz (left column) outnumber those at 17 mHz to 25 mHz (right column) ten-to-one or more for odd events. Among even events, the comparison is closer to three-to-one.

The spatial distribution of odd toroidal events above 17 mHz warrants specific consideration. Whereas odd toroidal events overall show an overwhelming preference for the morning side, those at the top of the Pc4 frequency band instead appear from noon to dusk. It's possible that this distribution is a consequence of the small number of events (25). More likely, however, is that these are third-harmonic events, and that their source more closely resembles the source for second-harmonic waves than it does first-harmonics.

TODO: Have people looked at third harmonics?

The frequency distribution for each mode is shown in Figure 8.8. The most distinctive feature, certainly, is the frequency peak in the odd toroidal mode near 9 mHz. This is in line with the idea that toroidal waves exhibit frequencies that depend sharply on L, as discussed in Chapter 7. While the Van Allen Probes' orbits do cover a large range of L-shells, their observations (and thus the selected events) are concentrated near apogee at $L \sim 6$.

TODO: Maybe put the Gaussian fit back on top of these distributions? The distributions are not particularly Gaussian, but it gives a quantitative estimate of the spread.

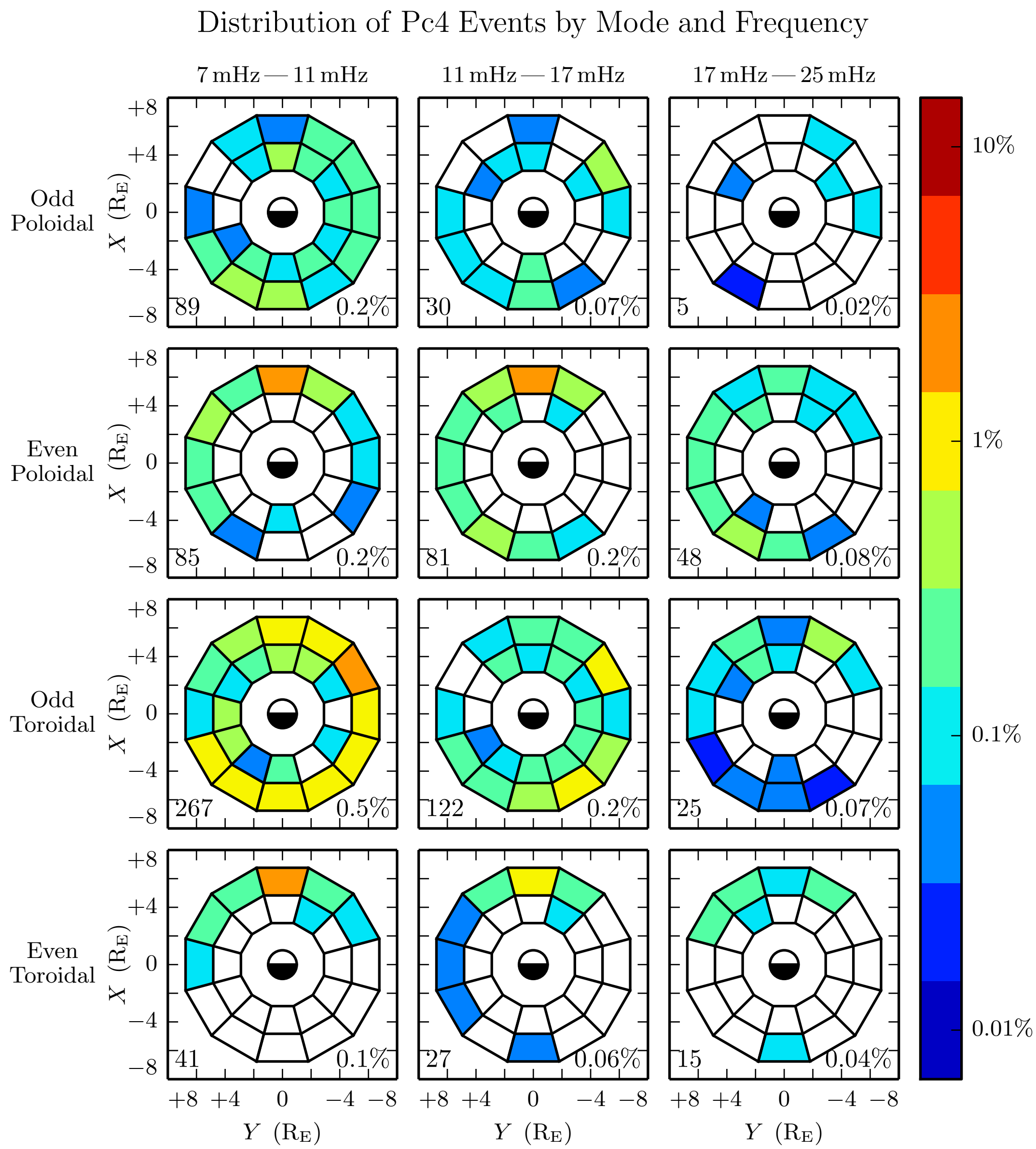

Figure 8.7: Event distributions above are shown in terms of mode (row) as well as event frequency (column). Mid-frequency Pc4 events are shifted somewhat nightward compared to low-frequency Pc4 events, as might be expected from the dayside's faster Alfvén speed. At the top of the Pc4 band, the distribution of odd toroidal events takes on a decidedly different character; this is likely because they are third harmonics rather than first harmonics.

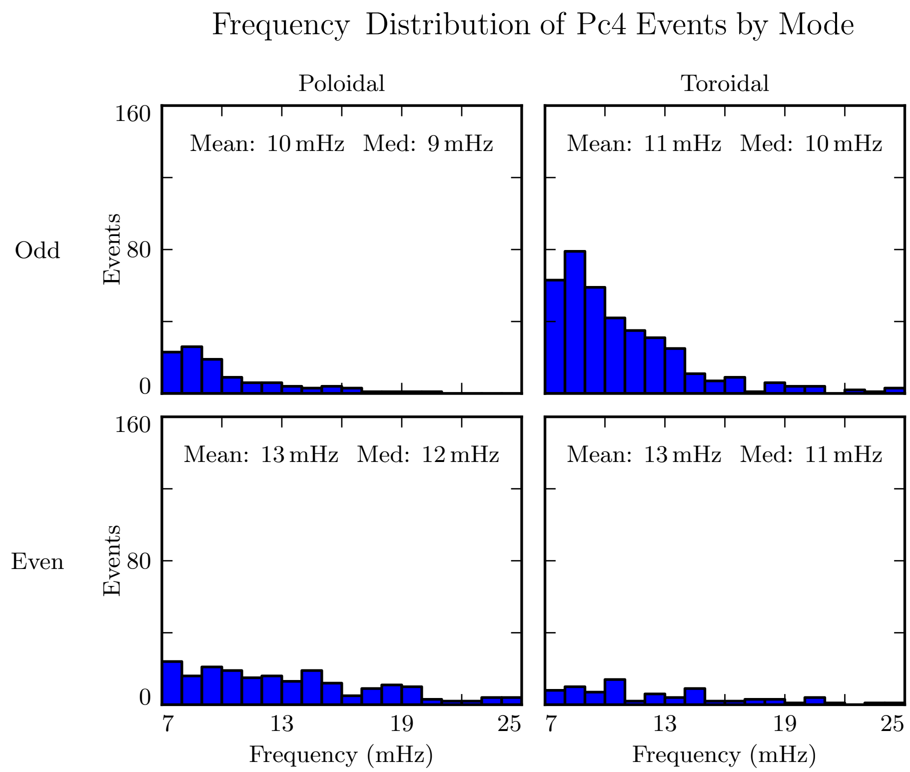

Figure 8.8: Frequency distributions are shown for all events, divided by harmonic and polarization. Odd toroidal events exhibit a particularly sharp peak in frequency, which is consistent with the toroidal mode's strong correlation with the local eigenfrequency. Poloidal modes appear more spread out in frequency, which is also consistent with past observations and with the numerical results in Chapter 7.

8.5 Events by Phase

The phase of a wave — that is, the phase offset between a wave's electric and magnetic fields — indicates how its energy is partitioned between the standing and traveling wave modes. An ideal standing wave has a phase of $\pm 90°$, and thus its Poynting flux is completely imaginary. A traveling wave, on the other hand, has electric and magnetic fields in phase (or in antiphase), and is associated with a net movement of energy, usually toward the ionosphere.

Wave phase is a topic of significant interest, since it allows an estimate to be made of the wave's lifetime. And, because phase can only be determined using simultaneous electric and magnetic field measurements, it has only recently become observable.

TODO: Do people really care about phase, or is it just John?

The energy per unit volume, and the rate at which energy is carried out of that volume by Poynting flux, are respectively given by:

$$U = \frac{R^3}{2\mu_0} B^2 \qquad\qquad \frac{\partial}{\partial t} U = \frac{R^2}{\mu_0} E B \cos\varphi \tag{8.2}$$

Where B, E, and R are the characteristic magnetic field magnitude, electric field magnitude, and length scale. The phase, $\varphi \equiv \arctan \frac{\mathbb{I}\mathrm{m}\widetilde{S}}{\mathbb{R}\mathrm{e}\widetilde{S}}$, enters because only real Poynting flux carries energy.

The ratio of the two quantities in Equation (8.2) gives a characteristic timescale over which energy leaves the system

$$\tau \equiv \frac{BR}{2E\cos\varphi} \tag{8.3}$$

In the present case, magnetic fields are on the order of $1\,\mathrm{nT}$ and electric fields are on the order of $1\,\mathrm{mV/m}$. A reasonable scale length might be $10^4\,\mathrm{km}$, the distance traversed by the probe over the course of a half-hour event (notably, back-to-back events are unusual).

At a phase of 80°, this timescale is comparable to a Pc4 wave period. At 135°, where energy is divided evenly between the standing and traveling wave, the timescale is only 7 seconds. A wave with a phase so far from 90° would quickly vanish unless it were constantly being replenished.

An example of just such an event is shown in Figure 8.9. The left column shows electric and magnetic field waveforms in blue and red respectively. The right shows the corresponding spectra: imaginary Poynting flux in magenta (corrresponding to the strength of the standing wave) and real Poynting flux in green (for the traveling wave). The black line is a Gaussian fit to the magnitude of the Poynting flux.

The poloidal channel shows a mostly-standing wave, with a phase of 79°. The coherent activity in the compressional magnetic field implies a low azimuthal modenumber, and thus a fast rotation of energy from the poloidal mode to the toroidal mode. It's likely the rotation of energy from the poloidal mode contributes significantly to the toroidal mode's lifetime; the toroidal wave's phase is 130°, so its energy should be carried away quickly by Poynting flux.

The selection process described in Section 8.1 does not explicitly consider phase. However, the discrete Fourier transform is performed over a half-hour time span. An event with a comparatively short lifetime would be unlikely to register. It's unsurprising to see the events in Figure 8.10tightly clustered near 90°.

It's further notable in Figure 8.10 that the odd events are more spread out in phase than the even events. Near the equator, odd modes have an electric field antinode and a magnetic field node; per Equation (8.3), an odd mode's lifetime should be longer than that of an even mode with the same phase. Figure 8.10 uses the absolute value of each event's phase, as does Figure 8.11.

Unlike amplitude (Section 8.3) and frequency (Section 8.4), events of different phase do not seem to exhibit different spatial distributions, as shown in Figure 8.11. Comparisons are limited by the small event counts in several of the subplots; however, coarsely speaking, events with phases of 75° and worse (left column) show spatial distributions more or less in proportion with events phased 85° or better (right column).

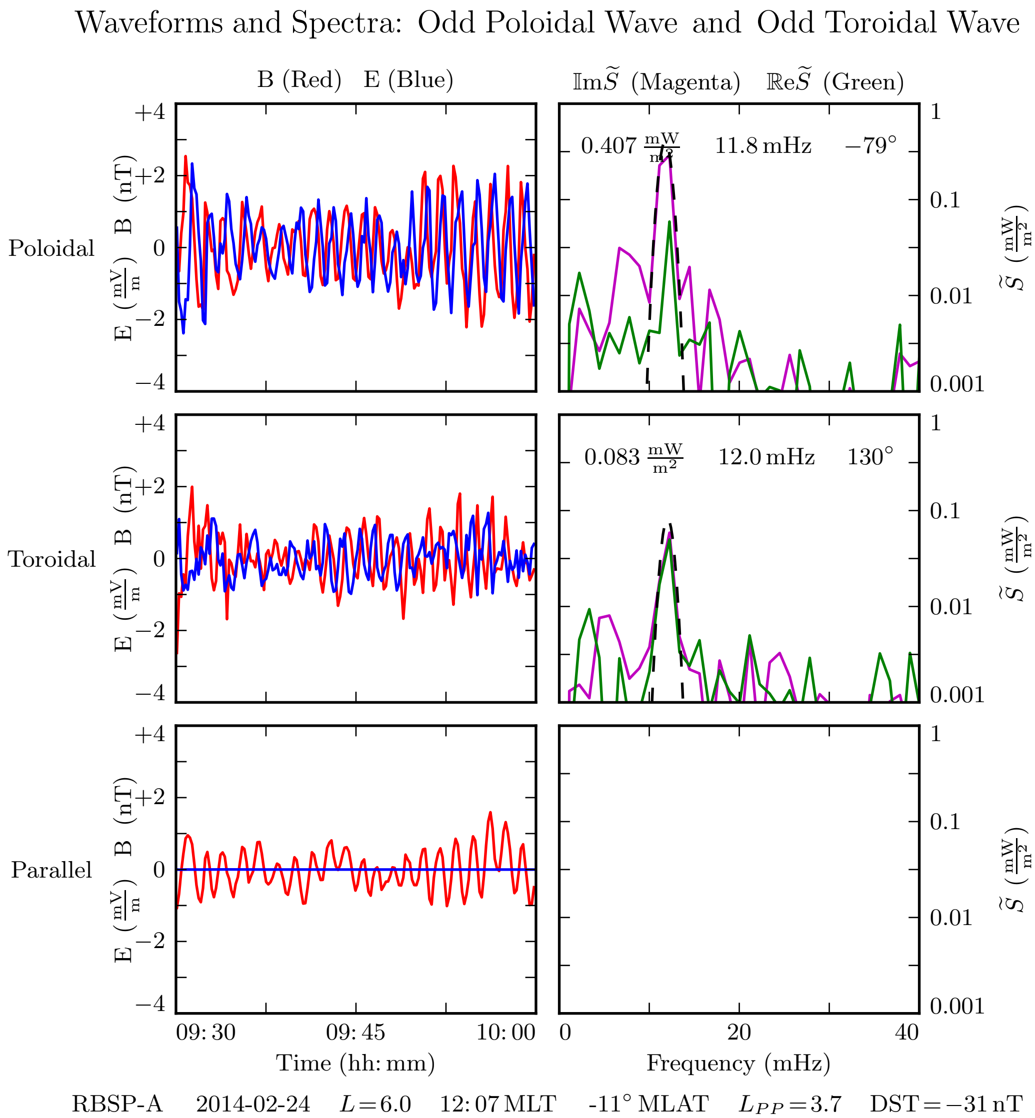

Figure 8.9: The above is a double event, where the poloidal and toroidal channels have been independently selected as events. The poloidal channel shows a wave with most of its energy in the standing wave (phase of 79°). The toroidal mode has a significant traveling component (phase of 130°). The compressional activity implies a low modenumber, which would cause energy to rotate quickly from the poloidal mode to the toroidal mode — evidently at a sufficient rate to replenish the losses due to the traveling mode's real Poynting flux.

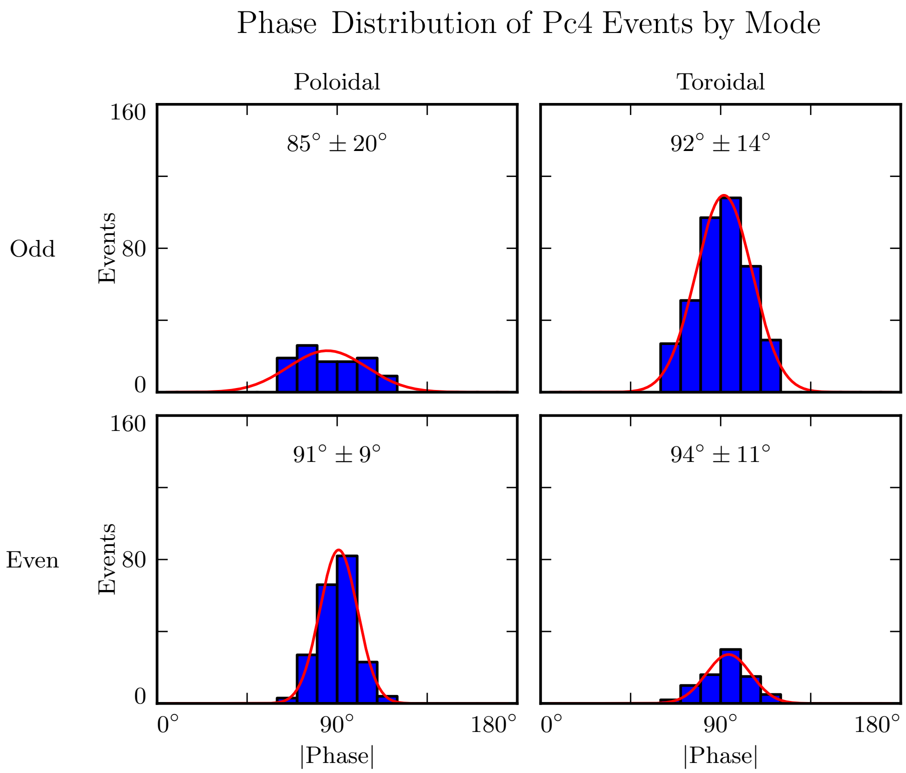

Figure 8.10: The (absolute) phase of the selected Pc4 events is shown above. All modes show phase distributions peaked around 90°. This reflects the fact that a significant traveling wave component quickly carries energy away from an FLR. Odd events are spread more broadly in phase than even events. This is consistent with the odd modes' electric field antinode near the equator, where events are observed; the characteristic loss timescale depends on $\frac{B}{E}$ per Equation (8.3).

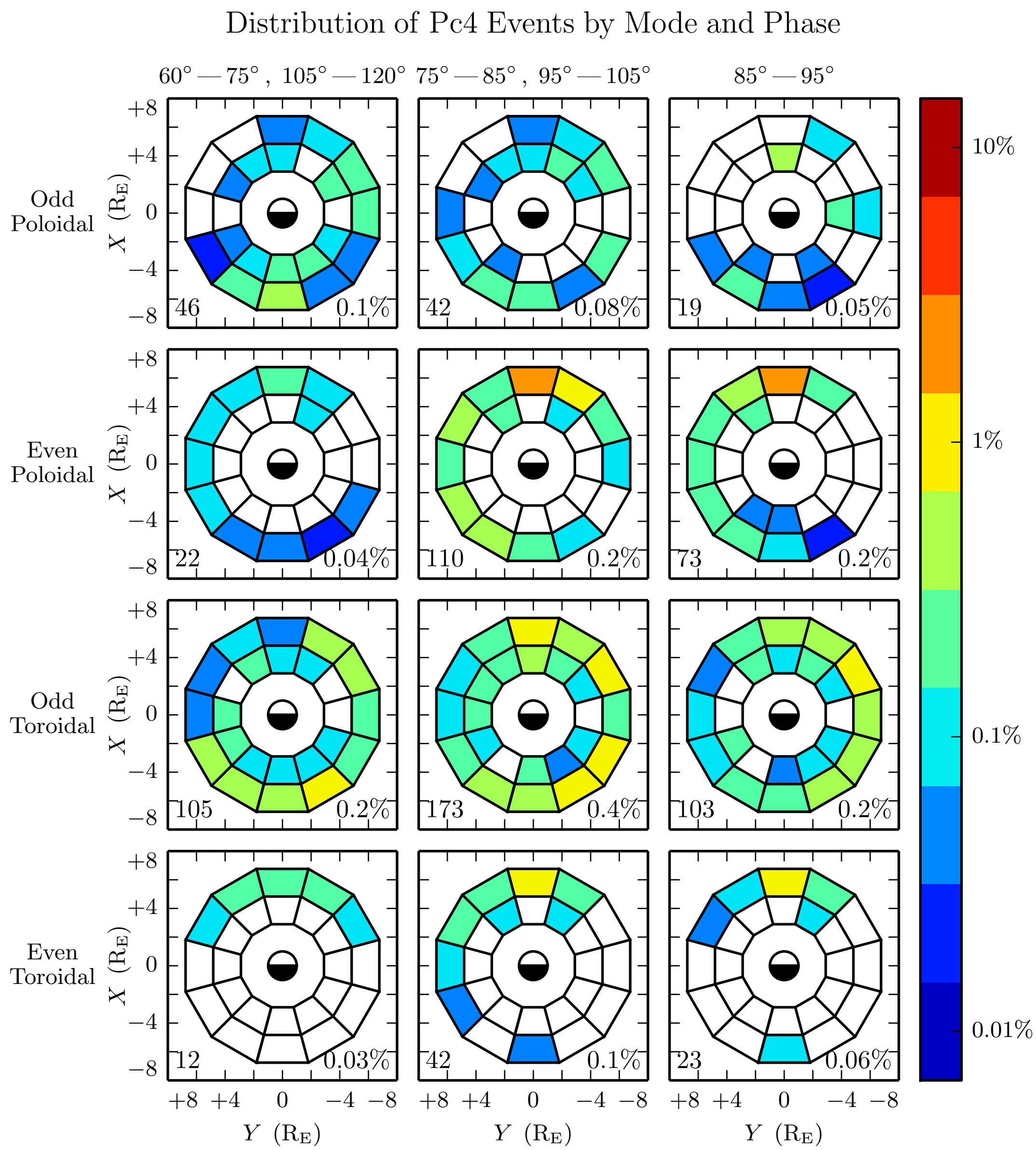

Figure 8.11: The observation rate of events is shown above, divided by (absolute) phase as well as mode. The closer a phase to 90°, the more of an event's energy is in the standing wave, rather than the traveling wave. The spatial distribution of events is more or less consistent between waves with phases very close to 90° and those with a significant traveling wave component.

8.6 Discussion

TODO: Odd poloidal events and odd toroidal events are distributed similarly in space. Even poloidal events and even toroidal events too. Toroidal events are skewed dayward compared to poloidal events, which makes sense, since on the nightside poloidal-to-toroidal rotation timescales are comparable to dissipation timescales.

TODO: Poloidal events are mostly even. Toroidal events are mostly odd. Maybe this indicates a different preference in modenumber?

TODO: Even poloidal events are skewed toward high amplitude compared to the other modes. Stronger even poloidal events are also skewed dayward.

TODO: Odd toroidal events near the top of the Pc4 frequency range exhibit qualitatively different behavior from the other odd toroidal modes. They are probably third harmonics. Maybe third harmonics have a source mechanism more like second harmonics than like first.

TODO: Most events have (absolute) phase in the range $80°$ to $100°$, indicating that most of the energy is in the standing wave. Odd events are spread a bit more broadly in phase. This makes sense, since they ahve an electric field antinode near the equator (where measurements are made) which makes them less susceptible to energy loss from the traveling wave.

Chapter 9

Conclusion

9.1 Summary of Results

TODO: Code development... Chapters 5 and 6

TODO: Make the Git repository public, and link to it.

TODO: Numerical results... Chapter 7

TODO: Re-summarize the Discussion sections, I guess.

TODO: Observational results... Chapter 8

TODO: Link to the Git repository.

9.2 Future Work

TODO: Code development.

Arbitrary deformation of grid. Get $\hat{e}_i = \frac{\partial}{\partial u^i}\underline{x}$, then $g_{ij} = \hat{e}_i \cdot \hat{e}_j$, then invert the metric tensor for contravariant components.

MPI. Time to compute vs time to broadcast. This might make sense for inertial length scales.

Better ionospheric profiles. Distinction between the dawn and dusk flanks. Maybe even update the conductivity based on energy deposition — precipitation causes ionization!

IRI ionosphere model. Solar illumination effects.

TODO: Numerical work.

More complicated driving. Higher harmonics, non-sinusoidal waveforms. Maybe evern drive based on events?

Look at the phase of waves in Tuna. How much is standing/traveling?

TODO: Analysis of RBSP data.

Basically just do everything over again, twice as well, once the probes have finished sampling the dayside again.

References

[1] S.-I. Akasofu. The development of the auroral substorm. *Planetary and Space Science*, 12(4):273–282, 1964.

[2] H. Alfvén. On the cosmogony of the solar system III. *Stockholms Observatoriums Annaler*, 14:9.1–9.29, 1946.

[3] B. J. Anderson, M. J. Engebretson, S. P. Rounds, L. J. Zanetti, and T. A. Potemra. A statistical study of Pc 3-5 pulsations observed by the AMPTE/CCE magnetic fields experiment, 1. occurrence distributions. *J. Geophys. Res.*, 95(A7):10495, 1990.

[4] V. Angelopoulos. The THEMIS mission. *Space Science Reviews*, 141(1-4):5–34, 2008.

[5] C. W. Arthur and R. L. McPherron. The statistical character of Pc 4 magnetic pulsations at synchronous orbit. *J. Geophys. Res.*, 86(A3):1325, 1981.

[6] K. Birkeland. Expédition norvégienne de 1899-1900 pour l'étude des aurores boréales. *Mat. Naturvidensk. Kl.*, KI(I), 1901.

[7] J. P. Boris. A physically motivated solution of the Alfvén problem. *NRL Memorandum Report*, 2167, 1970.

[8] A. Brekke, T. Feder, and S. Berger. Pc4 giant pulsations recorded in Tromsø, 1929-1985. *Journal of Atmospheric and Terrestrial Physics*, 49(10):1027–1032, 1987.

[9] C. W. Carlson, R. F. Pfaff, and J. G. Watzin. The fast auroral SnapshoT (FAST) mission. *Geophys. Res. Lett.*, 25(12):2013–2016, 1998.

[10] A. A. Chan, M. Xia, and L. Chen. Anisotropic alfvén-ballooning modes in Earth's magnetosphere. *J. Geophys. Res. Space Physics*, 99(A9):17351–17366, 1994.

[11] L. Chen and A. Hasegawa. A theory of long-period magnetic pulsations: 1. steady state excitation of field line resonance. *J. Geophys. Res.*, 79(7):1024–1032, 1974.

[12] L. Chen and A. Hasegawa. Kinetic theory of geomagnetic pulsations: 1. internal excitations by energetic particles. *J. Geophys. Res.*, 96(A2):1503, 1991.

[13] L. Chen, R. White, C. Cheng, F. Romanelli, J. Weiland, R. Hay, J. V. Dam, D. Barnes, M. Rosenbluth, and S. Tsai. Theory and simulation of fishbone-type instabilities in beam-heated tokamaks. Technical report, 1984.

[14] C. Z. Cheng and Q. Qian. Theory of ballooning-mirror instabilities for anisotropic pressure plasmas in the magnetosphere. *J. Geophys. Res.*, 99(A6):11193, 1994.

[15] G. Chisham and D. Orr. Statistical studies of giant pulsations (pgs): Harmonic mode. *Planetary and Space Science*, 39(7):999–1006, 1991.

[16] W. D. Cummings, R. J. O'Sullivan, and P. J. Coleman. Standing Alfvén waves in the magnetosphere. *J. Geophys. Res.*, 74(3):778–793, 1969.

[17] L. Dai. Collisionless magnetic reconnection via Alfvén eigenmodes. *Phys. Rev. Lett.*, 102(24), 2009.

[18] L. Dai, K. Takahashi, R. Lysak, C. Wang, J. R. Wygant, C. Kletzing, J. Bonnell, C. A. Cattell, C. W. Smith, R. J. MacDowall, S. Thaller, A. Breneman, X. Tang, X. Tao, and L. Chen. Storm time occurrence and spatial distribution of Pc4 poloidal ULF waves in the inner magnetosphere: A Van Allen Probes statistical study. *J. Geophys. Res. Space Physics*, 120:4748–4762, 2015.

[19] L. Dai, K. Takahashi, J. R. Wygant, L. Chen, J. Bonnell, C. A. Cattell, S. Thaller, C. Kletzing, C. W. Smith, R. J. MacDowall, D. N. Baker, J. B. Blake, J. Fennell, S. Claudepierre, H. O. Funsten, G. D. Reeves, and H. E. Spence. Excitation of

poloidal standing Alfvén waves through drift resonance wave-particle interaction. *Geophys. Res. Lett.*, 40:4127–4132, 2013.

[20] A. W. Degeling, R. Rankin, and Q.-G. Zong. Modeling radiation belt electron acceleration by ULF fast mode waves, launched by solar wind dynamic pressure fluctuations. *J. Geophys. Res. Space Physics*, 119(11):8916–8928, 2014.

[21] W. D. D'haeseleer, W. N. G. H. J. D. Callen, and J. L. Shohet. *Flux Coordinates and Magnetic Field Structure*. Springer-Verlag, New York, 1991.

[22] J. W. Dungey. The attenuation of Alfvén waves. *J. Geophys. Res.*, 59(3):323–328, 1954.

[23] J. W. Dungey. Interplanetary magnetic field and the auroral zones. *Phys. Rev. Lett.*, 6(2):47–48, 1961.

[24] A. Einstein. Die grundlage der allgemeinen relativitätstheorie. *Ann. Phys.*, 354:769–822, 1916.

[25] S. R. Elkington, M. K. Hudson, and A. A. Chan. Acceleration of relativistic electrons via drift-resonant interaction with toroidal-mode Pc-5 ULF oscillations. *Geophys. Res. Lett.*, 26(21):3273–3276, 1999.

[26] M. J. Engebretson, D. L. Murr, K. N. Erickson, R. J. Strangeway, D. M. Klumpar, S. A. Fuselier, L. J. Zanetti, and T. A. Potemra. The spatial extent of radial magnetic pulsation events observed in the dayside near synchronous orbit. *J. Geophys. Res.*, 97(A9):13741, 1992.

[27] M. J. Engebretson, L. J. Zanetti, T. A. Potemra, and M. H. Acuna. Harmonically structured ulf pulsations observed by the ampte cce magnetic field experiment. *Geophysical Research Letters*, 13(9):905–908, 1986.

[28] M. J. Engebretson, L. J. Zanetti, T. A. Potemra, D. M. Klumpar, R. J. Strangeway, and M. H. Acuña. Observations of intense ULF pulsation activity near the geomagnetic equator during quiet times. *J. Geophys. Res.*, 93(A11):12795, 1988.

[29] S. Fujita and T. Tamao. Duct propagation of hydromagnetic waves in the upper ionosphere, 1, electromagnetic field disturbances in high latitudes associated with localized incidence of a shear Alfvén wave. *J. Geophys. Res.*, 93(A12):14665, 1988.

[30] K.-H. Glassmeier. Magnetometer array observations of a giant pulsation event. *J. Geophys.*, 48:127–138, 1980.

[31] K.-H. Glassmeier. On the influence of ionospheres with non-uniform conductivity distribution on hydromagnetic waves. *J. Geophys.*, 54(2):125–137, 1984.

[32] K.-H. Glassmeier, S. Buchert, U. Motschmann, A. Korth, and A. Pedersen. Concerning the generation of geomagnetic giant pulsations by drift-bounce resonance ring current instabilities. *Ann. Geophysicae*, 17:338–350, 1999.

[33] C. Goertz. Kinetic alfvén waves on auroral field lines. *Planetary and Space Science*, 32(11):1387–1392, 1984.

[34] C. K. Goertz and R. W. Boswell. Magnetosphere-ionosphere coupling. *J. Geophys. Res.*, 84(A12):7239, 1979.

[35] C. A. Green. Giant pulsations in the plasmasphere. *Planetary and Space Science*, 33(10):1155–1168, 1985.

[36] J. L. Green and S. Boardsen. Duration and extent of the great auroral storm of 1859. *Advances in Space Research*, 38(2):130–135, 2006.

[37] C. Greifinger and P. S. Greifinger. Theory of hydromagnetic propagation in the ionospheric waveguide. *J. Geophys. Res.*, 73(23):7473–7490, 1968.

[38] B. C. Hall. *Lie Groups, Lie Algebras, and Representations.* Graduate Texts in Mathematics. Springer, New York, second edition, 2015.

[39] Y. X. Hao, Q.-G. Zong, Y. F. Wang, X.-Z. Zhou, H. Zhang, S. Y. Fu, Z. Y. Pu, H. E. Spence, J. B. Blake, J. Bonnell, J. R. Wygant, and C. A. Kletzing. Interactions of energetic electrons with ULF waves triggered by interplanetary shock: Van allen probes observations in the magnetotail. *J. Geophys. Res. Space Physics*, 119(10):8262–8273, 2014.

[40] L. Harang. *Pulsations in the terrestrial magnetic records at high latitude stations.* Grondahl, 1942.

[41] O. Hillebrand, J. Muench, and R. L. McPherron. Ground-satellite correlative study of a giant pulsation event. *Journal of Geophysics Zeitschrift Geophysik*, 51:129–140, 1982.

[42] W. J. Hughes. The effect of the atmosphere and ionosphere on long period magnetospheric micropulsations. *Planet. Space Sci.*, 22:1157–1172, 1974.

[43] W. J. Hughes. Magnetospheric ULF waves: A tutorial with a historical perspective. In M. J. Engebretson, K. Takahashi, and M. Scholer, editors, *Solar Wind Sources of Magnetospheric Ultra-Low-Frequency Waves*, volume 81 of *Geophys. Monogr.*, pages 1–12. American Geophysical Union, Washington, DC, 1994.

[44] W. J. Hughes and D. J. Southwood. The screening of micropulsation signals by the atmosphere and ionosphere. *J. Geophys. Res.*, 81(19):3234–3240, 1976.

[45] W. J. Hughes, D. J. Southwood, B. Mauk, R. L. McPherron, and J. N. Barfield. Alfvén waves generated by an inverted plasma energy distribution. *Nature*, 275(5675):43–45, 1978.

[46] J. A. Jacobs, Y. Kato, S. Matsushita, and V. A. Troitskaya. Classification of geomagnetic micropulsations. *J. Geophys. Res.*, 69(1):180–181, 1964.

[47] T. Karlsson and G. T. Marklund. A statistical study of intense low-altitude electric fields observed by freja. *Geophys. Res. Lett.*, 23(9):1005–1008, 1996.

[48] Y. Kato and T. Tsutomu. Hydromagnetic oscillations in a conducting medium with hall couduct-ivity under the uniform magnetic field. *Science reports of the Tohoku University. Ser. 5, Geophysics*, 7(3):147–164, 1956.

[49] M. C. Kelley. *The Earth's Ionosphere*. Academic Press, San Diego, second edition, 1989.

[50] R. L. Kessel. Solar wind excitation of pc5 fluctuations in the magnetosphere and on the ground. *J. Geophys. Res.*, 113(A4), 2008.

[51] D. Y. Klimushkin, P. N. Mager, and K.-H. Glassmeier. Toroidal and poloidal Alfvén waves with arbitrary azimuthal wavenumbers in a finite pressure plasma in the earth's magnetosphere. *Annales Geophysicae*, 22(1):267–287, 2004.

[52] S. Kokubun. Observations of Pc pulsations in the magnetosphere: Satellite-ground correlation. *J. Geomagn. Geoelec*, 32(Supplement2):SII17–SII39, 1980.

[53] S. Kokubun, K. N. Erickson, T. A. Fritz, and R. L. McPherron. Local time asymmetry of Pc 4-5 pulsations and associated particle modulations at synchronous orbit. *J. Geophys. Res.*, 94(A6):6607–6625, 1989.

[54] D.-H. Lee and K. Kim. Compressional MHD waves in the magnetosphere: A new approach. *J. Geophys. Res.*, 104(A6):12379–12385, 1999.

[55] A. S. Leonovich and V. A. Mazur. Structure of magnetosonic eigenoscillations of an axisymmetric magnetosphere. *J. Geophys. Res.*, 105(A12):27707–27715, 2000.

[56] W. Liu, J. B. Cao, X. Li, T. E. Sarris, Q.-G. Zong, M. Hartinger, K. Takahashi, H. Zhang, Q. Q. Shi, and V. Angelopoulos. Poloidal ULF wave observed in the plasmasphere boundary layer. *J. Geophys. Res. Space Physics*, 118(7):4298–4307, 2013.

[57] W. Liu, T. E. Sarris, X. Li, S. R. Elkington, R. Ergun, V. Angelopoulos, J. Bonnell, and K. H. Glassmeier. Electric and magnetic field observations of Pc4 and Pc5 pulsations in the inner magnetosphere: A statistical study. *J. Geophys. Res.*, 114(A12), 2009.

[58] W. Liu, T. E. Sarris, X. Li, Q.-G. Zong, R. Ergun, V. Angelopoulos, and K. H. Glassmeier. Spatial structure and temporal evolution of a dayside poloidal ULF wave event. *Geophys. Res. Lett.*, 38(19), 2011.

[59] R. L. Lysak. Magnetosphere-ionosphere coupling by Alfvén waves at midlatitudes. *J. Geophys. Res.*, 109, 2004.

[60] R. L. Lysak and D. hun Lee. Response of the dipole magnetosphere to pressure pulses. *Geophys. Res. Lett.*, 19(9):937–940, 1992.

[61] R. L. Lysak and Y. Song. A three-dimensional model of the propagation of Alfvén waves through the auroral ionosphere: first results. *Adv. Space Res.*, 28:813–822, 2001.

[62] R. L. Lysak and Y. Song. Nonlocal kinetic theory of alfvn waves on dipolar field lines. *Journal of Geophysical Research: Space Physics*, 108(A8), 2003. 1327.

[63] R. L. Lysak, C. L. Waters, and M. D. Sciffer. Modeling of the ionospheric Alfvén resonator in dipolar geometry. *J. Geophys. Res. Space Physics*, 118, 2013.

[64] P. N. Mager and D. Y. Klimushkin. Giant pulsations as modes of a transverse Alfvénic resonator on the plasmapause. *Earth, Planets and Space*, 65(5):397–409, 2013.

[65] I. R. Mann, E. A. Lee, S. G. Claudepierre, J. F. Fennell, A. Degeling, I. J. Rae, D. N. Baker, G. D. Reeves, H. E. Spence, L. G. Ozeke, R. Rankin, D. K. Milling, A. Kale, R. H. W. Friedel, and F. Honary. Discovery of the action of a geophysical synchrotron in the Earth's Van Allen radiation belts. *Nature Communications*, 4, 2013.

[66] I. R. Mann and A. N. Wright. Finite lifetimes of ideal poloidal Alfvén waves. *J. Geophys. Res.*, 100:23677–23686, 1995.

[67] I. R. Mann, A. N. Wright, and A. W. Hood. Multiple-timescales analysis of ideal poloidal Alfvén waves. *J. Geophys. Res.*, 102(A2):2381–2390, 1997.

[68] T. Maynard, N. Smith, S. Gonzalez, et al. Solar storm risk to the North American electric grid. 2013.

[69] K. McGuire, R. Goldston, M. Bell, M. Bitter, K. Bol, K. Brau, D. Buchenauer, T. Crowley, S. Davis, F. Dylla, H. Eubank, H. Fishman, R. Fonck, B. Grek, R. Grimm, R. Hawryluk, H. Hsuan, R. Hulse, R. Izzo, R. Kaita, S. Kaye, H. Kugel, D. Johnson, J. Manickam, D. Manos, D. Mansfield, E. Mazzucato, R. McCann, D. McCune, D. Monticello, R. Motley, D. Mueller, K. Oasa, M. Okabayashi, K. Owens, W. Park, M. Reusch, N. Sauthoff, G. Schmidt, S. Sesnic, J. Strachan, C. Surko, R. Slusher, H. Takahashi, F. Tenney, P. Thomas, H. Towner, J. Valley,

and R. White. Study of high-beta magnetohydrodynamic modes and fast-ion losses in PDX. *Phys. Rev. Lett.*, 50(12):891–895, 1983.

[70] R. L. McPherron. The role of substorms in the generation of magnetic storms. *Washington DC American Geophysical Union Geophysical Monograph Series*, 98:131–147, 1997.

[71] R. L. McPherron, G. K. Parks, D. S. Colburn, and M. D. Montgomery. Satellite studies of magnetospheric substorms on august 15, 1968: 2. solar wind and outer magnetosphere. *J. Geophys. Res.*, 78(16):3054–3061, 1973.

[72] T. Motoba, K. Takahashi, J. V. Rodriguez, and C. T. Russell. Giant pulsations on the afternoonside: Geostationary satellite and ground observations. *J. Geophys. Res. Space Physics*, 120:8350–8367, 2015.

[73] NASA. Coordinated data analysis (workshop) web.

[74] NASA. Near miss: The solar superstorm of july 2012.

[75] M. Nicolet. The collision frequency of electrons in the ionosphere. *Journal of Atmospheric and Terrestrial Physics*, 3(4):200–211, 1953.

[76] L. G. Ozeke and I. R. Mann. Energization of radiation belt electrons by ring current ion driven ULF waves. *J. Geophys. Res.*, 113(A2), 2008.

[77] E. M. Poulter, W. Allan, E. Nielsen, and K.-H. Glassmeier. Stare radar observations of a PG pulsation. *J. Geophys. Res.*, 88(A7):5668, 1983.

[78] J. A. Proehl, W. Lotko, I. Kouznetsov, and S. D. Geimer. Ultralow-frequency magnetohydrodynamics in boundary-constrained geomagnetic flux coordinates. *J. Geophys. Res.*, 107(A9):1225, 2002.

[79] H. R. Radoski. A note on oscillating field lines. *J. Geophys. Res.*, 72(1), 1967.

[80] H. R. Radoski. A theory of latitude dependent geomagnetic micropulsations: The asymptotic fields. *J. Geophys. Res.*, 79, 1974.

[81] R. Rankin, J. C. Samson, and V. T. Tikhonchuk. Parallel electric fields in dispersive shear alfvén waves in the dipolar magnetosphere. *Geophys. Res. Lett.*, 26(24):3601–3604, 1999.

[82] B. Rolf. Giant micropulsations at abisko. *J. Geophys. Res.*, 36(1):9, 1931.

[83] G. Rostoker, H.-L. Lam, and J. V. Olson. PC 4 giant pulsations in the morning sector. *J. Geophys. Res.*, 84(A9):5153, 1979.

[84] J. C. Samson, L. L. Cogger, and Q. Pao. Observations of field line resonances, auroral arcs, and auroral vortex structures. *J. Geophys. Res.*, 101(A8):17373–17383, 1996.

[85] H. J. Singer, W. J. Hughes, and C. T. Russell. Standing hydromagnetic waves observed by ISEE 1 and 2: Radial extent and harmonic. *J. Geophys. Res.*, 87(A5):3519, 1982.

[86] D. J. Southwood. Some features of field line resonances in the magnetosphere. *Planetary and Space Science*, 22(3):483–491, 1974.

[87] D. J. Southwood. A general approach to low-frequency instability in the ring current plasma. *J. Geophys. Res.*, 81(19):3340–3348, 1976.

[88] J. Stratton and N. J. Fox. Radiation belt storm probes (RBSP) mission overview. In *2012 IEEE Aerospace Conference*. Institute of Electrical & Electronics Engineers (IEEE), 2012.

[89] E. Sucksdorff. Giant pulsations recorded at sodankyl during 19141938. *Terrestrial Magnetism and Atmospheric Electricity*, 44(2):157–170, 1939.

[90] K. Takahashi, J. Bonnell, K.-H. Glassmeier, V. Angelopoulos, H. J. Singer, P. J. Chi, R. E. Denton, Y. Nishimura, D.-H. Lee, M. Nosé, and W. Liu. Multipoint observation of fast mode waves trapped in the dayside plasmasphere. *J. Geophys. Res.*, 115(A12), 2010.

[91] K. Takahashi, K.-H. Glassmeier, V. Angelopoulos, J. Bonnell, Y. Nishimura, H. J. Singer, and C. T. Russell. Multisatellite observations of a giant pulsation event. *J. Geophys. Res.*, 116:A11223, 2011.

[92] K. Takahashi, M. D. Hartinger, V. Angelopoulos, K.-H. Glassmeier, and H. J. Singer. Multispacecraft observations of fundamental poloidal waves without ground magnetic signatures. *J. Geophys. Res. Space Physics*, 118:4319–4334, 2013.

[93] K. Takahashi, R. W. McEntire, A. T. Y. Lui, and T. A. Potemra. Ion flux oscillations associated with a radially polarized transverse Pc 5 magnetic pulsation. *J. Geophys. Res.*, 95(A4):3717, 1990.

[94] K. Takahashi and R. L. McPherron. Standing hydromagnetic oscillations in the magnetosphere. *Planetary and Space Science*, 32:1343–1359, 1984.

[95] K. Takahashi, N. Sato, J. Warnecke, H. L´uhr, H. E. Spence, and Y. Tonegawa. On the standing wave mode of giant pulsations. *J. Geophys. Res. Space Physics*, 97(A7):10717–10732, 1992.

[96] B. J. Thompson and R. L. Lysak. Electron acceleration by inertial alfvén waves. *J. Geophys. Res.*, 101(A3):5359–5369, 1996.

[97] V. T. Tikhonchuk and R. Rankin. Electron kinetic effects in standing shear alfvén waves in the dipolar magnetosphere. *Physics of Plasmas*, 7(6):2630, 2000.

[98] B. T. Tsurutani, W. D. Gonzalez, G. S. Lakhina, and S. Alex. The extreme magnetic storm of 12 september 1859. *Journal of Geophysical Research: Space Physics*, 108(A7), 2003. 1268.

[99] A. Y. Ukhorskiy. Impact of toroidal ULF waves on the outer radiation belt electrons. *J. Geophys. Res.*, 110(A10), 2005.

[100] J. Veldkamp. A giant geomagnetic pulsation. *Journal of Atmospheric and Terrestrial Physics*, 17(4):320–324, 1960.

[101] J. A. Wanliss and K. M. Showalter. High-resolution global storm index: Dst versus sym-h. *Journal of Geophysical Research: Space Physics*, 111(A2):n/a–n/a, 2006. A02202.

[102] C. L. Waters, R. L. Lysak, and M. D. Sciffer. On the coupling of fast and shear Alfvén wave modes by the ionospheric Hall conductance. *Earth Planets Space*, 65:385–396, 2013.

[103] C. L. Waters and M. D. Sciffer. Field line resonant frequencies and ionospheric conductance: Results from a 2-d MHD model. *J. Geophys. Res.*, 113(A5), 2008.

[104] D. M. Wright and T. K. Yeoman. High-latitude HF doppler observations of ULF waves: 2. waves with small spatial scale sizes. *Ann. Geophys.*, 17(7):868–876, 1999.

[105] J. R. Wygant, J. W. Bonnell, K. Goetz, R. E. Ergun, F. S. Mozer, S. D. Bale, M. Ludlam, P. Turin, P. R. Harvey, R. Hochmann, K. Harps, G. Dalton, J. McCauley, W. Rachelson, D. Gordon, B. Donakowski, C. Shultz, C. Smith, M. Diaz-Aguado, J. Fischer, S. Heavner, P. Berg, D. M. Malsapina, M. K. Bolton, M. Hudson, R. J. Strangeway, D. N. Baker, X. Li, J. Albert, J. C. Foster, C. C. Chaston, I. Mann, E. Donovan, C. M. Cully, C. A. Cattell, V. Krasnoselskikh, K. Kersten, A. Brenneman, and J. B. Tao. The electric field and waves instruments on the radiation belt storm probes mission. *Space Science Reviews*, 179(1):183–220, 2013.

[106] J. R. Wygant, A. Keiling, C. A. Cattell, R. L. Lysak, M. Temerin, F. S. Mozer, C. A. Kletzing, J. D. Scudder, V. Streltsov, W. Lotko, and C. T. Russell. Evidence for kinetic alfvn waves and parallel electron energization at 46 re altitudes in the plasma sheet boundary layer. *Journal of Geophysical Research: Space Physics*, 107(A8):SMP 24–1–SMP 24–15, 2002.

[107] K. Yee. Numerical solution of initial boundary value problems involving maxwell's equations in isotropic media. *IEEE Trans. Antennas Propagat.*, 14(3), 1966.

[108] T. K. Yeoman and D. M. Wright. ULF waves with drift resonance and drift-bounce resonance energy sources as observed in artificially-induced HF radar backscatter. *Ann. Geophys.*, 19(2):159–170, 2001.

[109] Q.-G. Zong, X.-Z. Zhou, X. Li, P. Song, S. Y. Fu, D. N. Baker, Z. Y. Pu, T. A. Fritz, P. Daly, A. Balogh, and H. Réme. Ultralow frequency modulation of energetic particles in the dayside magnetosphere. *Geophys. Res. Lett.*, 34(12), 2007.

[110] Q.-G. Zong, X.-Z. Zhou, Y. F. Wang, X. Li, P. Song, D. N. Baker, T. A. Fritz, P. W. Daly, M. Dunlop, and A. Pedersen. Energetic electron response to ULF

waves induced by interplanetary shocks in the outer radiation belt. *J. Geophys. Res.*, 114(A10), 2009.